Ultrafast Time-Resolved Terahertz Spectroscopy of Charge Carrier Dynamics in Semiconductors

A Dissertation

submitted in partial fulfilment of the requirements

for the degree of

Doctor of Philosophy

by

Avinash M. Warankar

(ID: 20143307)

THz Spectroscopy Lab

Department of Chemistry

Indian Institute of Science Education and Research-Pune

2023

Dedicated to

My Family

भारतीय विज्ञान शिक्षा एवं अनुसंधान संस्थान, पुणे
INDIAN INSTITUTE OF SCIENCE EDUCATION AND RESEARCH (IISER) PUNE
(An Autonomous Institution of Ministry of Human Resource Development, Govt. of India)
Dr. Homi Bhabha Road, Pune - 411008.

DECLARATION

I declare that this written submission represents my ideas in my own words and wherever other's ideas have been included; I have adequately cited and referenced the original sources. I also declare that I have adhered to all principles of academic honesty and integrity and have not misrepresented or fabricated or falsified any idea / data / fact / source in my submission. I understand that violation of the above will cause for disciplinary action by the Institute and can also evoke penal action from the sources which have thus not been properly cited or from whom proper permission has not been taken when needed.

Date: 12th April 2023

Mr. Avinash M. Warankar

(ID: 20143307)

भारतीय विज्ञान शिक्षा एवं अनुसंधान संस्थान, पुणे
INDIAN INSTITUTE OF SCIENCE EDUCATION AND RESEARCH (IISER) PUNE
(An Autonomous Institution of Ministry of Human Resource Development, Govt. of India)
Dr. Homi Bhabha Road, Pune - 411008.

Dr. Pankaj Mandal
Associate Professor
Department of Chemistry,
IISER Pune

CERTIFICATE

Certified that the work incorporated in the thesis entitled "***Ultrafast Time-Resolved Terahertz Spectroscopy of Charge Carrier Dynamics in Semiconductors***" submitted by **Mr. Avinash M. Warankar** was carried out by the candidate, under my supervision. The work presented here or any part of it has not been included in any other thesis submitted previously for the award of any degree or diploma from any other university or institution.

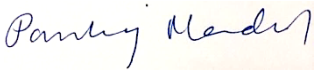

Dr. Pankaj Mandal

(Research Supervisor)

Date: 12th April 2023

Acknowledgement

First, I would like to thank my supervisor, Prof. Pankaj Mandal, for his constant support, enormous patience and guidance during my PhD. He always encourages me and strengthens my confidence. I always enjoy scientific discussions and his inputs on my PhD work during this process. Thank you, Sir.

I want to thank my Research Advisory Committee (RAC) members, Prof. Nirmalya Ballav and Prof. Sayan Bagchi, for their feedback, suggestions during RAC meetings, and support throughout my PhD.

I want to thank our collaborators Prof. Angshuman Nag, Prof. Kanishka Biswas, Prof. Satishchandra Ogale, Dr. Manoj Jana, Dr. Wasim Mir, Dr. Moinak Dutta, Dr. Subas Kumar Mudulli, Dr. Shidaling Matteppanavar for providing samples for THz experiments. I would also like to thank all the co-authors in my published and unpublished articles.

I want to thank IISER Pune for providing fellowship and research facilities. I want to thank Prof. H. N. Gopi for his support and encouragement. I thank Mr. Mayuresh Kulkarni for his support and conversation during this journey. I want to thank all the Chemistry department members, IISER Pune, who provided help and support during this journey.

I want to say thank you to Dr. Y. G. Reddy, a former labmate, for his assistance and technical guidance during my journey. Genuinely thank you for your support, Dr. Y. G. Reddy and you have always been very kind and caring to me. I learnt many technicalities related to optical alignment, data analysis etc., with Dr. Reddy. I want to thank all my current and former lab members, Dr. Sohini, Dr. Sneha, Aman, Shabnum, Riteeka, Rapti, Mayank, Ziyad, Garvit, and Nandana, for their support and help during my PhD journey. I would especially thank Nandana, Riteeka and Garvit for repeatedly reading Thesis chapters for constant improvement.

Most importantly, I thank my family for their unconditional love, support, and encouragement during my journey. Thank you for your love and support, Atya and Mama. Your contribution to my life is invaluable. My wife, Pallavi, has shown great support and faith in me. Throughout this journey, my mother, Smt. Manisha Warankar and mother-in-law Smt. Bhagashri Potdar have been by my side at all times. I would always be much obliged for their kind support and belief. I want to thank my sister, Meenakshi, my brother, Nilesh, my sister-in-law Rohini and Namita for their constant support and encouragement.

My friends have always encouraged me during this journey. My friends Dr. Sandip, Dr. Somanath, Mukesh, Harshawardhan, Dheeraj and many others for their wishes and support right from my post-graduation days. Thank you all of you.

I want to thank my IISER friends, Dr. Yogesh, Ganesh, Bhavin, Dr. Shammi and Dr. Udaysinh Bhosale, for their support, help and encouragement. I want to thank all my PhD batchmates for their support and scientific discussions during this journey. Many family members and friends have relentlessly provided their support, and I am always fortunate to receive their good wishes. Thank you all of you.

I am grateful to Prof. Vidya Patil for her support and encouragement during my undergraduate studies at Ruparel College. I have always learned many things about physics through discussions with my senior and friend Abhishek Chitnis and Mohan Mishra. I would also like to thank my childhood friend, Nilesh, for his support and good wishes. I want to thank Naval and Maruti for encouragement and inspiration. Thank you to all who directly and indirectly contributed to my PhD journey.

Synopsis

Terahertz (THz) radiation is a part of electromagnetic radiation between microwave and infrared frequency regions. The energy of THz photons lies in the milli-electronvolt (meV) range with a frequency of the order of 10^{12} Hz and wavelength in the sub-millimetre range. It is non-ionising and non-destructive for the majority of the material around us. Thanks to ultrafast laser technology, THz radiation has now been widely used as one of the important probes to study and characterise various systems, from small molecules to solids. In our ultrafast dynamics laboratory, broadband THz frequencies (up to 15 THz) are generated and detected using laser-induced air plasma by air photonics methods with an amplified femtosecond laser source.

Understanding nonequilibrium photoexcited charge carrier dynamics in semiconductors is crucial for developing and improving modern-day technology. Using time-resolved terahertz spectroscopy (TRTS) in transmission and reflection geometries, I investigated photoexcited charge carrier dynamics in nanocrystals (NCs) and bulk semiconductors having potential applications in optoelectronic, photodetector, and thermoelectric. THz spectroscopy is a noncontact way of measuring dielectric response, photoconductivity, and device parameters such as diffusion length, lifetime and carrier mobility of materials (in the THz frequency range). Physical and chemical phenomena that occur in the order of meV-energy can be probed using THz spectroscopy.

In **Chapter 2**, I have discussed different experimental techniques based on THz spectroscopy to study charge carrier dynamics in nanocrystal film and bulk semiconductors. THz time-domain spectroscopy (THz-TDS) in transmission and reflection geometries is used to understand steady-state THz absorption in semiconductors. Time-resolved THz spectroscopy (TRTS) in transmission and reflection geometries is employed to study the dynamics of photocarriers in semiconductors. I have discussed THz generation and detection methods, experimental setups of THz-TDS and TRTS THz techniques, and the procedure for collecting and analysing the experimental data. Various models and numerical procedures that help interpret experimental results are also addressed.

In **Chapter 3,** Time-resolved THz spectroscopy (TRTS) in transmission geometry is conducted on Thallium Halides (TlX, X=Br, I) thin films of nanocrystals and their bulk counterpart. TlX exhibits a metal halide perovskites-like electronics band structure. It is now well understood that the unique electronic band is one of the main reasons for many optoelectronic properties of metal halide perovskite. Charge carrier dynamics in TlBr NCs film slow down with increasing excitation fluence due to the saturation of surface trap states. In contrast, carrier dynamics is completely fluence-independent in TlI NCs film. Bulk thallium halide films studied at higher fluences (compared to TlX NCs film) showed similar photocarrier dynamics. Thallium halide films showed reasonably high carrier mobility and long diffusion length, possibly originating from its defect-tolerant electronic band structure.

Publications from this chapter:

Colloidal Thallium Halide Nanocrystals with Reasonable Luminescence, Carrier Mobility and Diffusion Length

Wasim J. Mir, Avinash Warankar, Ashutosh Acharya, Shyamashis Das, Pankaj Mandal*, and Angshuman Nag*

Chem. Sci. **2017**, 8, 4602-4611

Time-Resolved THz Spectroscopy of Thallium Halides (TlBr, TlI) Nanocrystal and Bulk Thin Films

Avinash Warankar, Wasim J. Mir, Ashutosh Acharya, Shyamashis Das, Angshuman Nag*, and Pankaj Mandal*

(manuscript under preparation)

In **Chapter 4,** photoexcited charge carrier dynamics in Indium Selenide (InSe) is investigated using TRTS in reflection mode. InSe is a class III-VI layered semiconductor and has shown promising optoelectronic properties in the last few years. Also, InSe possesses low thermal conductivity and is potentially useful as a thermoelectric semiconductor upon enhancing its electronic conductivity. Saturation of surface states governs the fluence-dependent charge carrier dynamics in InSe, which slow down carrier dynamics with increasing photoexcitation. This also indirectly estimates the density of surface states in bulk InSe.

Publication from this chapter:

Charge Carrier Dynamics in Indium Selenide

Avinash Warankar, Moinak Dutta, Kanishka Biswas*, and Pankaj Mandal*

(manuscript under preparation)

In **Chapter 5,** we investigated charge carrier dynamics in Thallium Selenide (TlSe) upon photoexcitation using TRTS in reflection mode. TlSe shows ultralow thermal conductivity. In TlSe, multicarrier recombination processes, including one with a significant bimolecular rate constant, largely control the dynamics of photocarriers. Also, we have compared intrinsic electronic conductivity and photoconductivity, and both conductivities are found to be in a similar order of magnitude.

Publication from this chapter:

Charge Carrier Dynamics in Thallium Selenide

Avinash Warankar, Moinak Dutta, Kanishka Biswas*, and Pankaj Mandal*

(manuscript under preparation)

In **Chapter 6**, emerging elemental two-dimensional (2D) Black Phosphorus (BP) is studied using the TRTS technique. The highly tunable electronic band gap of black phosphorus (0.3 to 2 eV) makes it an attractive material for many applications. We have discussed results obtained on charge carrier dynamics of few-layer BP nanoparticles (NPs) film. Charge carrier dynamics of few-layer BP NPs film is studied on various excitation wavelengths. Charge carrier dynamics of few-layer BP nanoparticles film is weakly wavelength-dependent. In contrast to most investigated 2D materials like graphene, our studies indicate that carrier recombination of few-layer BP NPs film is slower (hundreds of ps), and a bimolecular process may be one of the key recombination processes.

Publication from this chapter:

Ultrafast Charge Carrier Dynamics of Few-Layer Black Phosphorus Nanoparticles Film

Avinash Warankar, Subas Muduli, Satishchandra Ogale*, and Pankaj Mandal*

(manuscript under preparation)

Contents

Glossary of Acronyms

ABCD	: Air biased coherent detection
AFM	: Atomic force microscopy
BBO	: β-Barium borate/$Ba(BO_2)_2$
CB	: Conduction band
CBM	: Conduction band minimum
DC	: Direct current
dc	: Drude conductivity
DRS	: Diffuse reflection spectroscopy
DSP	: Digital signal processor
EM	: Electromagnetic
EOS	: Electro-optic sampling
FL	: Few-layer
fs	: Femtosecond
FWHM	: Full width at half maximum
FWM	: Four-wave mixing
HDPE	: High-density polyethylene
HR Si	: High-resistivity silicon
IR	: Infrared
IRF	: Instrumental response function
kHz	: Kilohertz
LO	: Local oscillator
meV	: Milli electron volt
mm	: Milli metre
μm	: Micrometre
μs	: Microsecond
NCs	: Nanocrystals
NIR	: Near-infrared
NMP	: N-methyl-2-pyrrolidone
nm	: Nanometre
NPs	: Nanoparticles

OD	: Optical density
OPA	: Optical parametric amplifier
OPTP	: Optical-pump terahertz-probe
PL	: Photoluminescence
PLQY	: Photoluminescence quantum yield
PMT	: Photomultiplier tube
ps	: Picosecond
PS	: Polystyrene
PXRD	: Powder X-ray diffraction
SEM	: Scanning electron microscopy
SRS	: Stanford Research Systems
TA	: Transient absorption
TEM	: Transmission electron microscopy
THz	: Terahertz
THz-TDS	: Terahertz time-domain spectroscopy
Ti	: Titanium
TlX	: Thallium halide
TMD	: Transition metal dichalcogenide
TRTS	: Time-resolved terahertz spectroscopy
R-TRTS	: Reflection mode (geometry) time-resolved terahertz spectroscopy
2D	: Two-dimensional
UV	: Ultraviolet
VB	: Valence band
VBM	: Valence band maximum
E_g	: Bandgap

Chapter 1
Introduction

1.1 Background

Scientists are always curious about the interaction of radiation with matter, and they have gained a reasonably good understanding of the interaction of optical radiation, i.e., visible light, with various materials in the last several decades. The study of interaction between matter and radiation has expanded into other regions of electromagnetic (EM) radiation in the last few decades, especially in the terahertz (THz) frequency range (also known as the far-infrared region) after the invention and development of ultrafast lasers and amplifiers. Due to the lack of effective emitters and detectors, the THz frequency region, also known as the "THz gap", was not explored much till 1990. The "THz gap" lies between the microwave and the infrared regions of electromagnetic radiation (Figure 1). The frequency of 1 THz, i.e. 10^{12} Hz, equivalent to 10^{-12} s in time periodicity of EM wave oscillation, 4.1 meV in energy and 300 μm in wavelength. The typical THz frequency range spans from 0.1 to 10 THz. Photonics and wireless electronics are two technologies that operate on opposite sides of the THz gap. Wireless electronics technology operates at lower frequencies of the electromagnetic spectra, which is mostly exploited in telecommunication. Photonics on the other hand, deals with various methodologies of generation, detection and manipulation of photons, also the interplay of the optical and electronic signals is studied. Photonics is generally developed at much higher frequencies, such as visible and ultraviolet frequencies.

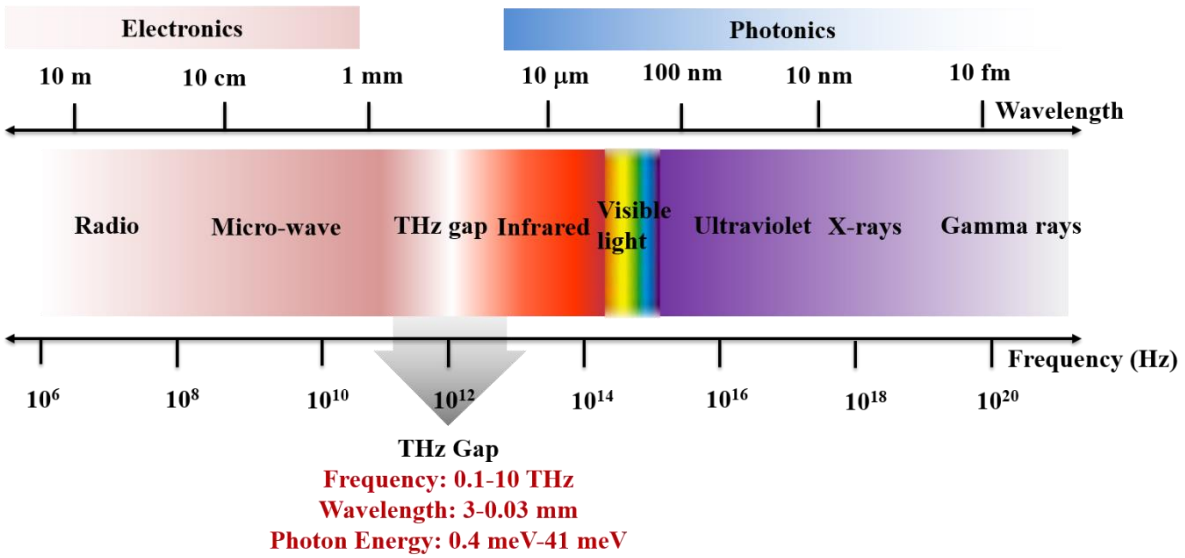

Figure 1. *Schematic of the electromagnetic spectrum showing THz radiation region.*

Now with almost three decades of research, THz radiation spans its application in many fields, such as physics, chemistry, biology, medical biology, pharmaceuticals, communications, security, quality control, non-destructive testing, imaging, etc.[1] The THz region is being utilised not only in fundamental research but in industrial applications as well.[2-4] THz spectroscopy offers unique advantages over conventional (optical) spectroscopy as it is a non-destructive, non-invasive, contact-free technique. It employs a heterodyne detection technique that measures the electric field as a function of time. Hence, both the phase and the amplitude of the electric field and, subsequently, the dispersion and the absorption of the system under study are obtained without using tedious Kramers–Kronig (K–K) relations. THz spectroscopy is based on ultrafast lasers, hence it can be used to probe dynamics and transient properties of materials with sub-ps temporal resolution.[5, 6] The temporal resolution of time-resolved THz experiments depends on the laser pulse width.

Modern technology depends largely on the development of semiconductors.[7] Semiconductors are usually crystalline materials with tunable optical and electronic properties.[8, 9] Like electronic properties, many of their other properties lie between those of metals and insulators. Silicon (Si), gallium (Ga), and carbon (C) are well-known semiconductors that exist in their elemental form and are called intrinsic semiconductors. They are used in many devices and electronic circuits and are well-researched from the perspective of basic understanding. Modern chemical and physical techniques produce semiconductors containing more than one element. Several factors are used to categorise semiconductors. For instance, the bandgap can be narrow, intermediate, or large; the bandgap can be direct or indirect; the doping can be p-type or n-type; and so on. The bandgap, i.e., the energy difference between the maximum of the valence band and the minimum of the conduction band, is one of the crucial properties of semiconductors. Generally, a material whose bandgap is smaller than silicon is called a narrow band gap semiconductor. Silicon's band gap is 1.1 eV and is indirect in nature. Semiconductors with a bandgap between 1.1 and 2 eV are said to have intermediate bandgap. Large bandgap semiconductors are those with a bandgap greater than 2 eV. Applications of semiconductors largely depend on their bandgap in addition to many other physical and chemical properties. Small bandgap semiconductors are primarily used in infrared photodetectors and thermoelectric devices. Intermediate bandgap semiconductors are useful in visible optoelectronics, photovoltaics, etc. Wide bandgap semiconductors find applications in

ultraviolet and other high-energy radiation detectors like gamma ray detectors, X-rays detectors, high-energy particle detectors, high-speed applications and power electronics.

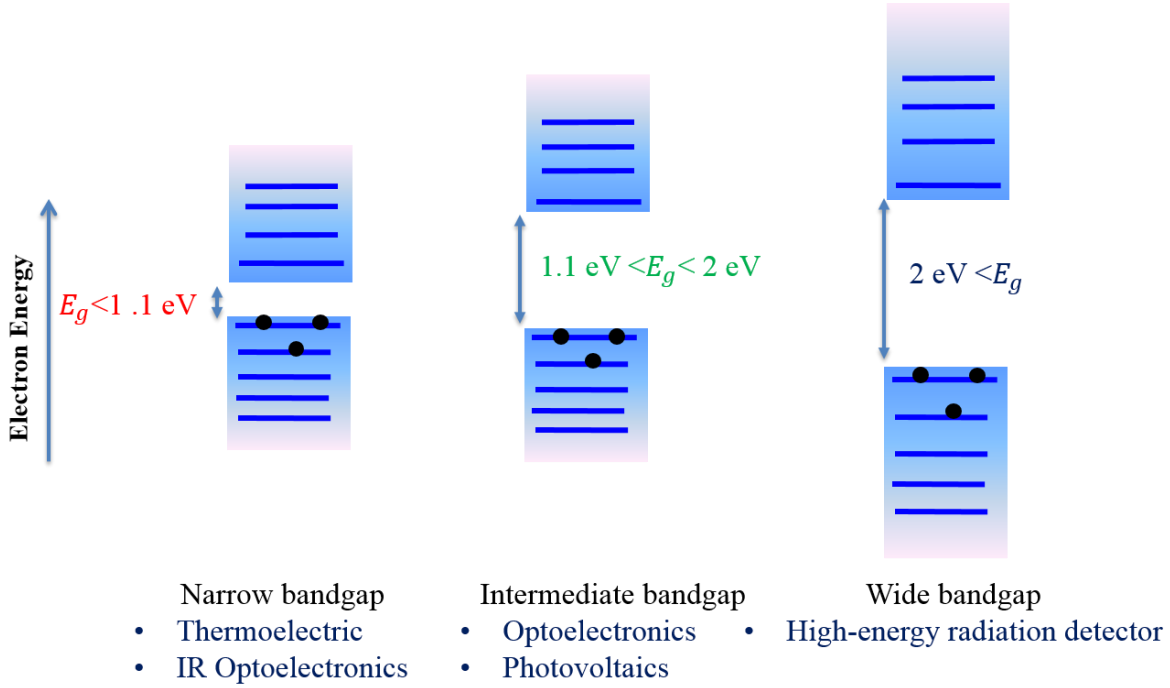

Figure 2. *Variation of bandgap of semiconductors and some of their bandgap dependent applications.*

Since optoelectronic properties depend primarily on the photoexcited states of semiconductors (Figure 3), studying photoexcited properties using various spectroscopic techniques is crucial for technological progress.[10] Evaluation of device parameters such as charge carrier mobility, diffusion length, and radiative and non-radiative carrier lifetimes are critical, especially for optoelectronic applications of semiconductors.

Figure 3. *Schematic of photoexcited properties of semiconductors a)Laser[11] b)Photovoltaic cells [12] and c)Light-emitting diodes (LED).[13] (Images taken from the internet website are cited.)*

In this thesis, semiconductor systems from bulk to nanoparticles having narrow to wide bandgap have been studied using THz spectroscopy. These semiconductors are promising as they could find potential applications in photodetector, thermoelectric, and optoelectronic devices.

1.1.1 Semiconductor photodetector

Photodetector is an optoelectronic device which converts optical signals into electronic signals, i.e. a device that can sense the presence of photons of a particular wavelength.[14, 15] In the photodetector, incident photons generate an excess number of electrons and holes, which creates current and increases the conductivity of the device, known as photoconductivity. It is the most fundamental quantity to be measured in the simplest type of semiconductor photodetector. The simplest photodetector is an n-type Si semiconductor connected to an ohmic contact with an external bias voltage (V_{bias}). Figure 4 shows the schematic of a photodetector (e.g. n-type Si semiconductor) with incident photon energy hv.

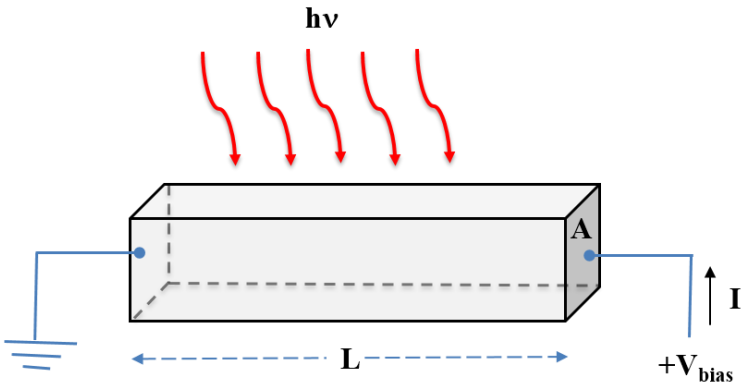

Figure 4. *Schematic of the photodetector (e.g. n-type Si semiconductor).*

Carrier lifetime (τ) is a crucial quantity since it gives us insight into the dynamics of a semiconductor device under photoexcitation. It is also fundamentally connected to the structural configuration, chemical bonding, and dielectric environment of semiconductor. Carrier mobility (μ) is the direct measure of transport characteristics. In a semiconductor photodetector, the product of mobility and lifetime is directly related to the figure of merit parameter.[14, 16] In the photodetector, which operates from infrared to UV regions, the gain (G)

is one of the important figure of merit parameter and exhibits the ability of carrier generation upon incident photon and which is given in the following relation as,[16]

$$G = \frac{\mu\tau\, V_{bias}}{L^2} \tag{1}$$

V_{bias} is the bias voltage across the contacts of the device, L is the length of the active channel of the device, and A is the area of the cross-section of the rectangular semiconductor.

In high-energy radiation detectors such as X-ray, and gamma-ray detectors, the signal sensitivity is described by modified Hetch equation[17-19] for photocurrent (I_{ph}) and is given by equation 2.

$$I_{ph} = \frac{I_0 \mu\tau\, V}{L^2} \frac{1 - \exp(-\frac{L^2}{\mu\tau\, V_{bias}})}{1 + \frac{Ls}{V_{bias}\mu}} \tag{2}$$

The sensitivity of the X-ray detector[19] is proportional to the photocurrent. D is the incident X-ray radiation dose.

$$Sensitivity \propto \frac{I_{ph}}{DV_{bias}} \tag{3}$$

Photoconductors must also be optimised for several other figure of merit parameters, including photoresponsivity (R), response time, cut-off frequency, noise equivalent power (NEP), specific detectivity (D*), and linear dynamic range (LDR) in order to develop efficient devices from semiconductors.[14, 16] The photoresponsivity (R) parameter expresses the electrical signal magnitude (the amount of photocurrent generation) per unit of incident optical power. Photoresponsivity is the ratio of the photocurrent (I_p) to the incident optical power (P),

$$R = \frac{I_p}{P} \tag{4}$$

Linear dynamic range (LDR) quantifies the maximum and the minimum measurable optical power range. The maximum power is limited by the non-linear response or optical damage to the photodetector, whereas the minimum power is generally determined by noise. LDR is

proportional to the ratio of maximum measurable power to minimum measurable power, and it is defined as,

$$LDR = 20\ log\left(\frac{I_p^*}{I_o}\right) \tag{5}$$

here I_p^* and I_o are photocurrent at the optical light intensity of around 1 mWcm^{-2} and the dark current of the photoconductor device respectively. Specific detectivity (D^*) is a significant parameter characterising the photodetector's sensitivity. Higher the specific detectivity, higher is the possibility of detecting a weak signal which competes with the detector's noise.

THz spectroscopy measures the photoconductivity of a material in a non-contact fashion. Hence, it has the potential to determine fundamental device parameters such as charge carrier mobility and carrier lifetime etc., which will provide insight into the material's potential for optoelectronic and various other applications.

1.1.2 Semiconductors for thermoelectric application

A thermoelectric device is based on the Seebeck effect and converts heat into electricity. Low bandgap semiconductors are generally used to fabricate thermoelectric materials. Thermoelectric applications require materials with low thermal conductivity and high electrical conductivity. While electrical conduction occurs primarily through charge carriers, heat is transported through both phonons and charge carriers. In many materials, low thermal conductivity is caused by phono-phonon scattering. Monitoring and quantifying the charge carrier and phonon dynamics in a potential thermoelectric material plays an important role in its practical applications. The thermoelectric efficiency is quantified by a dimensionless figure of merit ZT. It is defined as,

$$ZT = \left(\frac{S^2\sigma}{k_e + k_l}\right)T \tag{6}$$

here, S is the Seebeck coefficient, and T is the absolute temperature; σ, k_e, and k_l are the electrical conductivity, electronic thermal conductivity (due to charge carriers), and lattice thermal conductivity, respectively. Semiconductors have a large contribution from k_l to total

thermal conductivity than k_e in contrast to metals. The conductivity of the semiconductor is related to mobility (μ) and relaxation time or scattering time (τ) of charge carriers through the relation given below,

$$\sigma = ne\mu = n\left(\frac{e\tau}{m^*}\right) \quad (7)$$

here, n is carrier concentration, e is the charge of electron and m^* is effective or band mass of carrier (electron and hole).

Spectroscopic techniques in the THz frequency range can simultaneously investigate charge carrier and phonon transport phenomena and their dynamics. Since the energy of phonon oscillations falls in the THz range (the far-infrared region), THz spectroscopy can help identify phonon modes that play an essential role in restricting thermal conductivity in thermoelectric materials. THz spectroscopy measures steady-state (nonexcited) and photoexcited conductivity. It can provide an adequate understanding of electrical conduction when the contribution of phonons or other low-frequency excitations to the total conductivity is eliminated.

1.2 THz spectroscopy of semiconductors

Over the past three decades, THz spectroscopy has been proven to be an important technique for investigating the underlying photophysical properties of materials, particularly semiconductors in various forms such as bulk, thin films, and nanoparticles.[5, 20] Many physical and chemical processes occur in the THz frequency range. Carrier scattering in semiconductors [5], collective oscillations in crystalline solids[6], and intermolecular, collective vibration, low-frequency, diffusion and relaxation dynamical processes in liquids[6, 21] are a few examples of such processes. Moreover, intraband transitions[22, 23], and dynamics of excitons[24-26] and free carriers[5, 20, 27] of semiconductors have been successfully studied using THz spectroscopic techniques. Figure 5 shows interaction of matter and THz radiation, matter shows collective oscillation (e.g. phonon vibration), rotation (like molecular rotation), electron acceleration in the presence of few meV-energy THz photon.

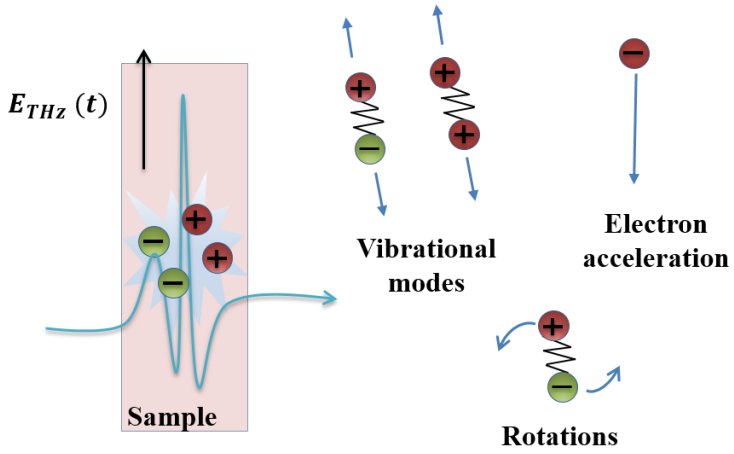

Figure 5. *Matter in the presence of THz radiation.*

1.2.1 THz interaction with photoexcited charge carriers

The primary interest of this thesis is to understand the photoexcited charge carrier dynamic probed by THz radiation. Hence, it is important to know how THz radiation interacts with matter. Photon of THz radiation has energy in the order of meV. Hence it can have the potential to probe chemical and physical phenomena in this energy scale or equivalent to other units. Unlike optical light, THz radiation cannot excite electrons and holes due to its small photon energy, but it produces an electrical current in a photoexcited sample.

THz radiation is transmissive and does not interact much with undoped or low intrinsic carrier concentration semiconductors. In the case of a photoexcited semiconductor, due to enhanced carrier concentration, important features occur in the THz frequency range (or equivalent other units). The plasma frequency in photoexcited semiconductors lies in THz frequency.[28] Scattering time in semiconductors usually lies in sub-picosecond time scales.[20] Charge carriers travel in a few hundred of nanometres in photoexcited semiconductors, and due to the picosecond time scale of THz radiation, if any kind of barriers for the carriers exist within the presence of THz pulse, a distinct spectral feature is observed.[29, 30]

Free carriers strongly interact and accelerate in the presence of the THz field, which shows a Drude-like conductivity (Figure 6a), which is a metallic fingerprint response.[5] Free carrier dynamics in the THz frequency region is dispersive.[5] In a quantum-confined system such as an electron and a hole in photoexcited quantum dots (Figure 6b), electron binding energy is relatively higher than the photon energy of the THz field, hence, the conductivity response is

entirely different from the free carriers. In such a quantum-confined system, polarizability gets induced in the presence of the THz field (Figure 6b).[24] In general, THz radiation interacts resonantly with free electron-like systems and non-resonantly with quantum-confined-like systems (as shown in Figures 7a and 7b).

Therefore, due to the unique interaction of THz radiation with matter, especially in time-resolved THz spectroscopy, THz radiation is used as a probe to monitor the excited state carrier density of the semiconductor, and hence effectively, it can be used to study carrier recombination and relaxation dynamics of material under investigation. In addition, important device parameters such as carrier mobility, diffusion length, and carrier lifetime can be evaluated in a non-contact manner, which is again one of the main advantages of this ultrafast technique.

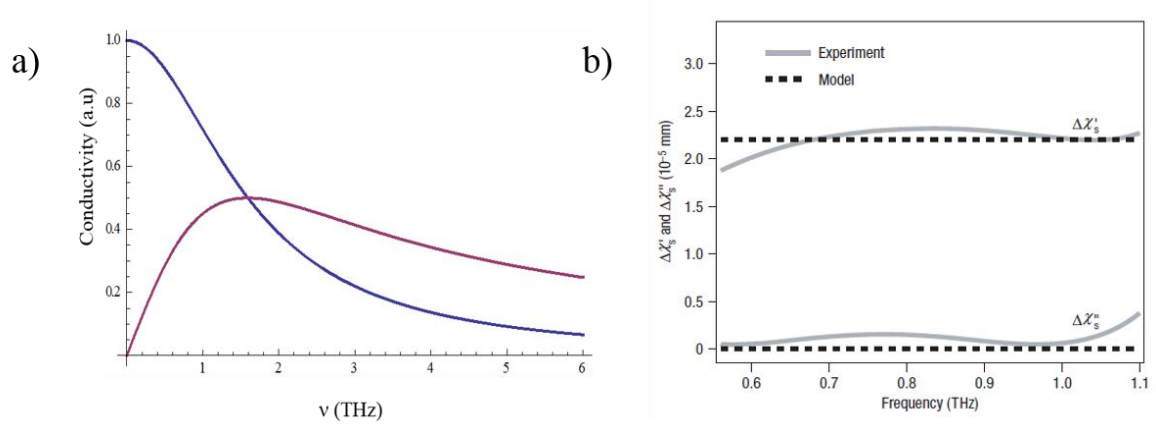

***Figure 6**. a) Free carrier response in THz frequency range. Complex conductivity simulated in Mathematica for Drude Model (for τ =100 fs and σ_{dc} = 1 unit. (real conductivity (blue) and imaginary conductivity (purple)) and b) Strongly quantum confined system in THz frequency range (Reproduced from reference [24] with permission from Springer Nature).*

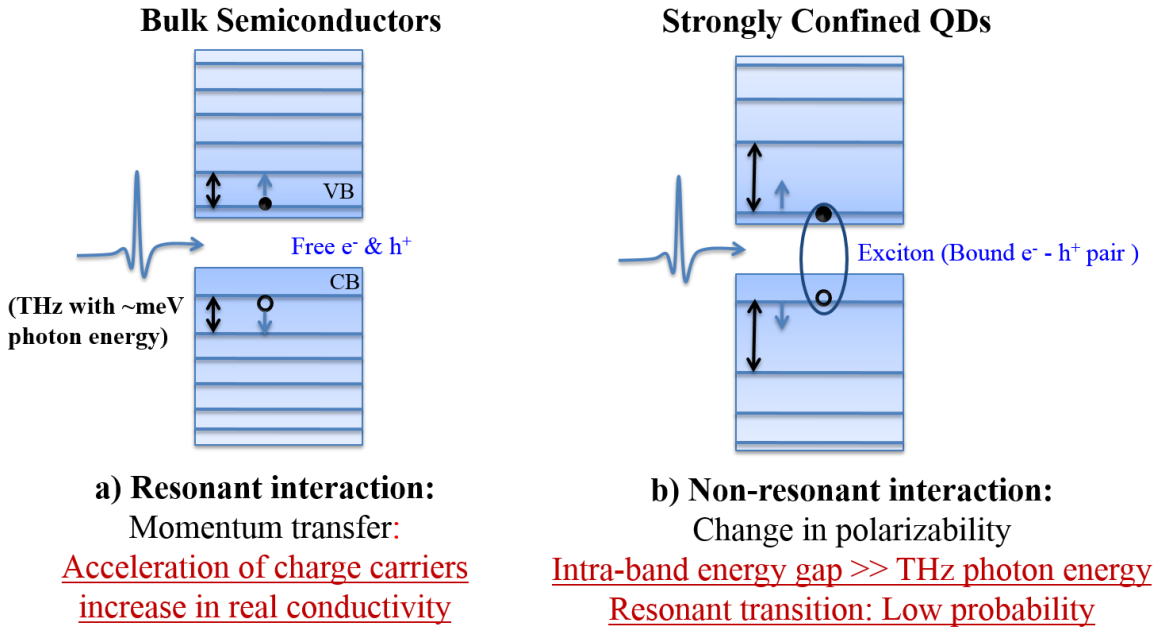

Figure 7. *Interaction of THz radiation and photoexcited charge carriers through a) Resonant interaction and b) Non-resonant interaction.*

1.2.2 Photoexcited semiconductor processes

Ultrashort laser pulse with photon energy more than the bandgap of a semiconductor generates excited-state charge carriers. Photoexcited charge carriers undergo a series of fast relaxation processes to reach equilibrium with lattice, such as carrier-carrier scattering and carrier-lattice scattering.[31-33] Time scales for these processes are of the order of hundreds of femtoseconds. Once photocarriers reach equilibrium with lattice by releasing excess energy, recombination processes start. In semiconductors, defect states are present and they can trap the charge carriers within timescales less than 100 picoseconds. Since a charge carrier gets trapped in a defect state, it remains trapped for a long time, and it could recombine after a very long time. This is a monomolecular process known as trap-assisted recombination. At the same time, depending on the photocarrier density present in semiconductors, electron-hole recombination happens by emitting photons; this process is known as the bimolecular recombination process. If carrier density is very high, the emitted photon due to electron-hole recombination excites other charge carrier in further excited state. The photon emitted in this process does not come out of the system, so it is a non-radiative type of recombination. This is a many-particle process known

as the Auger-recombination process. Three particles are involved in this process, also called a tri-molecular process.

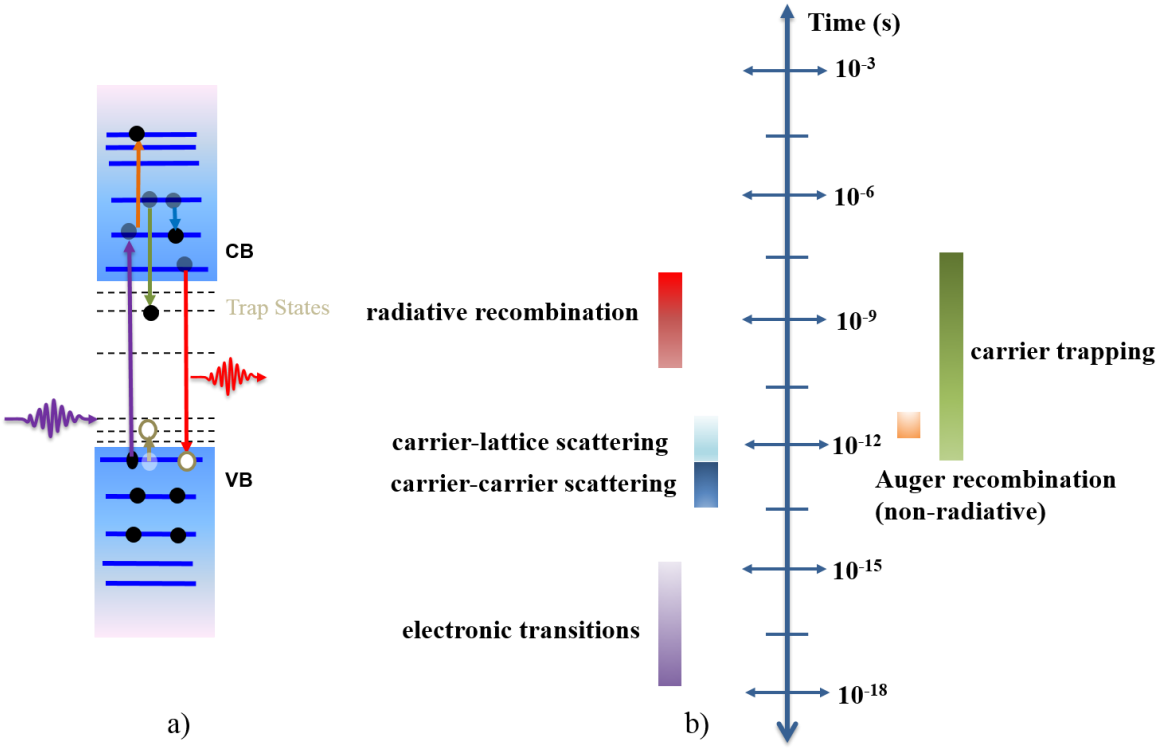

Figure 8. *a) Electrons (holes) undergo various relaxation/recombination processes after photoexcitation of semiconductor and b) Time scales (tentative) in photoexcited semiconductor corresponding to relaxation and recombination processes.*

All these recombination processes occur at different timescales (tentative time scales are shown in Figure 8). Auger-recombination is the fastest process, typically associated with time constants below 50 ps and occurs at very high photocarrier density. Bimolecular recombination is more rapid in the timescale than monomolecular trap-assisted recombination. Trap-assisted recombination is the slowest process and can happen over a microsecond (μs) timescale. This is a general, qualitative description of recombination processes occurring in photoexcited inorganic semiconductors shown in Figure 8b. These timescales may vary from one semiconductor to another and depend on many other internal and external factors, such as particle size, quantum confinement, temperature of the system under study etc. Apart from these processes, there are other channels through which relaxation and recombination may take place in a semiconductor (depending on many physical factors like size, shape, thickness,

exciton binding energy etc.), such as biexciton recombination, trion formation, polaron formation etc. Monomolecular, bimolecular and trimolecular processes are mathematically represented and understood by the well-known kinetic rate equation[34], given by equation 8

$$\frac{dn}{dt} = -k_1 n - k_2 n^{\,2} - k_3 n^{\,3} \tag{8}$$

Here, n is the photogenerated carrier density. k_1, k_2, and k_3 represent rate constants for monomolecular, bimolecular, and trimolecular recombination processes respectively. As time-resolved THz spectroscopy monitors photoexcited carrier density with pump-probe delay after optically exciting a semiconductor, we can experimentally determine the fundamental kinetic rate constants (k_1, k_2, and k_3) for a particular semiconductor.

1.3 Plan of the Thesis

This thesis describes the study of charge carrier dynamics in semiconductor materials ranging from low bandgap to high bandgap. Thallium halides (TlBr, TlI), Indium Selenide (InSe), Thallium Selenide (TlSe), and Black Phosphorus semiconductors are studied by THz time-domain spectroscopy and time-resolved THz spectroscopy. Thallium halide is a wide bandgap semiconductor having its bandgap in the UV region. Thallium halides are expected to behave as a defect-tolerant semiconductor system, leading to perovskite-like properties due to their band structure similarity with metal halide perovskites.[35, 36] Indium selenide (InSe) and thallium selenide (TlSe) are intermediate and narrow bandgap semiconductors, respectively. These are potential thermoelectric materials as they have recently shown ultralow/low thermal conductivity.[37, 38] Indium Selenide and Black Phosphorus are two-dimensional (2D) van der Waals semiconductors that have recently attracted much attention due to their promising optoelectronic properties.[39-41] Both Indium Selenide and Black Phosphorus have layer-dependent bandgaps. Indium Selenide and Thallium Selenide are studied in their bulk form. Few-layer Black Phosphorus nanoparticles film, Thallium Halides nanocrystals thin film and Thallium Halides bulk thin films are investigated using THz spectroscopic techniques.

1.4 References

1. Baxter, J. B.; Guglietta, G. W., Terahertz Spectroscopy. *Analytical Chemistry* **2011,** *83* (12), 4342-4368.
2. Zeitler, J. A.; Shen, Y.-C., Industrial Applications of Terahertz Imaging. In *Terahertz Spectroscopy and Imaging*, Peiponen, K.-E.; Zeitler, A.; Kuwata-Gonokami, M., Eds. Springer Berlin Heidelberg: Berlin, Heidelberg, **2013**; pp 451-489.
3. Wietzke, S.; Jansen, C.; Jördens, C.; Krumbholz, N.; Vieweg, N.; Scheller, M.; Shakfa, M. K.; Romeike, D.; Hochrein, T.; Mikulics, M.; Koch, M. In *Industrial applications of THz systems*, Proc.SPIE, **2009**; p 738506.
4. Al-Douseri, F. M.; Chen, Y.; Zhang, X. C., THz wave sensing for petroleum industrial applications. *International Journal of Infrared and Millimeter Waves* **2006,** *27* (4), 481-503.
5. Ulbricht, R.; Hendry, E.; Shan, J.; Heinz, T. F.; Bonn, M., Carrier dynamics in semiconductors studied with time-resolved terahertz spectroscopy. *Reviews of Modern Physics* **2011,** *83* (2), 543-586.
6. Jepsen, P. U.; Cooke, D. G.; Koch, M., Terahertz spectroscopy and imaging – Modern techniques and applications. *Laser & Photonics Reviews* **2011,** *5* (1), 124-166.
7. García de Arquer, F. P.; Talapin, D. V.; Klimov, V. I.; Arakawa, Y.; Bayer, M.; Sargent, E. H., Semiconductor quantum dots: Technological progress and future challenges. *Science 373* (6555), eaaz8541.
8. YU, P.; Cardona, M., *Fundamentals of Semiconductors: Physics and Materials Properties*. Springer Berlin Heidelberg: **2010**.
9. Klimov, V. I., *Nanocrystal Quantum Dots*. CRC Press: **2017**.
10. Yu, B.; Zhang, C.; Chen, L.; Qin, Z.; Huang, X.; Wang, X.; Xiao, M., Ultrafast dynamics of photoexcited carriers in perovskite semiconductor nanocrystals. **2020,** *10* (8), 1943-1965.
11. Soglin, A.; Gudgel, D. Is Your Laser Pointer Dangerous Enough to Cause Eye Injury? https://www.aao.org/eye-health/news/laser-pointer-eye-injury.
12. Li, Y.; Ye, J.; Yuan, K.; Zhai, G.; Li, T.; Ye, Y.; Wu, X.; Zhang, X., Photo-excited carrier relaxation dynamics in two-dimensional InSe flakes. *Nanotechnology* **2020,** *31* (9), 095713.
13. Shedding light on why blue LEDs are so tricky to make. https://www.ucl.ac.uk/mathematical-physical-sciences/news/2015/jan/shedding-light-why-blue-leds-are-so-tricky-make.
14. Neamen, D. A., *Semiconductor Physics and Devices: Basic Principles*. McGraw-Hill Higher Education: **2012**.
15. Konstantatos, G.; Sargent, E. H., *Colloidal Quantum Dot Optoelectronics and Photovoltaics*. Cambridge University Press: **2013**.
16. Long, M.; Wang, P.; Fang, H.; Hu, W., Progress, Challenges, and Opportunities for 2D Material Based Photodetectors. *Advanced Functional Materials* **2019,** *29* (19), 1803807.
17. Androulakis, J.; Peter, S. C.; Li, H.; Malliakas, C. D.; Peters, J. A.; Liu, Z.; Wessels, B. W.; Song, J.-H.; Jin, H.; Freeman, A. J.; Kanatzidis, M. G., Dimensional Reduction: A Design Tool for New Radiation Detection Materials. *Advanced Materials* **2011,** *23* (36), 4163-4167.

18. Kakavelakis, G.; Gedda, M.; Panagiotopoulos, A.; Kymakis, E.; Anthopoulos, T. D.; Petridis, K., Metal Halide Perovskites for High-Energy Radiation Detection. *Advanced Science* **2020,** *7* (22), 2002098.
19. Yang, T.; Li, F.; Zheng, R., Recent advances in radiation detection technologies enabled by metal-halide perovskites. *Materials Advances* **2021,** *2* (21), 6744-6767.
20. Lloyd-Hughes, J.; Jeon, T.-I., A Review of the Terahertz Conductivity of Bulk and Nano-Materials. *Journal of Infrared, Millimeter, and Terahertz Waves* **2012,** *33* (9), 871-925.
21. Sarkar, S.; Saha, D.; Banerjee, S.; Mukherjee, A.; Mandal, P., Broadband terahertz dielectric spectroscopy of alcohols. *Chemical Physics Letters* **2017,** *678*, 65-71.
22. George, P. A.; Strait, J.; Dawlaty, J.; Shivaraman, S.; Chandrashekhar, M.; Rana, F.; Spencer, M. G., Ultrafast Optical-Pump Terahertz-Probe Spectroscopy of the Carrier Relaxation and Recombination Dynamics in Epitaxial Graphene. *Nano Letters* **2008,** *8* (12), 4248-4251.
23. Kar, S.; Jayanthi, S.; Freysz, E.; Sood, A. K., Time resolved terahertz spectroscopy of low frequency electronic resonances and optical pump-induced terahertz photoconductivity in reduced graphene oxide membrane. *Carbon* **2014,** *80*, 762-770.
24. Wang, F.; Shan, J.; Islam, M. A.; Herman, I. P.; Bonn, M.; Heinz, T. F., Exciton polarizability in semiconductor nanocrystals. *Nature Materials* **2006,** *5* (11), 861-864.
25. Hendry, E.; Koeberg, M.; Bonn, M., Exciton and electron-hole plasma formation dynamics in ZnO. *Physical Review B* **2007,** *76* (4), 045214.
26. Kaindl, R. A.; Carnahan, M. A.; Hägele, D.; Lövenich, R.; Chemla, D. S., Ultrafast terahertz probes of transient conducting and insulating phases in an electron–hole gas. *Nature* **2003,** *423* (6941), 734-738.
27. Yettapu, G. R.; Talukdar, D.; Sarkar, S.; Swarnkar, A.; Nag, A.; Ghosh, P.; Mandal, P., Terahertz Conductivity within Colloidal CsPbBr3 Perovskite Nanocrystals: Remarkably High Carrier Mobilities and Large Diffusion Lengths. *Nano Letters* **2016,** *16* (8), 4838-4848.
28. Nienhuys, H.-K.; Sundström, V., Influence of plasmons on terahertz conductivity measurements. *Applied Physics Letters* **2005,** *87* (1), 012101.
29. Titova, L. V.; Cocker, T. L.; Cooke, D. G.; Wang, X.; Meldrum, A.; Hegmann, F. A., Ultrafast percolative transport dynamics in silicon nanocrystal films. *Physical Review B* **2011,** *83* (8), 085403.
30. Titova, L. V.; Cocker, T. L.; Cooke, D. G.; Wang, X.; Meldrum, A.; Hegmann, F. A., Erratum: Ultrafast percolative transport dynamics in silicon nanocrystal films [Phys. Rev. B 83, 085403 (2011)]. *Physical Review B* **2011,** *83* (15), 159903.
31. Othonos, A., Probing ultrafast carrier and phonon dynamics in semiconductors. *Journal of Applied Physics* **1998,** *83* (4), 1789-1830.
32. Nozik, A. J., *Spectroscopy and Hot Electron Relaxation Dynamics in Semiconductor Quantum Wells and Quantum Dots*. *Annual Review of Physical Chemistry* **2001,** *52* (1), 193-231.
33. Shah, J.; Telephone, A.; Company, T.; Labs, B.; Cardona, M.; Technologies, L.; Innovations, B. L.; Fulde, P.; Klitzing, K. V.; Queisser, H. J., *Ultrafast Spectroscopy of Semiconductors and Semiconductor Nanostructures*. Springer: **1999**.
34. Herz, L. M., Charge-Carrier Dynamics in Organic-Inorganic Metal Halide Perovskites. *Annual Review of Physical Chemistry* **2016,** *67* (1), 65-89.

35. Mir, W. J.; Warankar, A.; Acharya, A.; Das, S.; Mandal, P.; Nag, A., Colloidal thallium halide nanocrystals with reasonable luminescence, carrier mobility and diffusion length. *Chemical Science* **2017,** *8* (6), 4602-4611.
36. Brandt, R. E.; Stevanović, V.; Ginley, D. S.; Buonassisi, T., Identifying defect-tolerant semiconductors with high minority-carrier lifetimes: beyond hybrid lead halide perovskites. *MRS Communications* **2015,** *5* (2), 265-275.
37. Shi, H.; Wang, D.; Xiao, Y.; Zhao, L.-D., Dynamic carrier transports and low thermal conductivity in n-type layered InSe thermoelectrics. *Aggregate* **2021,** *2* (4), e92.
38. Dutta, M.; Matteppanavar, S.; Prasad, M. V. D.; Pandey, J.; Warankar, A.; Mandal, P.; Soni, A.; Waghmare, U. V.; Biswas, K., Ultralow Thermal Conductivity in Chain-like TlSe Due to Inherent Tl+ Rattling. *Journal of the American Chemical Society* **2019,** *141* (51), 20293-20299.
39. Dai, M.; Gao, C.; Nie, Q.; Wang, Q.-J.; Lin, Y.-F.; Chu, J.; Li, W., Properties, Synthesis, and Device Applications of 2D Layered InSe. *Advanced Materials Technologies* **2022,** *n/a* (n/a), 2200321.
40. Miao, J.; Zhang, L.; Wang, C., Black phosphorus electronic and optoelectronic devices. *2D Materials* **2019,** *6* (3), 032003.
41. Ling, X.; Wang, H.; Huang, S.; Xia, F.; Dresselhaus, M. S., The renaissance of black phosphorus. *Proceedings of the National Academy of Sciences* **2015,** *112* (15), 4523-4530.

Chapter 2

Experimental Methods and Data Analysis

2.1 Generation and Detection of THz Radiation

Before the 1990s, it was a technical challenge to generate and detect THz radiations. After the invention of ultrafast lasers, access to THz radiations became possible. Initially, THz radiation was mainly generated using two classical methods, namely photoconductive antennas (above band gap photoexcitation of charge carrier under bias field) and optical rectification (second-order nonlinear effect in medium).[1-3] Detection of the THz field is successfully demonstrated by the processes opposite to the generation methods.[1-3] Several limitations of both the approaches result in generating and detecting only a narrow band of THz frequency region. In photoconductive antennas, generation and detection are limited by the pulse width of the excitation laser and the response time of materials due to their resonant nature. In optical rectification, lattice vibrations of the nonlinear crystal remain the leading cause of low bandwidth of THz radiations. In the early 21st century, scientists found another way of generating and detecting THz radiations using ultrafast laser pulses focused in dry ambient air.[1] This method exploits third-order non-linearity of air-plasma, producing and detecting broadband THz radiation (Figure 1 and Figure 2). In this thesis, we have built and developed THz spectroscopic techniques based on air-plasma generation and detection methods, known as the air-photonic method.[4] Since air is easily replaceable and damage to the medium is not a significant problem, a very intense laser source has been used to generate THz radiations. Moreover, air can produce continuous coverage along with the broadband THz band due to the absence of phonon modes. THz pulses are generated by focusing the fundamental wavelength of 800 nm and its second harmonic of the wavelength of 400 nm in dry air, creating an intense air plasma. Together with the THz radiation, white light and other radiations of electromagnetic spectra are also generated in air plasma. THz detection is possible using the air-biased coherent detection (ABCD) method.

2.1.1 THz Generation

The four-wave mixing (FWM) model, based on the third-order nonlinear process, is used to explain THz generation in ambient air.[5] The fundamental optical radiation of angular frequency ω (corresponds to wavelength of 800 nm in this case) is mixed with its second harmonic of angular frequency 2ω. Second harmonic is generated in type I β-barium borate

crystal (BBO crystal) having a thickness of 0.1 mm. In FWM, THz photon is produced due to the coupling of three photons (two photons of fundamental and one photon of its second harmonics) simultaneously as per the following equation.

$$(2\omega + \omega_{THz}) - \omega - \omega - \omega_{THz} = 0 \quad (1)$$

THz generation in non-ionised air is extremely weak. Hence, ionised air is necessary to enhance the perturbative effect using a strong laser to generate reasonably intense THz radiation. Here, we use an amplified laser source having ~1.8 mJ per pulse energy to create an air plasma. Above the ionisation threshold, THz electric field is proportional to intensities of fundamental and its second harmonics as given in the following relation,

$$E_{THz} \propto \chi^{(3)} \sqrt{I_{2\omega}} I_{\omega} \quad (2)$$

here, $\chi^{(3)}$ is third-order nonlinear coefficient and equal to 1.68 x 10^{-25} (m/V) at 20° C in air. It is essential to mention the dependence of the THz electric field on the phase (ϕ) between the fundamental and its second harmonics electric fields. This phase change decides the sign of the THz electric field. The following equation 3 shows the electric field of the individual photon.

$$E_{THz}(t) \propto \chi^{(3)} E_{2\omega}(t) E_{\omega}^{*}(t) E_{\omega}^{*}(t) \cos(\phi) \quad (3)$$

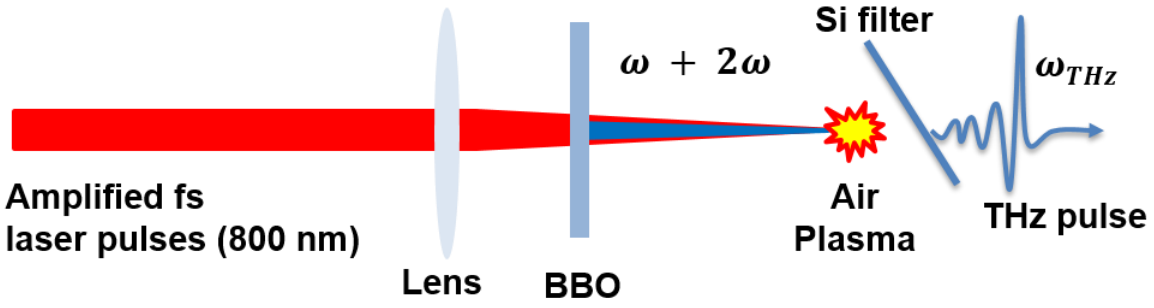

Figure 1. *Generation of THz pulse in laser induced-air plasma.*

2.1.2 THz Detection

Detection of THz electric field is carried out using laser-induced air-plasma by the process opposite to generation.[6] Here, two input photons of fundamental frequency (ω) and one

photon of THz frequency (ω_{THz}) are coupled in a weak air-plasma medium. As a result, a photon of the second harmonics of fundamental frequency (2ω) is generated. The following relation (equation 4) gives THz field-induced second harmonics, representing a four-wave mixing process.

$$2\omega = \omega + \omega \mp \omega_{THz} \tag{4}$$

The electric field of generated second harmonics is given by,

$$E_{2\omega} \propto \chi^{(3)} E_{\omega} E_{\omega} E_{THz} \tag{5}$$

The intensity of second harmonics is measured, which indirectly measures the intensity of THz radiation, as other terms in the expression are known

$$I_{2\omega} \propto \left| E_{2\omega} \right|^2 \propto (\chi^{(3)})^2 \, I_{\omega}^2 \, E_{THz}^2 \tag{6}$$

It should be noted that the measured signal is directly proportional to the intensity of the THz field, i.e., to the square of the THz field. As a result, the information about the phase of the electric field is lost, and the detection becomes incoherent (only the amplitude of the electric field can be measured).

For coherent detection of the entire THz electric field (both amplitude and phase of electric field), a local oscillator is introduced in the form of a AC bias field. This AC bias field, i.e., local oscillator (LO), produces the second harmonic from air-plasma created by fundamental frequency i.e.,

$$E_{2\omega} \propto \chi^{(3)} E_{\omega} E_{\omega} (E_{THz} + E_{LO}) \tag{7}$$

This can be written in the intensity form as below,

$$I_{2\omega} \propto \left| E_{2\omega} \right|^2 \propto (\chi^{(3)})^2 \, I_{\omega}^2 (E_{THz}^2 + E_{LO}^2 + 2E_{THz} E_{LO}) \tag{8}$$

The last term in the bracket of the above equation 8 represents the cross term, and the heterodyne method of detection of such signal becomes important, which allows coherent detection. We need to only measure the last term by using an AC electric field as the LO and detect the signal modulated with LO frequency. Hence, the measured signal is proportional to the THz electric field, as shown in equation 9.

$$I_{2\omega} \propto |E_{2\omega}|^2 \propto (\chi^{(3)})^2 I_{\omega}^2 (E_{THz} E_{LO}) \quad (9)$$

Here, we can enhance the strength of the measured signal simply by increasing the power of the fundamental frequency and the AC bias field. Figure 2 represents a schematic of the detection of THz pulse through the ABCD method.

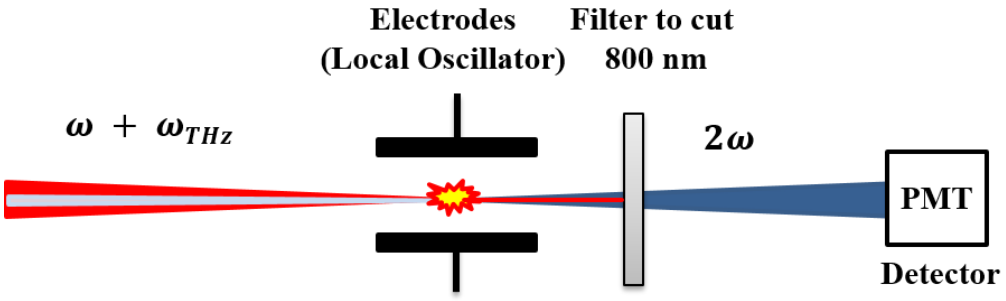

***Figure 3**. Detection of THz pulses in air plasma.*

2.2 Experimental Setups of THz-TDS and TRTS

Our home-built THz spectroscopy setup is based on an ultrafast laser system, primarily consisting of a Ti:sapphire-based oscillator (Tsunami, Spectra-Physics) and amplifier (Spitfire, Spectra-Physics). The ultrafast laser pulses coming out of the amplifier have a central wavelength of 800 nm and an average power of 4 W, i.e., 4 mJ energy per pulse with a repetition rate of 1 kHz. This laser pulse beam is split into two parts.[4] Half of the power (around 2 W) is utilised for generation (~92% of 2 W) and detection (~8% of 2 W) of THz radiation, and the remaining half of the power (around 2 W) is sent to the pump an optical parametric amplifier (OPA), which generates laser pulses of different wavelengths by nonlinear optical effects. The THz radiations, which are produced in air plasma along with white light and other parts of electromagnetic radiations, are filtered by placing a silicon wafer with high resistivity in the laser path. The THz pulses are then sequentially guided using parabolic mirrors to be detected by a photomultiplier tube (PMT) placed inside an ABCD detector (Zomega). Inside the detector, the THz pulses and the weak gate pulse of a wavelength of 800 nm are focused between high-voltage electrodes (AC bias) with a voltage of 1.5 kV, and that oscillate in square waveform with a frequency of 500 Hz, which acts as a local oscillator (LO). By fundamental and THz pulses, 400 nm pulses are generated via the

difference frequency generation method (i.e., four-wave mixing method). The intensity of 400 nm pulses is directly proportional to the THz electric field, as discussed in the above section. The entire THz generation and detection paths are continuously purged with dry nitrogen gas (inside the box) to avoid THz absorption in the water vapour in normal air.

The THz radiation is detected by temporally scanning a weak 800 nm femtosecond optical beam over a relatively long THz pulse (picosecond in time), using the cross-correlation of these two beams.[3] This method has been used to detect broadband THz radiation up to 15 THz in our lab. THz time-domain signal and its Fourier transform are shown in Figure 5. The pump pulse (used to photoexcite the sample/material) is obtained from the OPA output.[3] The OPA produces different frequencies by nonlinear processes such as white light generation, sum-frequency generation, and difference frequency generation. The photocurrent generated in the PMT of the ABCD detector is amplified with a pre-amplifier (SRS model SR570) and is converted into voltage. This voltage serves as input for the lock-in amplifier (SRS model SR830 DSP) referenced to the frequency of LO. The lock-in output is digitised with DAQ card (National Instrument), and the outcome is visualised and stored using LabView programmes.

2.2.1 THz Time-Domain Spectroscopy (THz-TDS)

To study dielectric response, complex refractive index, and low energy excitations in materials, THz time-domain spectroscopy (THz-TDS) is performed on various solid materials and liquids. THz-TDS can be implemented both in transmission and reflection geometries, and the choice of geometry of the experiment depends on the sample to be studied. In this thesis, we have used THz-TDS in both the modes (geometries) to study semiconductor film coated on non-conducting substrates and bulk semiconductors.[7, 8]

a) THz-TDS in transmission geometry

In THz time-domain THz spectroscopy (THz-TDS) in transmission geometry, the THz radiation propagating in free space is passed directly through the reference and the sample. THz spectroscopy is a coherent method that detects the amplitude and phase of the electric field of the freely propagating THz radiation, in contrast to other optical spectroscopy methods, such as UV-visible spectroscopy. The reference signal is the electric field of THz

radiation passing through air or a non-conductive substrate such as high-density polyethylene (HDPE) and polystyrene. A quartz substrate is used as a reference in various studies. The sample can be a pellet or a thin or thick layer on the substrate. The sample signal is the electric field of the THz radiation passing through the pellet or film layer on the substrate. Experimentally, the transmission function $\tilde{T}(\omega)$ is measured by taking the Fourier transform of time-domain signals.

$$\tilde{T}(\omega) = \frac{\tilde{E}_s(\omega)}{\tilde{E}_r(\omega)} = \frac{E_s(\omega)}{E_r(\omega)} e^{i\varphi(\omega)} = T(\omega) e^{i\varphi(\omega)} \quad (10)$$

Here, $\tilde{E}_s(\omega)$ and $\tilde{E}_r(\omega)$ are complex electric fields of sample and reference, respectively, and $\varphi(\omega)$ is the phase shift between the sample and reference. The complex refractive index of the sample is calculated as a function of frequency from $\tilde{T}(\omega)$.

$$\tilde{n}(\omega) = n(\omega) + ik(\omega) \quad (11)$$

Here, n and k are real and imaginary parts of the complex refractive index. α is the absorption coefficient of the sample.

Film/sample suspended in the air

If the reference is air instead of a non-conducting substrate, real (n) and imaginary (k) parts of complex refractive index are obtained using the following relations using experimentally measured quantities, phase(φ) and transmittance (T).

$$n(\omega) = 1 + \varphi(\omega) \frac{\omega d}{c} \quad (12)$$

$$\alpha(\omega) = \frac{2\omega k(\omega)}{c} = \frac{2\omega}{c} \ln\left(\frac{1}{T(\omega)}\right) \quad (13)$$

Thin film coated on the substrate

A non-conducting substrate (HDPE, polystyrene, etc.) is used as a reference in THz-TDS, and the iterative numerical method is followed to obtain the complex refractive index of the sample. The measured transmission coefficient is compared with the model transmission

coefficient. The difference between the measured and model transmittance is iteratively reduced to the minimum to obtain the complex refractive index of the sample. We used Duvillaret's algorithm and the associated Igor code from the doctoral thesis of Paul D. Cunningham to determine the complex refractive index of a thin sample on a thick substrate.[9, 10]

b) THz-TDS in reflection geometry

In this thesis, we studied optically thick bulk semiconductor samples using THz spectroscopy in reflection geometry due to the high absorption nature in the THz frequency range. In reflection geometry, THz radiation is reflected from the reference (here, we use high-resistivity silicon) and sample. Reflection of THz signal (electric field) in normal incidence from the reference and sample is preferred over oblique incidence as it involves relatively simple data analysis and the least error due to optical alignment. In reflection THz TDS, we measured the electric fields of THz radiation reflected from the sample, $\tilde{E}_{sample}(\omega)$ and reference $\tilde{E}_{ref}(\omega)$ and reflectance function is obtained as per the following equation,

$$\tilde{R}(\omega) = \frac{\tilde{E}_{sample}(\omega)}{\tilde{E}_{ref}(\omega)} \tag{14}$$

Fresnel equation for reflection in normal incidence is used to obtain the complex refractive index of the sample, and it is given in equation 15.

$$\frac{\tilde{E}_s(\omega)}{\tilde{E}_r(\omega)} = \frac{\frac{\tilde{n}_{sample} - n_{air}}{\tilde{n}_{sample} + n_{air}}}{\frac{\tilde{n}_{ref} - n_{air}}{\tilde{n}_{ref} + n_{air}}} \tag{15}$$

Here, $\tilde{n}_{sample}$ and $\tilde{n}_{ref}$ are complex refractive indices of sample and reference, respectively. n_{air} is the refractive index of air. In our experiment, we used high-resistivity (HR) Si as a reference. Here, air (dry air, which is mainly composed of nitrogen gas, and HR Si are almost non-absorbing and non-dispersive in the THz frequency range; hence, their refractive indices are considered to have real value.

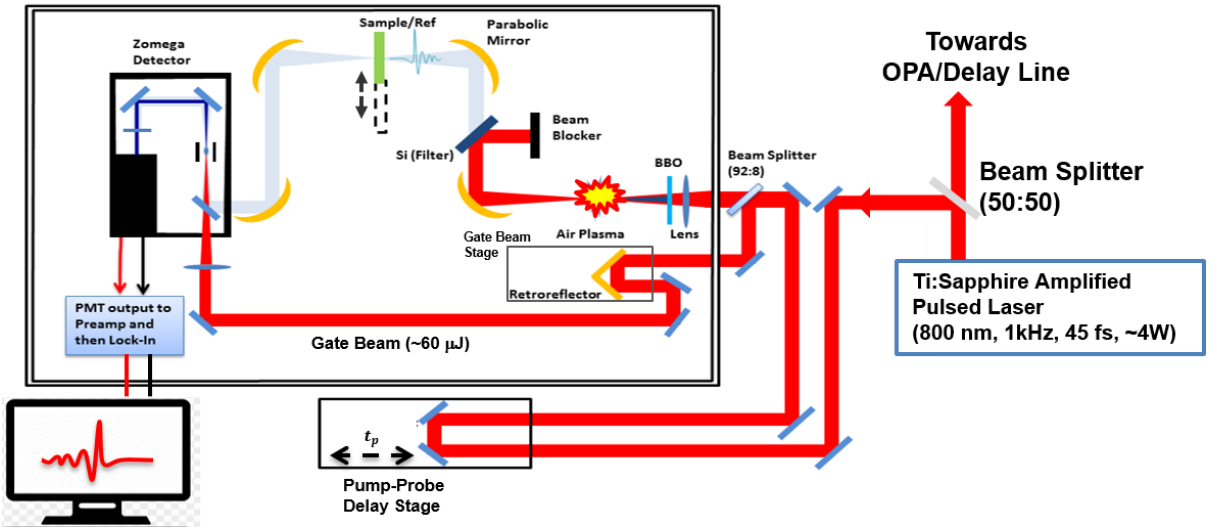

Figure 4. *THz time-domain spectroscopy setup in transmission geometry.*

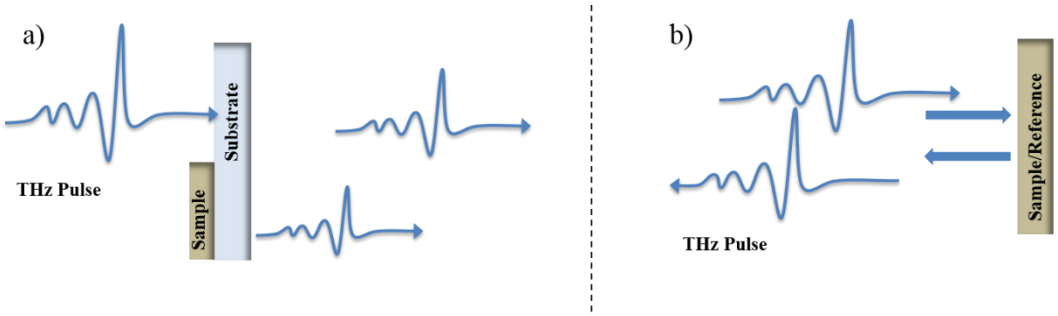

Figure 5. *a) Transmission of THz pulse through reference and sample and b) Reflection of THz pulse from reference and sample.*

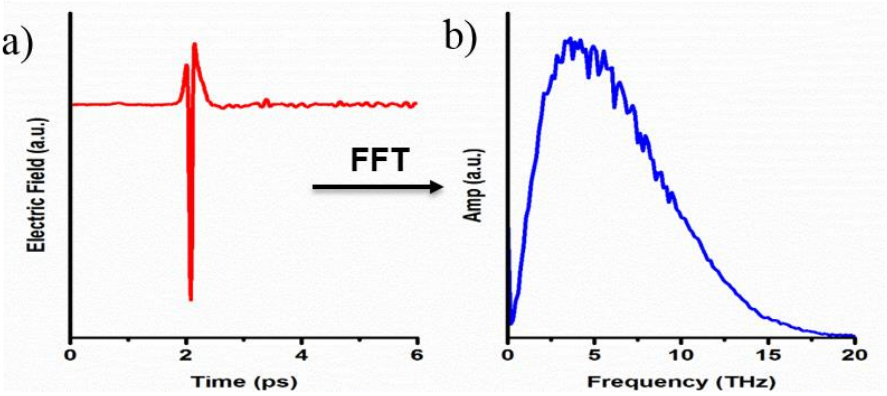

Figure 6. *a) THz time-domain signal and b) THz frequency-domain signal (broadband).*

2.2.2 Time-resolved THz spectroscopy (TRTS)

Time-resolved THz spectroscopy (TRTS) is performed on semiconductors to understand charge carrier dynamics. Although several time-resolved THz studies (pump-probe studies) were conducted by a few research groups on technologically important semiconductors such as gallium arsenide (GaAs) and Si[11-15], the TRTS technique was pioneered by doing detailed and systematic experiments on GaAs by Charles Schmuttenmaer's group at Yale University in the year 2000.[16] Over the past 20 years, it has been established as one of the important ultrafast techniques for studying photophysical properties in various materials.[17] Based on the optical and physical properties of the semiconductor, one can choose either transmission or reflection mode TRTS.

We have performed TRTS in two different ways to study photoexcited properties of materials: frequency-averaged (pump scan) and frequency-resolved (probe scan) TRTS. TRTS is also known as optical-pump THz-probe (OPTP) spectroscopy. In frequency-averaged (pump scan) TRTS, the peak of the THz electric field is monitored in the absence (E_{off}) and presence (E_{on}) of pump excitation, and the photoinduced change in electric fields ($\Delta E = E_{on} - E_{off}$) is monitored with a pump-probe time delay up to the nanosecond time scale. In frequency-resolved (probe scan) TRTS, photoexcited and unexcited waveforms of the entire time-domain THz electric field are collected at different pump-probe delays. The charge carrier dynamics, the nature of photoexcited charge carriers, and the photoinduced changes in the dielectric function of material are measured from the combination of both TRTS scans.

The double lock-in technique is implemented to simultaneously detect the pump-induced change in THz electric field (ΔE) and non-excited THz electric field (E_{off}).[18, 19] Pump wavelength, which is chopped at 333 Hz using an optical chopper, is used to photoexcite the sample, and THz pulses with a frequency of 1 kHz probe the photoexcited states of the sample. The photocurrent as an output of PMT is sent to the first pre-amplifier, which gets converted into voltage and then to two lock-in amplifiers operating at different reference frequencies 333 Hz (synchronised with the optical chopper) and 500 Hz (half of the laser repetition rate) which is the frequency of the local oscillator.

a) TRTS in transmission mode

Thin films, colloidal nanoparticles and low-absorbing materials (in the THz frequency range) can be studied using TRTS in transmission mode. In this experiment, optical pump-induced change in THz probe pulses (ΔE) is collected.

$$\Delta E(\omega) = E_{on}(\omega) - E_{off}(\omega) \tag{16}$$

Experimentally, photoinduced differential transmission is obtained, which is given by

$$\frac{\Delta T(\omega)}{T(\omega)} = \frac{\Delta E(\omega)}{E_{off}(\omega)} \tag{17}$$

as it is mathematically related to the photoconductivity ($\Delta\sigma$) of the sample studied. *T* is THz transmission through the unexcited sample.

Photoconductivity ($\Delta\sigma$) of the film is related to differential transmission as per the following expression.

$$\Delta\sigma = -\frac{(n_a + n_b)}{z_0\, d}\,\frac{\Delta E}{E_{off}} \tag{18}$$

Here, n_a and n_b represent refractive indices of either side of the photoexcited sample, and d represents the thickness of the films. z_0 is free space impedance, $z_0 = \frac{1}{\varepsilon_0 c} \sim 377\ \Omega$.

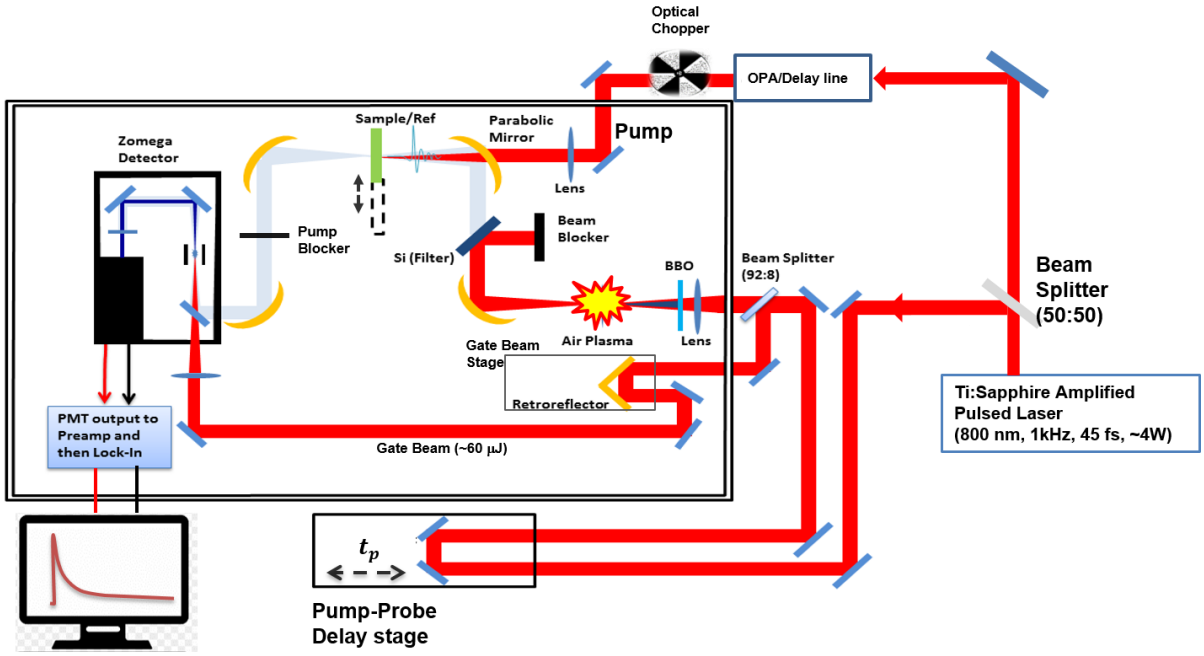

Figure 7. *Setup of time-resolved THz spectroscopy in transmission geometry.*

b) TRTS in reflection mode

Photoexcited properties of highly absorbing materials in the THz frequency range and optically thick materials are studied using time-resolved THz spectroscopy in reflection mode. In this thesis, we have utilised TRTS in normal incidence reflection mode. Photoinduced change in reflectance (ΔR) from the sample is measured, here $\Delta R = R_{on} - R_{off}$, R_{on} is the reflectance in a photoexcited state and R_{off} is the reflectance in the unexcited state of the sample. For measuring photoconductivity ($\Delta\sigma$), differential reflectance is obtained by dividing R_{off} to ΔR

$$\frac{\Delta R}{R_{off}} = \frac{\Delta E}{E_{off}} \tag{19}$$

The photoconductivity of the sample using thin film approximation can be written in the form of $\frac{\Delta R}{R_{off}}$,

$$\Delta\sigma = \frac{(n^2 - 1)}{2 z_0 d} \frac{\Delta R}{R_{off}} \tag{20}$$

here, n is the low-frequency refractive index (for pump scan) or frequency-dependent refractive index (for probe scan) of the sample z_0 $(1/\varepsilon_0 c)$ is free space impedance, and d is the penetration depth of the sample at the pump wavelength.

Photoconductivity equation as the function of pump-probe delay time (t_p) and angular frequency (ω) using thin film approximation is given in Table 1 below.

Table 1. *Photoconductivity equation according to thin-film approximation.*

	Frequency-averaged (Pump scan)	Frequency-resolved (Probe scan)
Photoconductivity (Transmission Geometry)	$\Delta\sigma(t_p) = \frac{1}{z_0 d}(n_a + n_b)\frac{-\Delta E(t_p)}{E_0(t_p)}$	$\Delta\sigma(\omega) = \frac{1}{z_0 d}(n_a + n_b)\frac{-\Delta E(\omega)}{E_0(\omega)}$
Photoconductivity (Reflection Geometry)	$\Delta\sigma(t_p) = \frac{(n^2-1)}{2z_0 d}\frac{\Delta E(t_p)}{E_0(t_p)}$	$\Delta\sigma(\omega) = \frac{(n^2-1)}{2z_0 d}\frac{\Delta E(\omega)}{E_0(\omega)}$

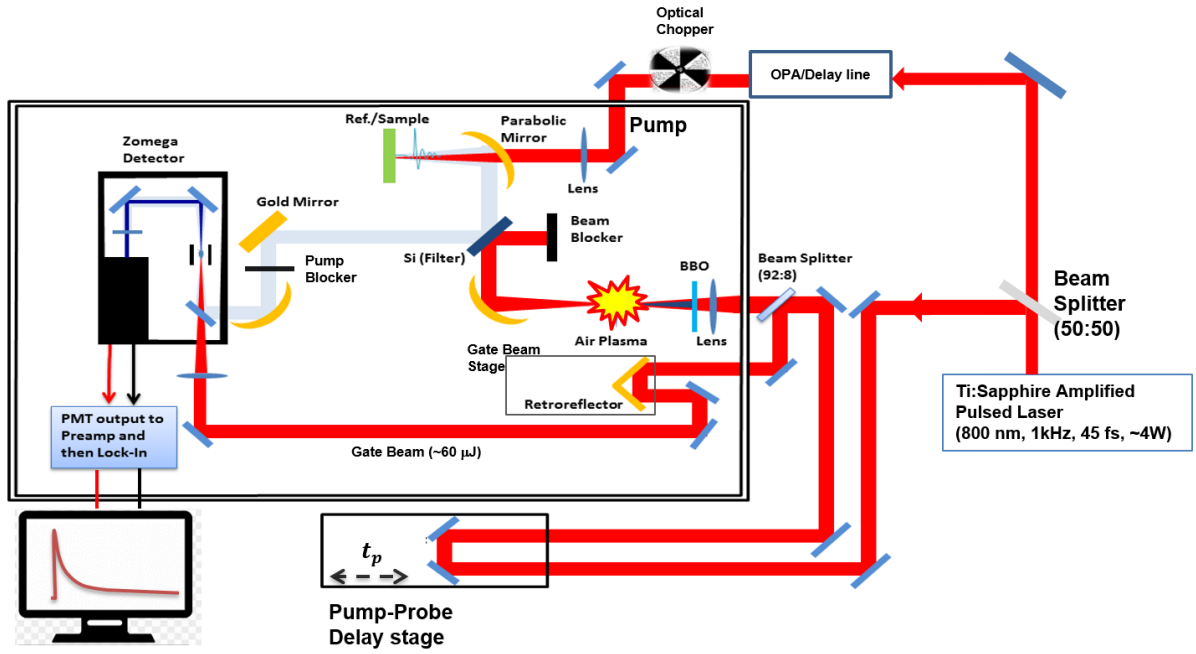

Figure 8. *Setup of time-resolved THz spectroscopy in reflection geometry.*

2.3 Conductivity Models

THz time-domain spectroscopy can measure the steady-state dielectric response of semiconductors and hence obtain steady-state complex conductivity spectra, whereas THz time-resolved spectroscopy measures time-dependent, excited-state photoconductivity. Free carrier, lattice vibration, and other low-frequency excitations contribute to steady-state conductivity and photoconductivity, which can be quantified using various conductivity models, leading to the finding of important material parameters, as discussed below.

2.3.1 Drude model and Drude-Smith model

Free charge carrier response under an external, oscillating electric field in a semiconductor is often described by the semiclassical model developed by Drude.[17, 20] This model is designed for non-interacting electron gas in metals with very high carrier concentrations. Semiconductors in a non-photoexcited state have inherent carrier concentration depending on factors such as doping, temperature, etc. Upon photoexcitation by appropriate pump

wavelength, photocarriers are generated in higher concentrations than the intrinsic concentration. In both cases, the carriers in semiconductors are approximated as free carriers. According to the Drude model, the complex conductivity of free carriers under an external oscillating electric field of angular frequency (ω) is given by,

$$\tilde{\sigma}(\omega) = \frac{\sigma_{dc}}{(1 - i\omega\tau)} \tag{21}$$

here σ_{dc} is direct conductivity (dc). Direct conductivity, in this case, is also known as Drude conductivity (near zero frequency, i.e., ω~0 THz), τ is carrier momentum scattering time. The dc conductivity is related to carrier concentration (n), scattering time (τ) and effective mass (m^*) of carriers.

$$\sigma_{dc} = \frac{ne^2\tau}{m^*} \tag{22}$$

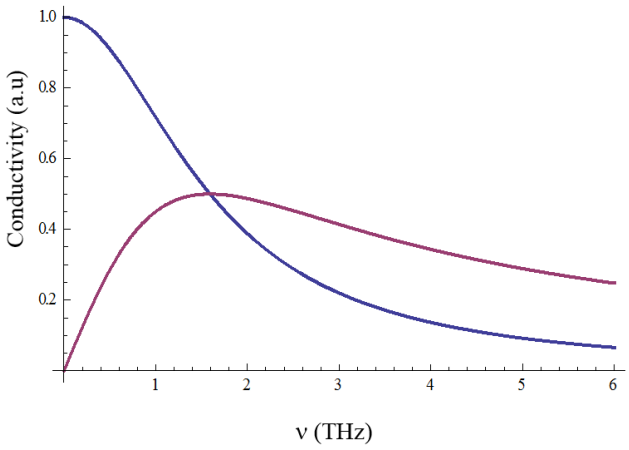

***Figure 9**. Complex conductivity simulated in Mathematica for Drude Model (for τ =100 fs and σ_{dc} = 1 unit. (real conductivity (blue) and imaginary conductivity (purple)).*

The Drude model needs to be modified when charge carriers are confined to a specific region or backscattered, as in the case of nanomaterials, where the movement of carriers is restricted to small dimensions or in two-dimensional (2D) materials, i.e., carriers are confined to the plane. N.V. Smith developed the required modification by incorporating backscattered parameters and a modified conductivity model, now known as the Drude-Smith Model.[21]

$$\tilde{\sigma}(\omega) = \frac{\sigma_{dc}}{(1 - i\omega\tau)}\left(1 + \frac{c}{(1 - i\omega\tau)}\right) \tag{23}$$

Here, c is the parameter that quantifies the percentage of backscattered carriers and varies from 0 (no backscattered) to -1 (completely backscattered). Here σ_{DC} (Drude conductivity), τ, c are fitting parameters while modelling experimental complex conductivity.

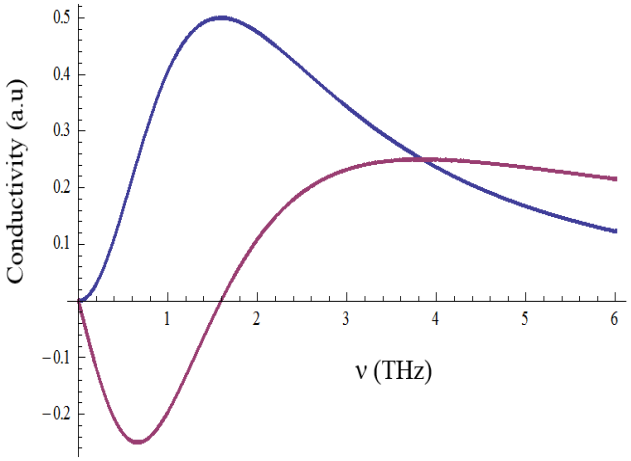

Figure 10. *Complex conductivity simulated in Mathematica for Drude-Smith Model (for τ =100 fs, σ_{dc} = 1 unit and c=-1. (real conductivity (blue) and imaginary conductivity (purple)).*

2.3.2 Lorentz oscillator model

Lorentz model accounts for conductivity arising from low-frequency absorption.[17] Semiconductors absorb THz frequency through low-energy excitation in solids such as phonon vibration, exciton resonances, etc.; this is reflected in peaks in the real part of complex conductivity.[17, 22] Complex conductivity is derived from the Lorentz model in the following expression (equation 24).

$$\tilde{\sigma}(\omega) = \sum_i \frac{\sigma_i \omega}{(\omega - i\tau_i(\omega^2 - \omega_i^2)} \qquad (24)$$

Experimental photoconductivity spectra are fitted to this model in addition to Drude or Drude-Smith model for particular pump-probe delay (t_p). Here σ_i , τ_i , ω_i are fitting parameters while modelling experimental complex conductivity.

a) The fundamental parameter of materials

Fitting experimental complex photoconductivity spectra to the Drude model or Drude-Smith model provides important parameters like charge mobility and carrier density.

$$n(t_p) = \frac{\sigma_{dc} m}{e^2 \tau} \tag{25}$$

$$\mu(t_p) = \frac{e\tau}{m} \tag{26}$$

Oscillator strength (f_i) of i^{th} oscillator with oscillation (resonance) angular frequency (ω_i) is obtained from fitting from oscillator-induced Lorentz conductivity (σ_i) and time (τ_i).

$$f_i = \frac{\sigma_i}{\tau_i} \tag{27}$$

2.4 Modelling recombination processes in semiconductors

We tried to understand the photoinduced recombination processes in semiconductors by analysing fluence-dependent photoinduced THz transients in two ways. The measured signal is a photoinduced change in THz electric fields, which depends on the carrier concentration of the excited states. The change in photoinduced conductivity with pump-probe delay reflects the temporal evolution of carrier concentration. The first approach is to model normalized photoinduced THz transients with multiexponential function convoluted with Gaussian function.[23] The mathematical expression for the same is given in equation 28.

$$y(t) = G(t - t_0) \otimes \frac{\sum_i^n a_i \, exp(t - t_0)}{t_i} \tag{28}$$

Here, $\sum_i^n a_i$=1, is the sum of amplitudes (a_i) corresponding to i^{th} process having a time component t_i. Gaussian function, centred at t_0 is represented by $G(t - t_0)$ and with full width at half maximum (FWHM) is about 300 fs. This Gaussian function represents the instrument response function (IRF) of our TRTS setup. We get different time constants with the corresponding amplitude by fitting the normalized THz transients to equation 28. We can assign physical recombination processes by inspecting the magnitude of time constants and their fluence-dependent behaviour. But modelling THz transients using the above equation will not give a complete and accurate picture of physical processes happening upon photoexcitation due to the assumption of exponential decay functions. We can roughly relate the time evolution of THz transients to the change in carrier density. As every point on THz

transient is related to photoexcited carrier density, we need a model which describes these two quantities. The rate of change of carrier density is proportional to an integer power of carrier density, which can effectively be modelled by the kinetic rate equation. Equation 29 represents the mathematical form of the kinetic rate equation.[24]

$$\frac{dn}{dt} = -k_1 n - k_2 n^{\,2} - k_3 n^{\,3} \qquad (29)$$

Here, the left side term represents the change of carrier density with pump-probe time delay, and the three terms on the right side of the equation represent three distinct recombination processes. The first term on the right side $-k_1 n$ accounts for the trap-assisted recombination process, in which the recombination of excited charge carriers, either electron or hole, happens through the presence of a trap state; it is also called a monomolecular recombination process. The second term $-k_2 n^2$ depends on both charge carriers, electron and hole. It is termed a bimolecular recombination. The third term $-k_3 n^3$ depends on three charge carriers, and it is known as Auger recombination. Bimolecular recombination can be radiative or non-radiative, whereas trimolecular recombination is non-radiative. Auger recombination is the process associated with trimolecular recombination, and it is relevant only at very high carrier density as it depends on the third power of n. k_1, k_2 and k_3 are rate constants of monomolecular, bimolecular and trimolecular recombination processes, respectively. All three processes are shown schematically in Figure 10.

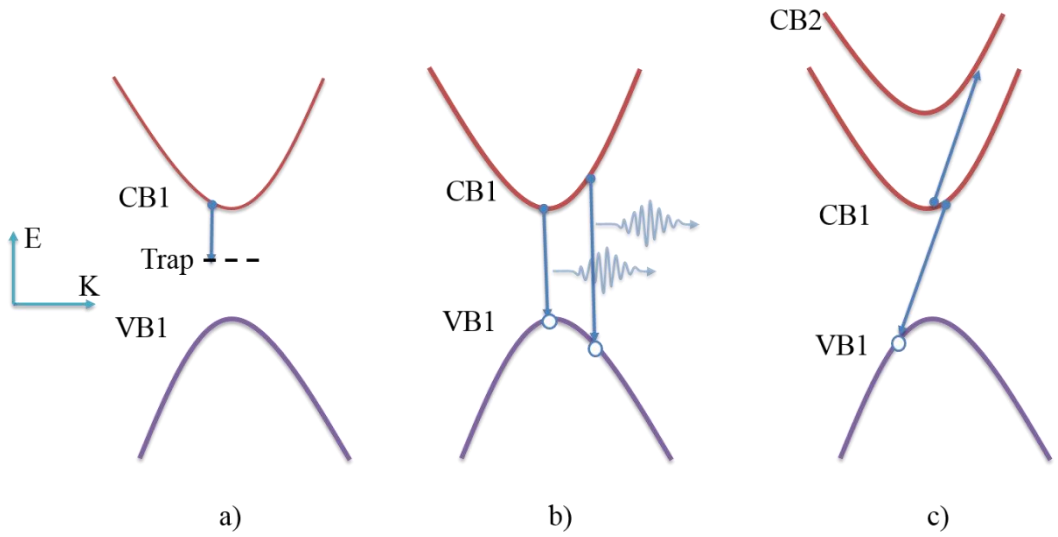

Figure 11. *Schematic of recombination processes in semiconductors a) Monomolecular (trap-assisted process) b) Bimolecular (radiative process) and c) Trimolecular (Auger process).*

a) Numerical procedure for solving kinetic rate equation

We obtained three rate constants by doing a global fitting analysis of fluence-dependent photoinduced THz transients using the kinetic rate equation. It is important to note that solving the rate equation analytically is almost impossible, so we must first solve equation 29 numerically for appropriate initial conditions. Undergraduate student from our lab, Mr. Garvit developed a Python-based code to solve rate equation using a global fitting procedure. Figure 11 shows the steps of a global fitting procedure of photoinduced THz transients using the kinetic rate equation (equation 29).

Here, n is the carrier density, t is the pump-probe time delay, k_1, k_2, k_3 are the rate constants for the recombination processes. We know that $n \propto \frac{\Delta T}{T}$ (where $\frac{\Delta T}{T}$ is differential transmission). This means that $n = C\frac{\Delta T}{T}$ (here C is the proportionality constant, which can be calculated by $\frac{n_0}{x_0}$ (where n_0 is the initial charge carrier density (t_p = 0) and x_0 is the peak differential transmission signal). We assume that, $\frac{\Delta T}{T} = y$ and substitute this equation into the kinetic rate equation, we get,

$$\frac{dy}{dt} = -k_1 y - Ck_2 y^{\,2} - C^{\,2} k_3 y^{\,3} \qquad (30)$$

Let $k_1 = a_1$, $Ck_2 = a_2$, and $C^2 k_3 = a_3$. So, this equation simplifies to equation 31.

$$\frac{dy}{dt} = -a_1 y - a_2 y^2 - a_3 y^3 \tag{31}$$

This is the equation that we have fitted for our data.[24]

b) Euler method for numerical integration

This differential equation is a nonlinear differential equation that is difficult to solve analytically. So, we have numerically integrated the differential equation using the Euler integration method.[25] The primary reason that we chose the Euler method is that it is much faster compared to other integration methods (time is of the order of n, i.e. $O(n)$). As the number of data point we are fitting is of the order 10^6, the algorithm that we used really required to be processed/executed fast. The global error of Euler integration method goes as the order of h, i.e., $O(h)$, where h is the step size. As the step sizes for the data points in our data set were very small, the deviations due to truncation error in Euler will be very small and won't cause many issues.

c) Powell method for minimization

We take the solutions that we get by integrating this equation and define the global chi-squared statistic, which we minimize using the Powell method.[26-28] The Powell method is an iterative minimization method that can be used to estimate local minima for functions. It doesn't calculate any gradients while minimizing functions and has a quadratic termination property; that is, it can minimize quadratic functions in a predetermined number of iterations. As near the local minima, a function tends to act like a quadratic, and also, as the gradients of chi-square with respect to the fitting parameters are very difficult to estimate correctly, Powell method was our method of choice. For the Powell method, the only condition is that a function should be real valued with fixed number of real inputs. As we needed to do a constrained minimization (all three parameters must be non-negative), we used a slightly modified variant of the original Powell method (which is the 'Powell' method used in the

bound constrained minimization methods of the scipy.optimize.minimize function). As the local minimum chosen depends on the initial guess, we tried a lot of initial guesses to find the global minimum. If the results of the Powell method lead to a local minimum (and not a global minimum), the confidence intervals become very large, which lets us know that what we found was a local minimum and not a global minimum.

d) **Calculation of error/confidence interval**

For estimating the 95% confidence intervals for our fit parameters, we have calculated the covariance matrix using the formula $(J^T J)^{-1}\chi^2$ (where J is the Jacobian and χ^2 is the reduced chi-square).[29] The diagonal entries of this matrix give us the variances of the fit parameters. Taking the square root of the variances should give us the standard errors of the fit parameters. By applying the central limit theorem, we can estimate the 95% confidence intervals by multiplying the standard errors by 1.96.[30]

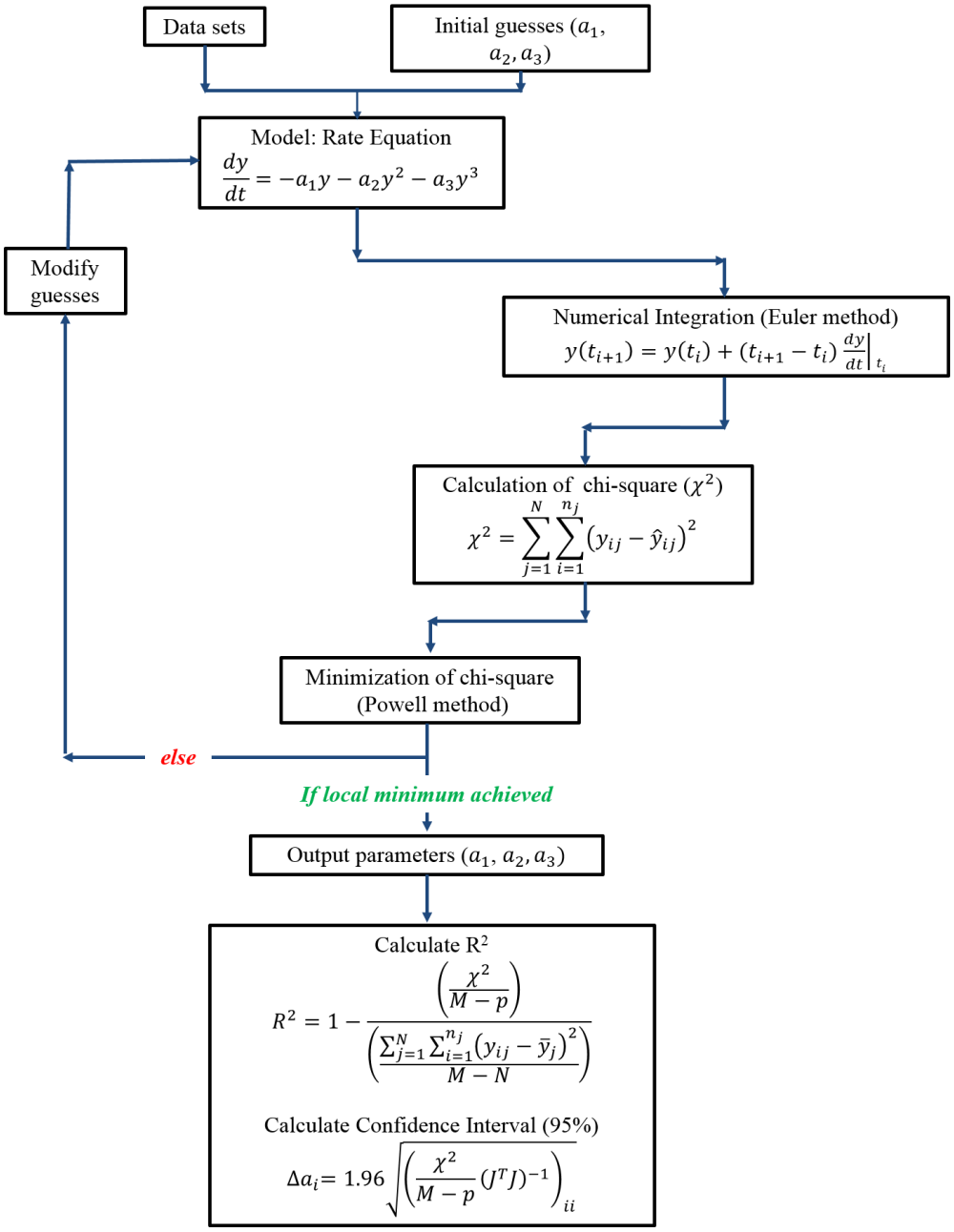

Figure 12. *Steps (flowchart) of global fitting of THz transients using Kinetic rate equation.*

2.5 Optical beam radius measurement by knife-edge method

We used the knife-edge technique for measuring the pump and probe beam diameter in all our experiments. When the knife is moved perpendicular to the optical beam with the surface facing the incoming beam, total power is calculated as a function of knife position. Measured power is the highest when the beam is entirely unblocked and the lowest when the beam is completely blocked (ideally, total power should be zero, but due to background

noise, it may be nearly zero). We used the following relation to fit measured power (p) as a function of knife position (x) to obtain the radius of the optical Gaussian beam.[31]

$$p = p_0 + \frac{p_{max}}{2}\left(1 - \mathrm{erf}\left(\frac{\sqrt{2}(x - x_0)}{w}\right)\right) \tag{32}$$

Where p_0 and p_{max} is background and maximum measured power, respectively. x_0 is the position of the knife (the position of the mechanical stage on which the knife is mounted) at half of the maximum power. erf is the error function, w is the radius of the optical beam.

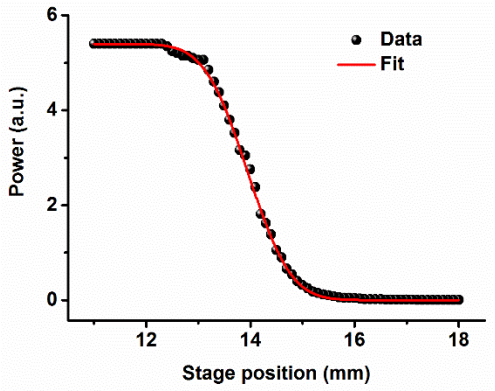

Figure 13. *Typical curve obtained while measuring beam radius and its fit with equation 32.*

2.6 Summary

In this chapter, I have discussed THz frequency generation and detection which are based on the air-photonic method. The two types of THz spectroscopy in both reflection and transmission geometries, THz time-domain spectroscopy and THz time-resolved spectroscopy, are described from the standpoints of their experimental setup and data analysis. THz spectroscopy is used to evaluate steady-state conductivity and photoconductivity; I discussed various models that help in describing experimental conductivity. I have described multiexponential fitting and the kinetic rate equation, two methods for fitting photoinduced THz transients. Python code was used to analyse the numerical solution of the rate equation for experimental data.

2.7 References

1. Zhang, X. C.; Xu, J., *Introduction to THz Wave Photonics*. Springer US: **2009**.
2. Lee, Y. S., *Principles of Terahertz Science and Technology*. Springer US: **2010**.
3. Reid, G. D.; Wynne, K., Ultrafast Laser Technology and Spectroscopy. In *Encyclopedia of Analytical Chemistry*, **2006**.
4. Yettapu, G. R.; Talukdar, D.; Sarkar, S.; Swarnkar, A.; Nag, A.; Ghosh, P.; Mandal, P., Terahertz Conductivity within Colloidal CsPbBr3 Perovskite Nanocrystals: Remarkably High Carrier Mobilities and Large Diffusion Lengths. *Nano Letters* **2016,** *16* (8), 4838-4848.
5. Xie, X.; Dai, J.; Zhang, X. C., Coherent Control of THz Wave Generation in Ambient Air. *Physical Review Letters* **2006,** *96* (7), 075005.
6. Dai, J.; Xie, X.; Zhang, X. C., Detection of Broadband Terahertz Waves with a Laser-Induced Plasma in Gases. *Physical Review Letters* **2006,** *97* (10), 103903.
7. Jana, M. K.; Pal, K.; Warankar, A.; Mandal, P.; Waghmare, U. V.; Biswas, K., Intrinsic Rattler-Induced Low Thermal Conductivity in Zintl Type TlInTe2. *Journal of the American Chemical Society* **2017,** *139* (12), 4350-4353.
8. Dutta, M.; Matteppanavar, S.; Prasad, M. V. D.; Pandey, J.; Warankar, A.; Mandal, P.; Soni, A.; Waghmare, U. V.; Biswas, K., Ultralow Thermal Conductivity in Chain-like TlSe Due to Inherent Tl+ Rattling. *Journal of the American Chemical Society* **2019,** *141* (51), 20293-20299.
9. Duvillaret, L.; Garet, F.; Coutaz, J.-L.; Whitaker, J. F. In *A Reliable Method for the Extraction of Material Parameters of Thick and Thin Samples in THz Time-Domain Spectroscopy*, Ultrafast Electronics and Optoelectronics, Incline Village, Nevada, 1997/03/17; Nuss, M.; Bowers, J., Eds. Optica Publishing Group: Incline Village, Nevada, **1997**; p UF10.
10. Cunningham, P. D., Optical pump terahertz probe studies of semiconducting polymers, Ph.D. Thesis, University of Maryland. **2010**.
11. Nuss, M. C.; Auston, D. H.; Capasso, F., Direct Subpicosecond Measurement of Carrier Mobility of Photoexcited Electrons in Gallium Arsenide. *Physical Review Letters* **1987,** *58* (22), 2355-2358.
12. Greene, B. I.; Federici, J. F.; Dykaar, D. R.; Levi, A. F. J.; Pfeiffer, L., Picosecond pump and probe spectroscopy utilizing freely propagating terahertz radiation. *Optics Letters* **1991,** *16* (1), 48-49.
13. Zielbauer, J.; Wegener, M., Ultrafast optical pump THz ‐ probe spectroscopy on silicon. *Applied Physics Letters* **1996,** *68* (9), 1223-1225.
14. Prabhu, S. S.; Ralph, S. E.; Melloch, M. R.; Harmon, E. S., Carrier dynamics of low-temperature-grown GaAs observed via THz spectroscopy. *Applied Physics Letters* **1997,** *70* (18), 2419-2421.
15. Groeneveld, R. H. M.; Grischkowskyt, D., Picosecond time-resolved far-infrared experiments on carriers and excitons in GaAs–AlGaAs multiple quantum wells. *Journal of the Optical Society of America B* **1994,** *11* (12), 2502-2507.
16. Beard, M. C.; Turner, G. M.; Schmuttenmaer, C. A., Transient photoconductivity in GaAs as measured by time-resolved terahertz spectroscopy. *Physical Review B* **2000,** *62* (23), 15764-15777.
17. Ulbricht, R.; Hendry, E.; Shan, J.; Heinz, T. F.; Bonn, M., Carrier dynamics in semiconductors studied with time-resolved terahertz spectroscopy. *Reviews of Modern Physics* **2011,** *83* (2), 543-586.

18. Iwaszczuk, K.; Cooke, D. G.; Fujiwara, M.; Hashimoto, H.; Jepsen, P. U., Simultaneous reference and differential waveform acquisition in time-resolved terahertz spectroscopy. *Optics Express* **2009,** *17* (24), 21969-21976.
19. D'Angelo, F.; Němec, H.; Parekh, S. H.; Kužel, P.; Bonn, M.; Turchinovich, D., Self-referenced ultra-broadband transient terahertz spectroscopy using air-photonics. *Optics Express* **2016,** *24* (9), 10157-10171.
20. Ashcroft, N. W.; Mermin, N. D., *Solid State Physics*. Cengage Learning: 2011.
21. Smith, N. V., Classical generalization of the Drude formula for the optical conductivity. *Physical Review B* **2001,** *64* (15), 155106.
22. Lloyd-Hughes, J.; Jeon, T.-I., A Review of the Terahertz Conductivity of Bulk and Nanomaterials. *Journal of Infrared, Millimeter, and Terahertz Waves* **2012,** *33* (9), 871-925.
23. Beard, M. C.; Turner, G. M.; Schmuttenmaer, C. A., Size-Dependent Photoconductivity in CdSe Nanoparticles as Measured by Time-Resolved Terahertz Spectroscopy. *Nano Letters* **2002,** *2* (9), 983-987.
24. Herz, L. M., Charge-Carrier Dynamics in Organic-Inorganic Metal Halide Perovskites. *Annual Review of Physical Chemistry* **2016,** *67* (1), 65-89.
25. Kong, Q.; Siauw, T.; Bayen, A., *Python Programming and Numerical Methods: A Guide for Engineers and Scientists*. Elsevier Science: **2020**.
26. Vassiliadis, V. S.; Conejeros, R., Powell methodPowell Method. In *Encyclopedia of Optimization*, Floudas, C. A.; Pardalos, P. M., Eds. Springer US: Boston, MA, **2001**; pp 2001-2003.
27. Powell, M. J. D., An efficient method for finding the minimum of a function of several variables without calculating derivatives. *The Computer Journal* **1964,** *7* (2), 155-162.
28. Press, W. H.; Teukolsky, S. A.; Vetterling, W. T.; Flannery, B. P., *Numerical Recipes 3rd Edition: The Art of Scientific Computing*. Cambridge University Press: **2007**.
29. Fox, J., *An R and S-Plus Companion to Applied Regression*. SAGE Publications: **2002**.
30. Altman, D. G.; Bland, J. M., Standard deviations and standard errors. *BMJ* **2005,** *331* (7521), 903.
31. de Araújo, M. A.; Silva, R.; de Lima, E.; Pereira, D. P.; de Oliveira, P. C., Measurement of Gaussian laser beam radius using the knife-edge technique: improvement on data analysis. *Appl. Opt.* **2009,** *48* (2), 393-396.

Chapter 3

Charge Carrier Dynamics in Thallium Halides (TlX, X=Br, I) Nanocrystals and Bulk Films

3.1 Introduction

Due to the distinct electronic band structure, which is one of the reasons for its defect-tolerance, metal halide perovskite with the formula ABX_3 (where A is an organic/inorganic cation, B is a divalent cation, and X is the halogen anion) is an emerging class of defect-tolerant semiconductors. Defect tolerance is a semiconductor property that allows defect states to have a negligible effect on its optical and electronic properties. Figures 1a and 1b depict the electronic band structure of two types of semiconductors: a) defect-intolerant (inorganic semiconductors) and b) defect-tolerant (metal halide perovskites). The formation of trap states in these two types of semiconductors is very different. High photoluminescence quantum yield (PLQY),[1] tunable bandgap,[1] low threshold lasing,[2] bright light emitting diodes,[3] high-efficiency solar cell[4] etc., are important properties of perovskites semiconductors.

Wide bandgap thallium halides show an electronic band structure similar to metal halide perovskites due to elemental similarity.[5, 6] In TlX, Tl^+ ([Xe] 4f14 5d10 6s2 6p0) is isoelectronic similar to Pb^{2+} ([Xe] 6s2 4f14 5d10 6p0) with lone-pair electrons in outermost s-orbital. Antibonding interaction of filled 6s orbital with halide 4p/5p orbital makes valence band maximum (VBM). 6p orbital of Tl^+ is largely making conduction band minimum (CBM). Strong spin-orbit coupling in 6p provides further stabilization to conduction band minimum (CBM). Thus 6s electrons and spin-orbit coupling in 6p produces electronic band structure, which is supposed to have extremely low deep-level trap states. Such an electronic band structure is the one of the proposed origins of defect-tolerance in perovskite semiconductors as shown in Figure 1b.[6] Therefore, compositional similarity with metal halide perovskites, thallium halide is expected to have a similar defect-tolerant band structure.

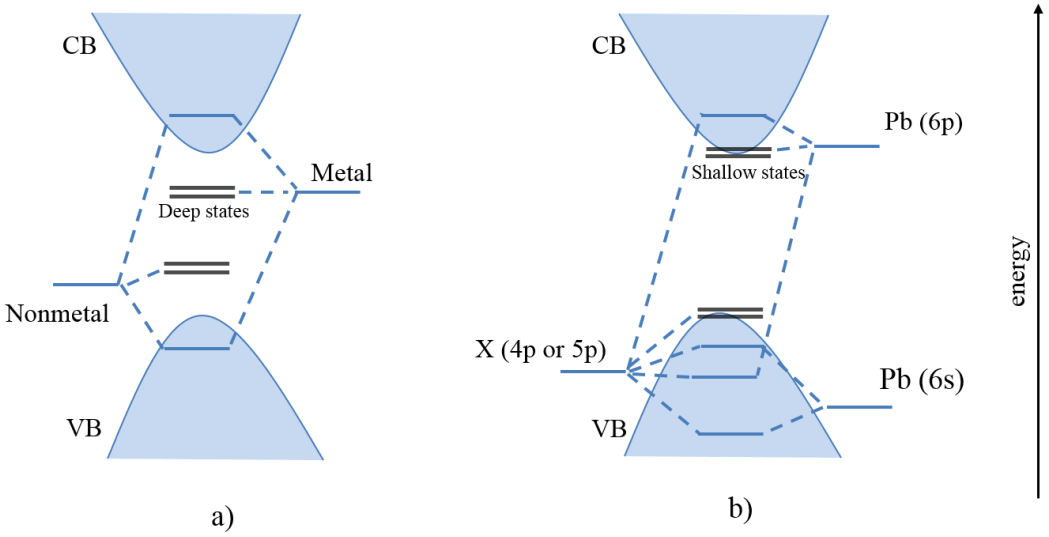

***Figure 1**. Schematic of electronic band structure of semiconductors: a) Defect-intolerant (inorganic semiconductors such as GaAs, CdSe etc.) and b) Defect-tolerant (metal halide perovskites, ABX_3 where, $A=Cs^+$, $B=Pb^{2+}$, $X=I^-$, Br^-). Major difference can be found in position of defect states in two cases a and b.*

Another important issue with wide bandgap and many inorganic semiconductors is that the possibility of presence of deep level defect states within bandgap (Figure 1a).[7] Since thallium halides have band gap in UV region[8] and band structure similar to metal halide perovskites (Figure 1b), the possibility of defect-tolerant nature of band structure and its effect on carrier transport are the important points to be researched. Thallium halides are one of the important classes of semiconductors due to their potential application in high-energy radiation and particle detectors in recent times.[9-11] Photoconductor applications are solely dependent on the excited states of semiconductors.

In this chapter, we have conducted a time-resolved THz spectroscopic study on thin films of Thallium halide (TlBr and TlI) NCs and their bulk form. According to our study, TlBr and TlI NCs films have shown long diffusion lengths and high mobility. TlBr and TlI exhibit different carrier recombination dynamics. Further, we have also investigated bulk thallium halides (TlBr and TlI) using time-resolved THz spectroscopy to understand better how morphology impacts charge carrier dynamics. We will therefore attempt to compare the results from the bulk and NCs films samples.

3.2 Experimental Section

3.2.1 TlX NCs synthesis, film preparation and characterisation

Synthesis of TlX NCs

The hot-injection method was used to synthesise TlBr and TlI NCs.[8] Synthesis and characterisation of NCs were done by Wasim Mir from Dr. Angshuman Nag's group at IISER Pune. For THz spectroscopy studies, TlX NCs thin film was made by drop-casting colloidal NCs dispersion in hexane onto the non-conducting polystyrene substrate. Details of the synthesis and characterisation of NCs can also be found in reference elsewhere.[8]

In a three-neck round bottom flask, 0.5 mmol of Thallium (I) nitrate ($TlNO_3$) was taken with 15 ml 1-octadecene, 1 ml oleic acid and 1 ml oleylamine. This reaction mixture was degassed at 100 ^oC for 1 hour, and then the temperature was raised to 300 ^oC under N_2 atmosphere till the solution became clear. In another round bottom flask, 1 mmol of tetra butyl ammonium iodide (TBAI) was taken with 5 mL 1-octadecene and 5 ml oleylamine. The mixture was degassed for 90 minutes at 140 ^oC, and then the temperature was raised to 200 ^oC under N_2 atmosphere till the solution became clear. This clear iodide solution was swiftly injected into the thallium solution kept at 170 ^oC, and the reaction was quenched immediately after the addition using an ice bath to obtain 8.4 nm TlI NCs. After centrifuging the reaction product at 3000 rpm for 1 min, the precipitate obtained was discarded, and the supernatant was taken up for further washing. The NCs from the supernatant solution were precipitated by adding a small amount of tert-butanol as an anti-solvent. The obtained NCs were dispersed in hexane and kept in the refrigerator for 30 minutes.

TlBr NCs were synthesized using the same procedure with a few changes involving 1 mmol $TlNO_3$ and 2 mmol of tert butyl ammonium bromide, and the final reaction was carried out at 300 ^oC.

Characterization

Powder X-ray diffraction (PXRD) of drop cast films of TlX NCs was carried out by Bruker D8 Advance X-ray diffractometer with Cu K_α (1.54 Å) radiation. An orthorhombic phase of

TlI NCs and a cubic phase of TlBr NCs were confirmed from the PXRD pattern at room temperature as shown in Figures 2a and 2b.

TEM images were collected using a JEOL JEM-2100F electron microscope with a 200 kV electron source. The average diameter of TlI NCs and TlBr NCs obtained from TEM images are 8.4 ±1.2 nm and 28.7 ± 3.2 nm respectively, as shown in Figures 2c and 2d.

The UV-Visible absorption spectrum of TlX NCs in hexane was collected using Perkin Elmer Lambda-45 UV/vis spectrometer, as shown in Figures 2e and 2f (red). UV-visible absorption spectrum shows the excitonic absorption peak around 438 nm for TlI NCs and around 400 nm for TlBr NCs. According to previous reports, the average diameter of TlI NCs (8.4 nm) and average diameter of TlBr NCs (28.7 nm) are more than their excitonic Bohr excitonic diameter (~8.8 nm for TlI and ~9.7 to 24.6 nm for TlBr).[12-18] Hence colloidal NCs are in a weak quantum confinement region or no confinement region.

Photoluminescence (PL) spectra of TlI and TlBr NCs were recorded using Edinburg FLS980 spectrophotometer, as shown in Figures 2e and 2f (blue). The peak of PL spectrum centred is at 480 nm as measured for TlI NCs of diameter 8.4 nm with PLQY of about 6% obtained for TlI NCs. The peak of the PL spectrum shows peak at 435 nm for TlBr NCs of diameter 28.7 nm with PLQY of about 10%. Both the NCs dispersed in hexane were illuminated with a wavelength of 365 nm. Photoluminescence quantum yield (PLQY) of TlI and TlBr NCs were obtained with the help of sodium salt of fluorescein dye in water used as a reference (PLQY = 0.92 in water)

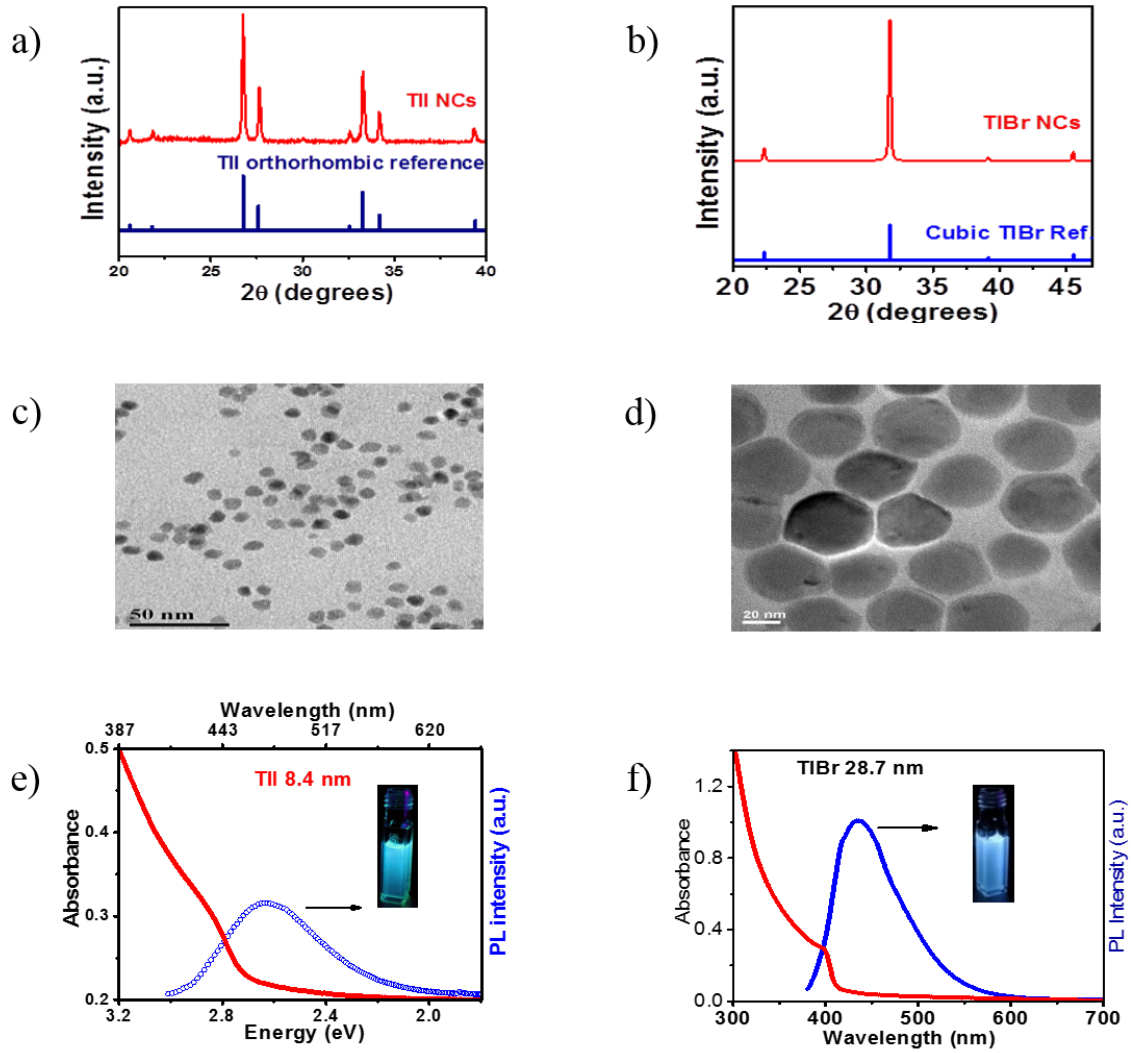

Figure 2. *a-b) PXRD of TlI and TlBr NCs c-d) TEM Images of TlI (on 50 nm scale) and TlBr NCs (on 20 nm scale) and e-f) UV-visible absorbance (red) and PL spectrum (blue) of TlI and TlBr NCs. Reproduced from ref.* [8] *with permission from the Royal Society of Chemistry.*

TlX NCs film characterization

TlX NCs films were made by drop-casting colloidal NCs dispersion in hexane onto the non-conducting polystyrene substrate.

The UV-Visible absorption spectrum of TlX NCs films (Figures 3b and 3d) was collected using Perkin Elmer Lambda-45 UV/vis spectrometer. Polystyrene, a non-conducting substrate, was used as a reference while measuring the absorption spectrum of thallium halide NCs films. UV-visible absorption spectrum shows the excitonic absorption peak around 438

nm for TlI NCs film and around 400 nm for TlBr NCs film. TlX NCs films show a bandgap similar to colloidal NCs, and observed excitonic peaks of TlX NCs films are very close to the bulk bandgap values of respective semiconductors, showing that NCs are in a very weak quantum confinement region or no confinement region.

The thickness of TlXs films was measured using an optical surface profilometer, ZETA instrument. Thicknesses measured for TlBr NCs film (Figure 3c) and TlI NCs films (Figure 3d) were 11±0.9 μm and 8±0.7 μm, respectively.

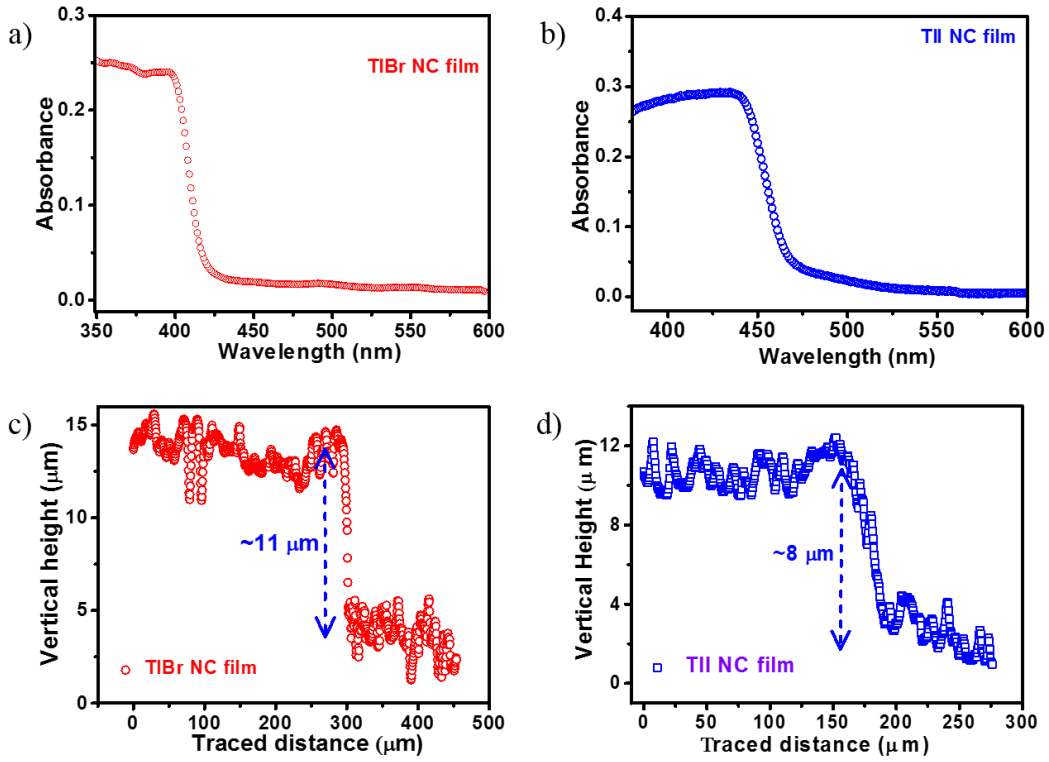

Figure 3. *Absorbance of a) TlBr NCs b) TlI NCs films and, film thickness of c) TlBr NCs d) TlI NCs. Reproduced from ref.* [8] *with permission from the Royal Society of Chemistry.*

For TRTS measurement of TlX NCs film, the radii of pump and probe beams at the sample were 1.6 mm and 0.4 mm as measured by the knife-edge method.

3.2.2 Bulk TlX (X=Br, I) synthesis, thin film preparation and characterisation

Bulk TlX Synthesis

Bulk TlBr was prepared via ionic metathesis reaction by Wasim Mir from Dr. Angshuman Nag's group at IISER, Pune. The reaction was performed at room temperature (24 ^{o}C) and under ambient conditions. Thallium nitrate ($TlNO_3$) 0.5 mmol, 124.5 mg was dissolved in 5 mL dimethylformamide (DMF). In a separate vial, potassium bromide (KBr) 0.5 mmol, 59.5 mg was dissolved in 1 mL DMF. The KBr solution was then slowly added to $TlNO_3$ solution under vigorous stirring leading to the formation of yellowish precipitate. The product was separated by centrifugation at 5000 rpm, and the precipitate was washed three times with methanol. Once the powder sample of TlBr was made, we ground the powder for several hours to make the particle size smaller and uniform. Next, isopropyl alcohol was added to the TlBr powder to make TlBr paste. Several films were made on non-conducting high-density polyethylene (HDPE) substrate using doctor blade method.[20]
Bulk TlI film was made from a powder sample of TlI purchased from Sigma-Aldrich. The thin film of bulk TlI was prepared in the same manner by coating IPA solution (paste) of TlI on HDPE substrate using doctor blade procedure.
For THz studies, the appropriate film was selected by measuring film thickness.

Characterization

Powder X-ray diffraction of bulk TlX film samples were carried out by Bruker D8 Advance X-ray diffractometer with Cu K_α (1.54 Å) radiation. A cubic phase of TlBr and an orthorhombic phase of TlI were confirmed from the PXRD pattern at room temperature (Figures 4a and 4b).[8]

UV-visible absorption spectra of both bulk TlBr, TlI films were recorded using a Shimadzu UV 3600 plus spectrophotometer in reflection mode. Barium sulphate ($BaSO_4$) was used as a reference. Here we recorded diffuse reflectance, R, from the sample and reference. Diffuse reflectance, R, was used to obtain the Kubelka-Munk Function, $F(R) = \frac{\alpha}{s} = \frac{(1-R)^2}{2R}$ here, $R =$

$\frac{R_{Sample}}{R_{Ref-BaSO4}}$. Bandgaps of bulk TlX were obtained with UV-visible absorption spectra and Tauc plot. Bandgaps of bulk TlBr and bulk TlI are 2.97 eV and 2.73 eV, respectively (Figures 4c and 4d).

The thickness of TlXs films was measured using an optical surface profilometer from ZETA instruments. Thicknesses obtained for TlBr NCs film and TlI Ncs film were 67.8 ± 4.9 μm and 26.4 ± 2.7 μm (Figures 5a and 5b), respectively.

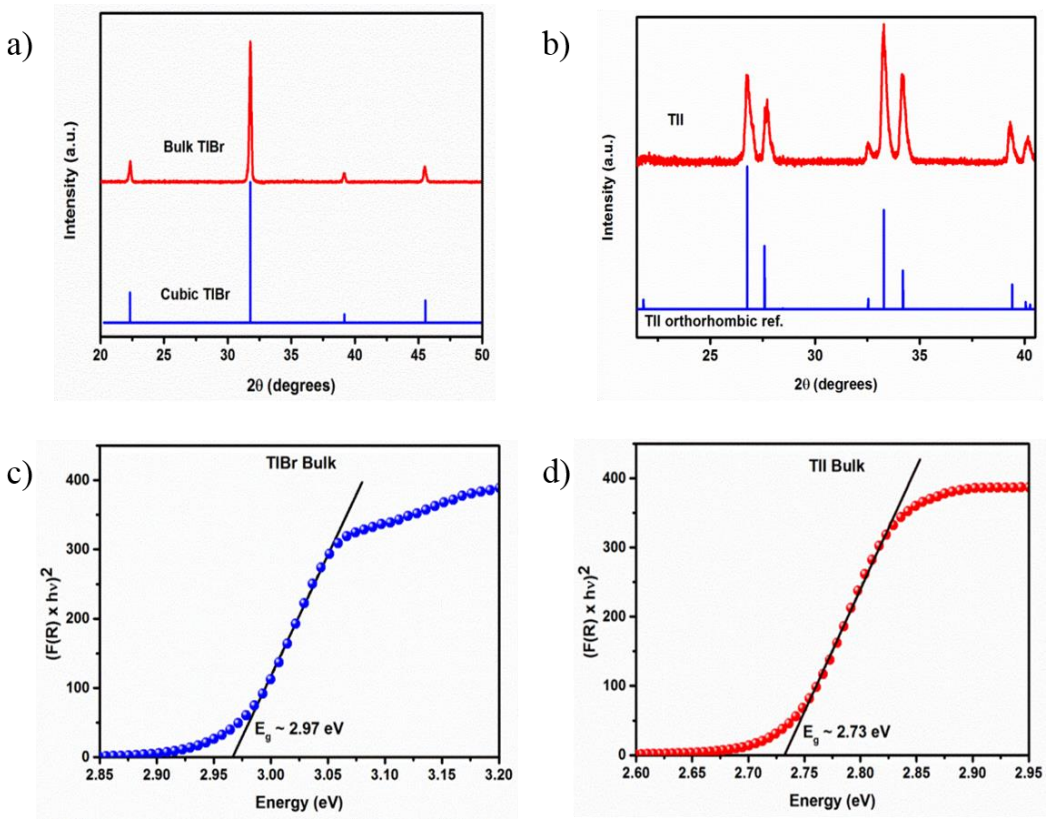

Figure 4. *PXRD of bulk TlX: a) TlBr b) TlI. Diffuse reflectance spectra and Tauc plot show bandgap of bulk TlX: c) bulk TlBr and d) bulk TlI.*

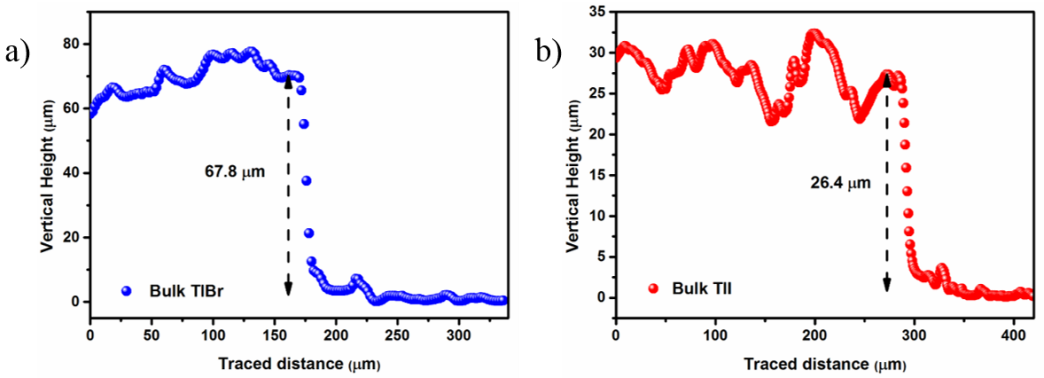

Figure 5. *The film thickness of a) Bulk TlBr and b) Bulk TlI.*

For TRTS measurement of bulk TlX film, the average diameters of pump and probe beams at the sample were 1.4 mm and 0.8 mm, measured by the knife-edge method.

3.2.3 THz-TDS and TRTS experiment

Experimental setup, data acquisition, and data analysis procedures for THz-TDS and TRTS experiments of thin film are discussed in detail in Chapter 2.

3.3 Results and Discussions

3.3.1 Charge carrier dynamics in Thallium halide NCs films

a) Frequency-averaged scans (pump scans)

We studied charge carrier dynamics of TlBr and TlI NCs films using the TRTS technique in transmission geometry. TlX films were photoexcited using a wavelength of 400 nm. For the TRTS experiment, TlBr and TlI NCs solution were drop-casted on non-conducting polystyrene substrates. Thicknesses for TlBr and TlI were found to be around 11±0.9 μm and around 8±0.7 μm, respectively. A pump wavelength of 400 nm creates photoexcited charges just above the bandgap with very low extra energy.

In the first part of the TRTS experiment, which is simply frequency-averaged scans or pump scans, the gate beam delay is fixed at a position such that the maximum of the THz (electric field) waveform is detected. The maximum of THz electric field is monitored with respect to

pump-probe delay of up to 1500 ps in the absence of the pump wavelength and in the presence of the pump wavelength. We use two computer-controlled mechanical stages to manipulate the gate delay and the pump-probe delay (see Chapter 2 for details). In frequency-avaraged TRTS, photoinduced change in the transmission of the maximum (peak) of THz field is measured as a function of pump-probe delay time (t_p),

$$\Delta T(t_p) = T_{on} - T_{off} \quad (1)$$

Here T_{on} is the transmitted THz field through the photoexcited sample (pump-on), which changes with pump-probe delay and T_{off} is the transmission of the THz field through the non-excited sample, which remains constant over the delay. ΔT is measured by collecting change in THz electric field.

$$\Delta E(t_p) = E_{on} - E_{off} \quad (2)$$

Here E_{on} and E_{off} are THz electric fields transmitted through the photoexcited and unexcited samples respectively. TlX samples were photoexcited for different fluences (photons energy per unit area) at room temperature. In TlBr NCs film, fluences were used from 7 to 24 μJ/cm^2; in TlI NCs film fluences were used from 5 to 23 μJ/cm^2. Photon density (N_{Ph}) was calculated from experimentally measured fluence (F_l) using the following relation,

$$N_{Ph} = \frac{F_l(1 - 10^{-OD_\lambda})}{\delta\, h\nu} \quad (3)$$

Here $\delta(=\frac{OD_\lambda\, ln(2)}{d})$ is the penetration depth, $h\nu$ is photon density and OD_λ is the optical density at the pump excitation wavelength (400 nm). Since thallium halides have excitonic binding energy (~6.5 meV[13, 21] for TlBr and ~17 meV[22, 23] for TlI) below room temperature kinetic energy (25 meV), it is assumed that one photon creates two photoexcited charge carriers, one electron and a hole.[13] Total carrier density (N_0) was calculated from equation 4.

$$N_0 = \varphi\ 2\ N_{Ph} \quad (4)$$

Here, φ is the photon-to-charge carrier ratio. In this experiment N_{Ph} varies from 0.85 × 10^{15} to 3.05 × 10^{15} cm^{-3} for TlBr NCs film and 0.9× 10^{15} to 4.25 × 10^{15} cm^{-3} for TlI NCs film. Differential transmission $\left(\frac{\Delta T}{T_{off}}\right)$ can be converted to photoconductivity ($\Delta\sigma$) using thin film

approximation when the thickness of the film is less than the wavelength of THz frequency range (1THz ≡ 300 μm). According to the thin film approximation, photoconductivity is given by equation 5.[24, 25]

$$\Delta\sigma\,(t_p) = \frac{1}{z_0 d}(n_a + n_b)\frac{-\Delta T(t_p)}{T_{off}} \qquad (5)$$

Here z_0 $(1/\varepsilon_0 c)$ is free space impedance and equals 377 Ω. d is the film thickness. n_a and n_b are refractive indices on either side of the photoexcited film. We use photoconductivity to find initial, peak carrier mobility and diffusion length, which will be discussed further.

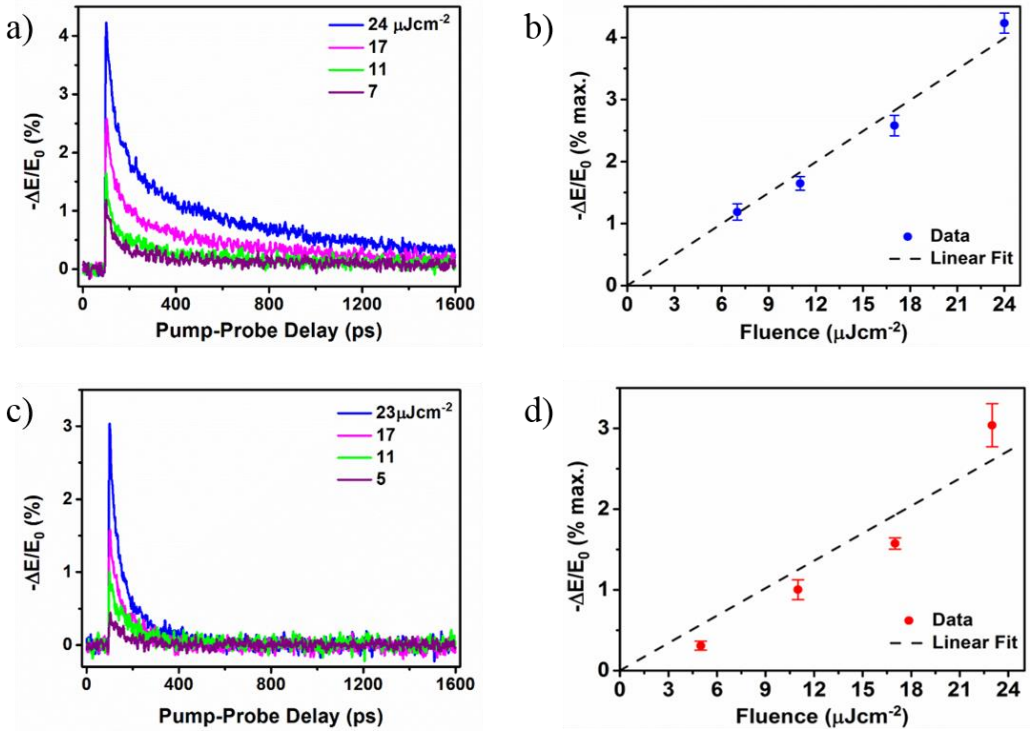

Figure 6. *Fluence-dependent THz transients a) TlBr NCs film and c) TlI NCs film. Maximum of negative differential transmission versus fluence and their linear fits for b) TlBr NCs film (adj. R^2~0.99) and d) TlI NCs film (adj. R^2~0.95). Reproduced from ref. [8] with permission from the Royal Society of Chemistry.*

Figures 6a and 6c show the charge carrier dynamics of TlBr and TlI NCs films as a function of pump-probe delay. The maximum negative differential transmission increases when fluence increases due to an increase in the photoinduced absorption. Figures 6b and 6d show

the linear relation between maximum differential transmission and excitation fluence of TlX NCs films.

To understand charge carrier dynamics of TlX NCs films, THz transients were fitted using a multiexponential function convoluted with a Gaussian function. First, each THz transient was normalised to its peak value. The following relation has been utilised to fit THz transients (see Chapter 2 for details about equation 6).[26]

$$y = G(t - t_0) \otimes \sum_i a_i exp\,[-(t - t_0)/t_i\,] \qquad (6)$$

We obtained time constants t_i for every fitted THz transient. For TlBr NCs film, we required three exponentials; for TlI NCs film, we needed two exponentials for a good fit. The first difference in carrier dynamics of Thallium halides can be found in their dependence on fluence. Figure 7 shows that TlBr NCs film's carrier dynamics is fluence-dependent, and that of TlI NCs film is fluence-independent at experimental condition (i.e. fluence/photon density used in the present experiment). Carrier dynamics seem to slow down with fluence increasing for TlBr NCs film.

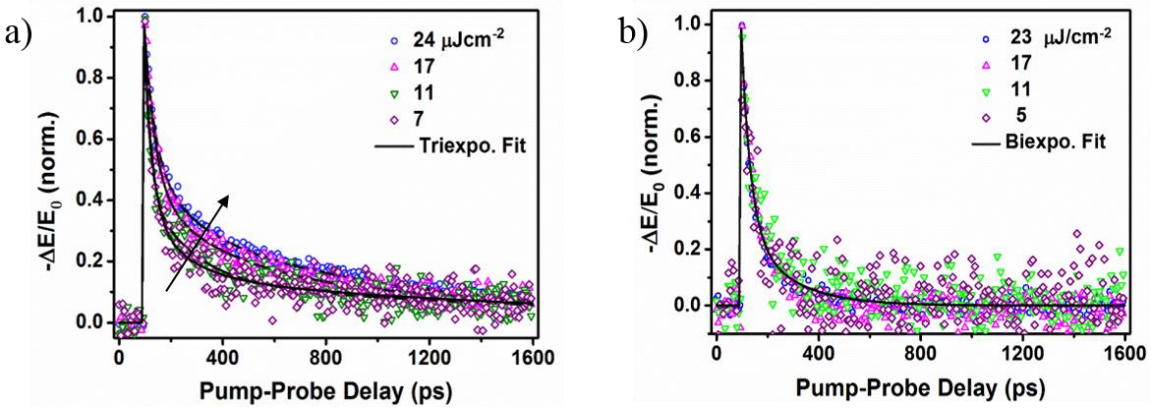

Figure 7. *Normalised THz transients of a) TlBr NCs film and b) TlI NCs film and their multiexponential fits. Reproduced from Ref.* [8] *with permission from the Royal Society of Chemistry.*

Three time constants were obtained for TlBr NCs film and are plotted against total carrier density, as shown in Figure 8. The fastest time constant is almost fluence independent, whereas intermediate time constants increase with the fluence from 155 ps to 240 ps. The slowest time components change from 1650 to 1270 ps with fluence increment. Average lifetimes $< t >$ were obtained for each THz transient using the following equations.[27]

$$< t >= \sum f_i \, t_i \tag{7}$$

$$f_i = a_i t_i / \sum a_i \, t_i \tag{8}$$

The average lifetime decreases from 1300 to 800 ps on increasing fluence.

Now let us discuss the possible processes involved in the photoexcitation dynamics of TlBr NCs. Since the smallest component does not vary with fluence, this process is assigned to trap states filling. Intermediate time components are interesting as these time components slow down with fluence and could be due to the trap saturation process.[28, 29] A similar trend in relaxation time with an increase in power (in the same order of time component) was found in undoped semi-insulating GaAs, possibly due to trap-saturation as free electrons density being larger than surface trap density.[30] The slowest time component could be assigned to the bimolecular recombination process.[31]

The charge carrier dynamics of TlI NCs film show fluence independent behaviour and is much faster than the TlBr NCs film. Two time constants were obtained by fitting THz transients except for the lowest fluence-dependent THz transient. The fast time component is independent of fluence and could be assigned to the trap-filling process. The slow time component is also independent of fluence and could be another trap-filling process or a weakly active bimolecular process. The fast and the slow time components are around 20 ps and 100 ps, respectively. Tables 1 and 2 show time constants obtained from fitting THz transients of TlBr NCs and TlI NCs films, respectively.

Table 1. *Fitting Parameters for THz transients of TlBr NCs film under photoexcitation of 400 nm wavelength. (Errors are given in parentheses.)*

Fluence ($\mu J/cm^2$)	t_1(ps)	a_1	t_2 (ps)	a_2	t_3(ps)	a_3	$< t >$ (ps)
24	44.5 (0.2)	0.481 (0.003)	240.0 (2.0)	0.223 (0.004)	1133 (11.0)	0.282 (0.002)	953.0 (8.4)
17	40.5 (0.2)	0.523 (0.002)	227.0 (3.0)	0.251 (0.001)	1269 (13.0)	0.208 (0.002)	1020.0 (11.8)
11	22.0 (0.2)	0.534 (0.002)	172.0 (2.0)	0.313 (0.001)	1664 (23.0)	0.132 (0.001)	1315.0 (20.9)

7	31.8 (0.3)	0.586 (0.004)	155.8 (3.4)	0.212 (0.003)	1655 (24.0)	0.148 (0.001)	1386.0 (17.6)

Table 2. *Fitting Parameters for THz transient of TlI NCs film under photoexcitation of 400 nm wavelength. (Errors are given in parentheses.)*

Fluence ($\mu J/cm^2$)	t_1(ps)	a_1	t_2 (ps)	a_2	$< t >$ (ps)
23	35.4 (0.1)	0.679 (0.002)	146.7 (0.7)	0.303 (0.002)	107.6 (0.625)
17	24.8 (0.4)	0.371 (0.004)	93.9 (0.4)	0.643 (0.005)	84.8 (0.4)
11	22.0 (0.5)	0.443 (0.003)	136.9 (0.5)	0.536 (0.002)	123.4 (0.5)
5	71.4 (0.2)	0.831 (0.002)			71.4 (0.2)

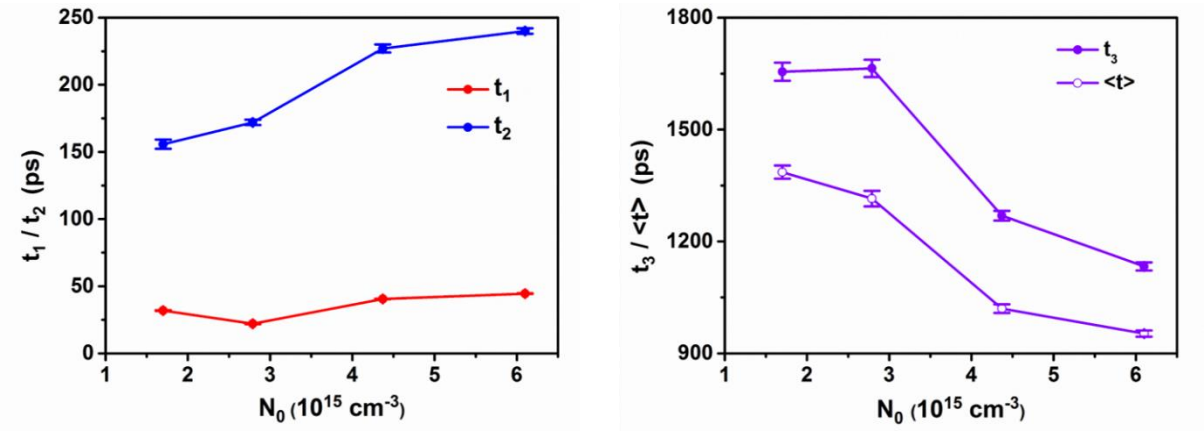

Figure 8. *Time constants of TlBr NCs films obtained by the fitting multi-exponential function (with their respective error): a) fastest time (t_1) and intermediate time constants (t_2) b) Slowest time constant (t_3) and average time constants ($< t >$).*

b) Mobility and diffusion length

One of the main advantages of the TRTS technique is obtaining carrier transport parameters such as mobility and diffusion length in a non-contact fashion. This could be advantageous in very small particles where measuring physical constants for electronic and transport properties is either difficult or impossible. Here we have measured the mobility and diffusion length of TlBr and TlI NCs film for the experimental fluence range. Effective mobility ($\phi\mu$)

and diffusion length (L_D) at the peak photoconductivity ($\Delta\sigma$) are calculated from equations 9 and 10.

$$\phi\mu = \frac{\Delta\sigma}{qN_0} \tag{9}$$

$$L_D = \sqrt{\frac{< t > \mu k_B T}{q}} \tag{10}$$

Here peak photoconductivity is calculated by using equation 5 (in which the peak value of negative differential transmission $\left(\frac{-\Delta T}{T_{off}}\right)$ considered). We determine the effective mobility from frequency-averaged TRTS scans and which will provide a lower bound to mobility. In the present study, the TlBr NCs film has a diffusion length of about 0.8 µm and charge carrier mobility of around 250 cm^2/Vs. Figure 9 displays effective mobility and diffusion length as a function of carrier density. TlI NCs film has lesser mobility than TlBr NCs films.

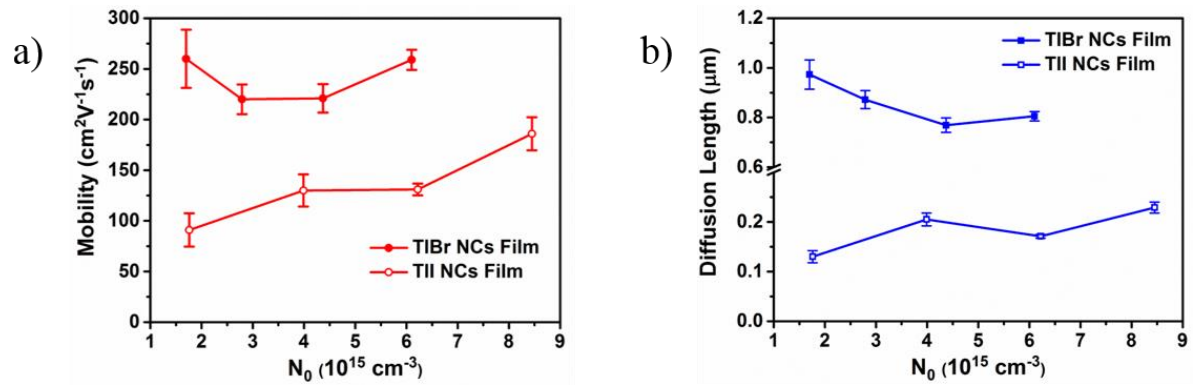

Figure 9. *a) Mobility and b) Diffusion length (break on y-axis from 0.3 to 0.6 µm) of TlX NCs film. Reproduced from ref.* [8] *with permission from the Royal Society of Chemistry.*

Table 3. *Parameters extracted from pump scans at different pump fluences at 400 nm pump wavelength. (Peak conductivity= $\Delta\sigma_{peak}$) (Errors are given in parentheses.)*

Fluence (µJ cm^{-2})	Photons (10^{13} cm^{-2} per pulse)	N_0 (10^{15} cm^{-3})	$\frac{-\Delta E}{E_0}$ $(max.)$	$\Delta\sigma_{peak}$ (Sm^{-1})	Mobility ($cm^2V^{-1}s^{-1}$)	Avg. lifetime (ps)	Diffusion length (µm)
	TlBr NCs						
24	4.76	6.10	0.042 (0.002)	25.3 (1.0)	259 (9.9)	953.0 (8.4)	0.805 (0.019)

17	3.41	4.37	0.026 (0.002)	15.4 (1.0)	221 (14.1)	1020.0 (11.8)	0.769 (0.029)
11	2.18	2.79	0.017 (0.001)	9.9 (0.7)	220 (14.6)	1315.0 (20.9)	0.872 (0.036)
7	1.33	1.70	0.012 (0.001)	7.1 (0.8)	260 (28.7)	1386.0 (17.6)	0.973 (0.059)
	TlI NCs						
23	4.64	8.45	0.030 (0.003)	25.1 (2.2)	186 (16.3)	107.6 (0.625)	0.229 (0.011)
17	3.42	6.22	0.016 (0.001)	13.0 (0.6)	131 (5.79)	84.8 (0.4)	0.171 (0.004)
11	2.19	3.99	0.010 (0.001)	8.3 (1.0)	130 (15.9)	123.4 (0.5)	0.205 (0.013)
5	0.97	1.76	0.003 (0.0005)	2.6 (0.5)	91 (16.3)	71.4 (0.2)	0.130 (0.012)

c) Frequency-resolved scans (probe scans)

Frequency-resolved THz study can reveal the nature of the photoexcited charge carriers, photoinduced phonons, carrier-phonon coupling, etc.[32] In frequency-resolved THz study, time-domain signals of the photoinduced change in THz electric field (ΔE) and steady-state electric field (E_{off}) are collected at various pump-probe delay (t_p). Time-domain signals are Fourier transformed using thin film approximation to obtain frequency-domain complex photoconductivity spectrum (Figures 10a and 10b).

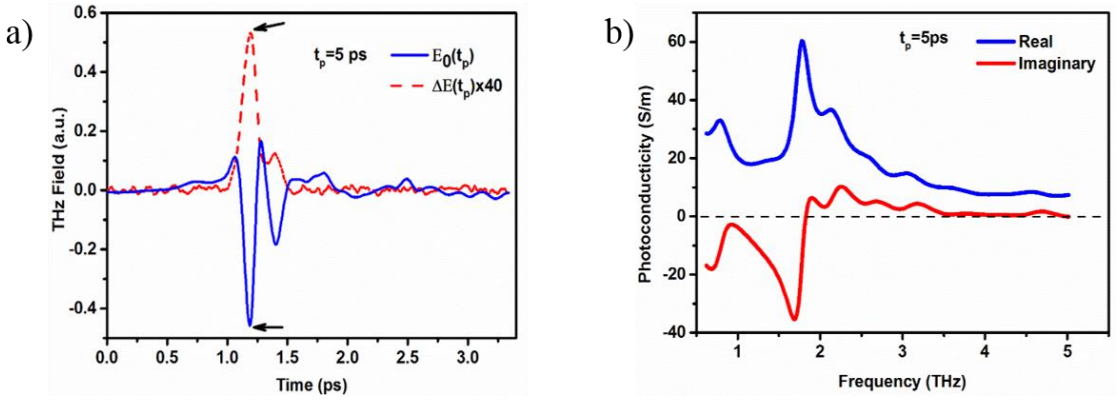

Figure 10. *a) Photoinduced change in THz electric field (red) and unexcited electric field (blue) and b) Real and imaginary parts of photoconductivity at the pump-probe delay of 5 ps. Reproduced from ref.* [8] *with permission from the Royal Society of Chemistry.*

Photoconductivity spectra were collected for three different fluences, 7 μJ/cm^2, 17 μJ/cm^2 and 24 μJ/cm^2 under 400 nm photoexcitation for TlBr NCs film for various pump-probe delays as shown in Figure 11. As clearly seen in Figure 10b, the real part of photoconductivity is positive, and the imaginary part of the photoconductivity (at a delay of 5 ps) is negative in the low frequency range and positive in the high-frequency range. Real photoconductivity is positive with broad peaks, and imaginary conductivity is negative and positive in magnitude with several inflection points where peaks occurred in the real part of photoconductivity. This kind of complex conductivity spectra implies the presence of the free carriers with backscattering (i.e. charge carrier localization with nanoparticles), and the presence of absorption peaks is most likely due to phonon modes. Complex photoconductivity spectra at several pump-probe delays were fitted to the Drude-Smith and Lorentz oscillator models. We combine both models in the following expression (equation 11).

$$\tilde{\sigma}(\omega) = \frac{\sigma_{dc}}{(1 - i\omega\tau)} + \frac{\sigma_{dc}\, c}{(1 - i\omega\tau)^2} + \sum_i \frac{\sigma_i \omega}{(\omega - i\tau_i(\omega^2 - \omega_i^2)} \qquad (11)$$

The first two terms of the right side of equation 11 represent Drude-Smith conductivity, and the last term describes resonance in the photoconductivity in the form of the Lorentz oscillator. [33] Here, τ is the scattering time of photocarriers, c is the constant related to carrier localisation. c varies from 0 (no localisation or pure Drude-type (free carriers) response) to -1 (maximum localisation). ω_i represents the frequency of i^{th} oscillator and τ_i is in the unit of time and it is the related to width of i^{th} oscillator and oscillator strength by equation 14 .

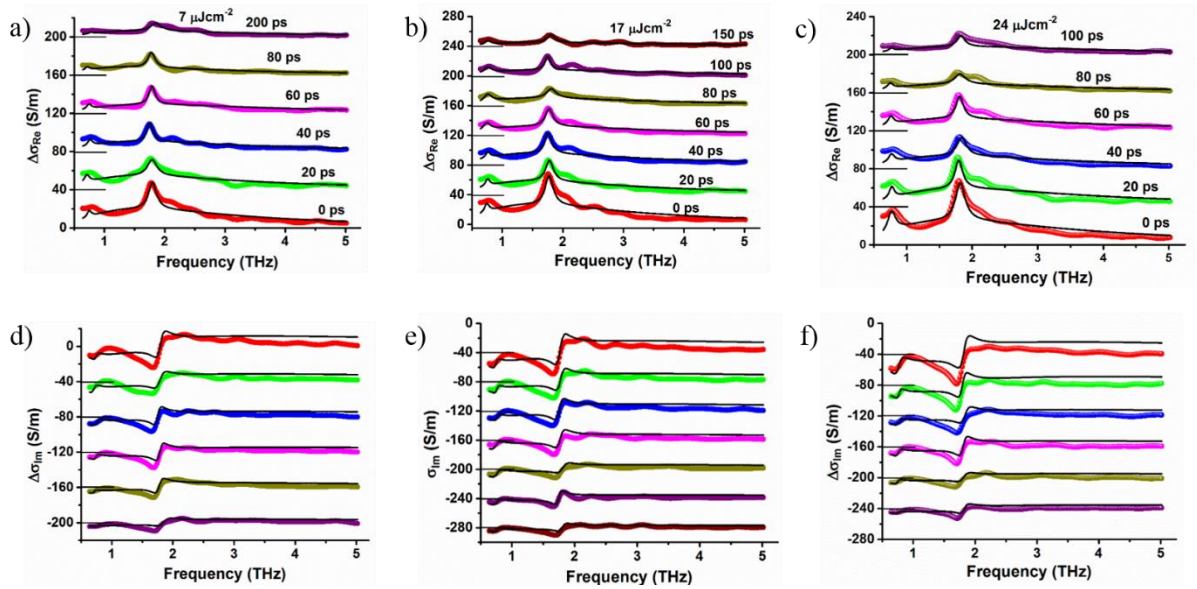

Figure 11. *Photoconductivity spectra at various delays with Drude-Smith and Lorentz oscillator model fitting for a-c) Real parts of complex photoconductivity d-f) Imaginary parts of complex photoconductivity for TlBr NC film under 400 nm photoexcitation at fluences of 7 μJ/cm^2 (a & d), 17 μJ/cm^2 (b & e), and 24 μJ/cm^2 (c & f).*

d) THz time-domain spectroscopy of TlBr NCs film

We have performed THz time-domain spectroscopy (THz-TDS) on TlBr NCs films on a polystyrene substrate. Refractive index and absorption coefficient were obtained for the thin film on the substrate, as discussed in Chapter 2. Figure 12a shows time-domain THz waveforms (signals) transmitted through the reference (polystyrene substrate) and TlBr NCs film. These time-domain waveforms are Fourier transforms using Duvillaret's algorithm to obtain the complex refractive index of TlX NCs film.[34]

The absorption coefficient shows a broad peak around 2 THz, as seen in Figure 12b. Few theoretical and experimental studies were available on lattice vibrations of thallium halides such as TlBr, TlCl, and TlI. Several modes have been observed around 2 THz in the inelastic neutron scattering experiment.[35-37] A broad peak near 2 THz in our steady-state THz measurement could be TO phonon mode. A prominent peak around 1.8 THz in the transient photoconductivity spectra (Figure 11) is closely related to the peak observed near 2 THz in the steady-state absorption spectrum obtained using THz-TDS Figure 12b).

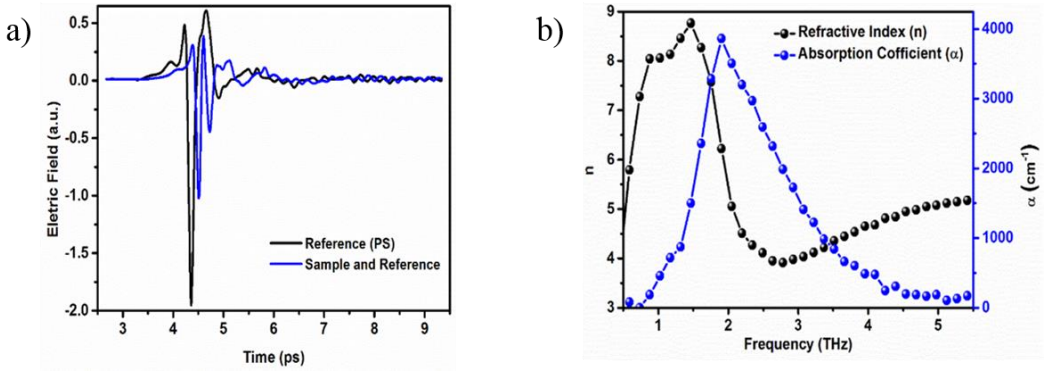

Figure 12. *a) Time-domain THz signals transmitted through the reference and TlBr NCs film. b) Refractive index and absorption coefficient vs TH frequency of TlBr NCs film.*

e) Parameters obtained from frequency-resolved THz study

TRTS offers to measure some crucial semiconductor parameters in a non-contact fashion by modelling complex photoconductivity spectra at different delays. Drude-Smith Scattering time (τ), Drude conductivity (σ_{dc}), carrier density $n(t_p)$, mobility $\mu(t_p)$, plasma frequency (ω_p) and oscillator strength (f_i) for i^{th} oscillator are obtained by fitting experimental photoconductivity spectra at the specific delay (t_p).

$$n(t_p) = \frac{\sigma_{dc} m}{e^2 \tau} \tag{12}$$

$$\mu(t_p) = \frac{e\tau}{m_{ave}} \tag{13}$$

$$f_i = \frac{\sigma_i}{\tau_i} \tag{14}$$

$$\omega_p = \sqrt{\frac{\sigma_{dc}}{\varepsilon_0 \tau}} \tag{15}$$

Here σ_i and τ_i are in units of conductivity and time, which are used to obtain the i^{th} Lorentz oscillator strength at a resonance angular frequency ω_i. ε_0 is the permittivity of free space (8.85×10^{-12} F.m^{-1}). $m_{ave}$is the average mass of an electron and a hole. Average mass is

calculated from $m_{ave} = \frac{m_e^* + m_h^*}{2}$ where m_e^* $(= 0.28m_0)$ and $m_h^* (= 0.72m_0)$ are effective masses of electron and hole, with m_0 (=9.1 × 10^{-31} kg) is the mass of electron.[8]

The scattering time (τ) of photocarriers is a fundamental parameter of semiconductors. This study obtains τ using TRTS with an average value of ~100 fs, as shown in Figure 13a; it remains almost the same for all the fluence and different delays (up to 200 ps as shown in Figure 13). Scattering time of about 100 fs is observed in many inorganic semiconductors, studied by THz spectroscopic techniques.[38, 39] Carrier density is found to decrease with increasing delay, and it is evident that carriers start recombining after photoexcitation, and their density is supposed to reduce with increased pump-probe delays.

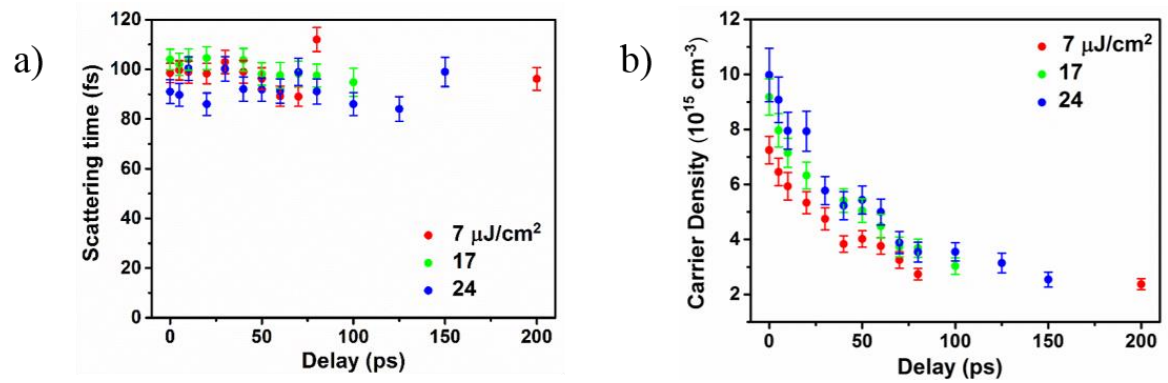

Figure 13. *a) Scattering time and b) Carrier density (with their error) obtained from fitting the frequency-resolved THz scans to Drude-Smith and Lorentz model (equation 11).*

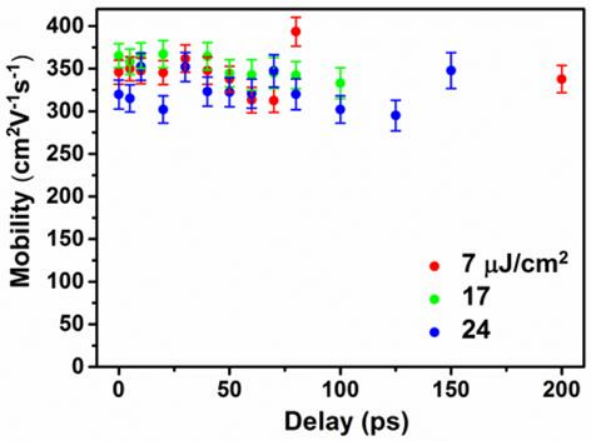

Figure 14. *Mobility (with their error) obtained from fitting the frequency-resolved THz scans to Drude-Smith and Lorentz oscillator models (equation 11).*

Interestingly, carrier mobility is found to be very high value (>350 cm^2/Vs) and does not change with the pump-probe delay of at least up to 200 ps. There is slight variation in mobility value for different fluences, as shown in Figure 14. Tables 4 to 9 show various parameters (related to Drude-Smith and Lorentz oscillators models) obtained from fitting complex photoconductivity with equation 11. These transport and other parameters can be utilised in applications dealing with photoexcited properties.

Table 4. *Parameters (Drude-Smith) obtained by fitting Drude-Smith and Lorentz model for 7 μJ/cm^2. (Errors are given in parentheses.)*

t_p (ps)	c	σ_{dc} (S/m)	τ (fs)	ω_p (THz)	$n(t_p)$ (10^{15} cm^{-3})	$\mu(t_p)$ (cm^2/Vs)
0	-1 (0.04)	40.1 (1.3)	98.5 (3.9)	6.8 (0.2)	7.2 (0.5)	346 (14)
5	-1 (0.05)	36.2 (1.2)	99.6 (3.9)	6.4 (0.2)	6.5 (0.5)	350 (14)
10	-1 (0.05)	33.0 (1.2)	98.9 (4.4)	6.1 (0.2)	5.9 (0.5)	347 (15)
20	-1 (0.06)	29.5 (1.0)	98.3 (4.1)	5.8 (0.2)	5.3 (0.4)	345 (14)
30	-1 (0.06)	27.5 (0.9)	103.0 (4.7)	5.5 (0.2)	4.7 (0.4)	362 (16)
40	-1 (0.05)	21.3 (0.8)	99.0 (4.5)	4.9 (0.2)	3.8 (0.3)	348 (16)
50	-1 (0.06)	21.7 (0.7)	96.2 (4.4)	5.1 (0.2)	4.0 (0.3)	338 (15)
60	-1 (0.05)	18.9 (0.6)	89.2 (4.1)	4.9 (0.2)	3.8 (0.3)	313 (15)
70	-1 (0.05)	16.3 (0.5)	89.0 (3.9)	4.5 (0.2)	3.3 (0.3)	313 (14)
80	-1 (0.05)	17.2 (0.1)	112.0 (4.8)	4.17 (0.16)	2.73 (0.21)	393 (17)
200	-1 (0.05)	12.8 (0.5)	96.1 (4.5)	3.88 (0.17)	2.37 (0.20)	338 (16)

Table 5. *Parameters (Lorentz oscillator) obtained by fitting Drude-Smith and Lorentz model for 7 μJ/cm^2. (Errors are given in parentheses.)*

t_p (ps)	σ_1 (S/m)	ω_1 (THz)	τ_1(ps)	σ_2 (S/m)	ω_2 (THz)	τ_2 (ps)	f_1 (10^{12} S/ms)	f_2 (10^{13} S/ms)
0	6.6 (2.8)	0.75 (0.02)	1.8 (1.4)	27.8 (2.1)	1.797 (0.006)	1.0 (0.1)	3.6 (4.3)	2.8 (0.6)

5	7.9 (2.5)	0.75 (0.01)	1.8 (1.0)	23.5 (1.9)	1.797 (0.007)	1.0 (0.1)	4.5 (4.0)	2.4 (0.5)
10	7.8 (2.5)	0.73 (0.02)	1.6 (1.0)	22.7 (2.0)	1.771 (0.007)	1.1 (0.2)	4.7 (4.3)	2.1 (0.5)
20	8.0 (2.0)	0.71 (0.01)	1.5 (0.7)	17.1 (1.4)	1.791 (0.008)	0.8 (0.1)	5.4 (4.0)	2.0 (0.5)
30	5.3 (2.1)	0.69 (0.02)	1.6 (1.3)	26.1 (1.6)	1.763 (0.005)	1.1 (1.1)	3.2 (3.9)	2.4 (0.4)
40	6.3 (1.6)	0.76 (0.01)	1.6 (0.7)	19.3 (1.5)	1.753 (0.005)	1.3 (0.2)	3.9 (2.8)	1.5 (0.3)
50	5.4 (1.7)	0.72 (0.02)	1.5 (0.9)	20.9 (1.5)	1.767 (0.005)	1.2 (0.1)	3.6 (3.2)	1.7 (0.3)
60	5.2 (1.6)	0.75 (0.01)	1.7 (0.9)	19.0 (1.4)	1.788 (0.004)	1.3 (0.1)	3.1 (2.6)	1.5 (0.3)
70	4.5 (1.2)	0.75 (0.01)	1.4 (0.7)	10.2 (1.0)	1.777 (0.007)	1.1 (0.2)	3.3 (2.4)	0.9 (0.2)
80	3.3 (1.3)	0.71 (0.02)	1.8 (1.3)	15.7 (0.9)	1.779 (0.004)	1.1 (0.1)	1.8 (1.9)	1.4 (0.2)
200	1.4 (1.3)	0.77 (0.03)	2.7 (4.2)	7.9 (0.7)	1.855 (0.009)	0.7 (0.1)	0.5 (1.3)	1.1 (0.3)

Table 6. *Parameters (Drude-Smith) obtained by fitting Drude-Smith and Lorentz model for 17 μJ/cm^2. (Errors are given in parentheses.)*

t_p (ps)	c	σ_{dc} (S/m)	τ (fs)	ω_p (THz)	$n(t_p)$ (10^{15} cm^{-3})	$\mu(t_p)$ (cm^2/Vs)
0	-1 (0.05)	53.7 (1.7)	104.0 (4.1)	7.64 (0.27)	9.18 (0.66)	365 (14)
5	-1 (0.05)	45.7 (1.5)	102.0 (4.4)	7.11 (0.27)	7.97 (0.61)	358 (15)
10	-1 (0.05)	41.8 (1.4)	104.0 (4.3)	6.74 (0.25)	7.15 (0.53)	365 (15)
20	-1 (0.05)	37.1 (1.3)	104.5 (4.5)	6.34 (0.25)	6.33 (0.49)	367 (16)
40	-1 (0.05)	31.6 (1.1)	103.8 (4.6)	5.86 (0.23)	5.41 (0.43)	365 (16)
50	-1 (0.05)	27.9 (1.1)	98.1 (4.5)	5.66 (0.24)	5.05 (0.43)	345 (16)
60	-1 (0.07)	24.6 (1.1)	97.6 (5.1)	5.34 (0.25)	4.48 (0.43)	343 (18)
70	-1 (0.06)	20.6 (0.9)	98.2 (5.1)	4.87 (0.24)	3.73 (0.36)	345 (18)
80	-1 (0.06)	20.2 (0.9)	97.5 (4.6)	4.84 (0.22)	3.68 (0.33)	342 (16)
100	-1 (0.06)	16.2 (0.7)	94.8 (5.7)	4.39 (0.21)	3.03 (0.30)	333 (18)

Table 7*. Parameters (Lorentz oscillator) obtained by fitting Drude-Smith and Lorentz model for 17 μJ/cm^2. (Errors are given in parentheses.)*

t_p (ps)	σ_1 (S/m)	ω_1 (THz)	τ_1(ps)	σ_2 (S/m)	ω_2 (THz)	τ_2 (ps)	f_1 (10^{12} S/ms)	f_2 (10^{13} S/ms)
0	11.5 (3.5)	0.75 (0.02)	1.6 (0.9)	39.5 (2.7)	1.773 (0.006)	1.0 (0.1)	7.2 (6.2)	4.0 (0.7)
5	11.3 (3.4)	0.75 (0.01)	1.7 (0.9)	43.9 (2.8)	1.776 (0.004)	1.2 (0.1)	6.6 (5.5)	3.7 (0.6)
10	9.6 (3.0)	0.75 (0.97)	1.76 (1.75)	29.5 (2.3)	1.785 (0.009)	1.0 (0.1)	5.5 (7.2)	2.8 (0.6)
20	9.5 (2.7)	0.76 (0.01)	1.76 (0.89)	28.1 (2.1)	1.778 (0.006)	1.0 (0.1)	5.4 (4.3)	2.8 (0.5)
40	8.0 (2.4)	0.76 (0.01)	1.83 (0.97)	27.3 (1.9)	1.758 (0.005)	1.1 (0.1)	4.3 (3.7)	2.5 (0.4)
50	8.9 (1.8)	0.76 (0.01	1.23 (0.5)	22.1 (1.5)	1.786 (0.006)	0.8 (0.1)	7.2 (4.3)	2.6 (0.5)
60	10.0 (1.8)	0.74 (0.01)	1.1 (0.4)	23.3 (1.7)	1.773 (0.006)	1.0 (0.1)	9.5 (5.1)	2.7 (0.4)
70	10.6 (1.5)	0.76 (0.01)	1.1 (0.3)	15.0 (1.2)	1.797 (0.008)	0.8 (0.1)	9.3 (3.9)	1.8 (0.4)
80	9.6 (1.3)	0.76 (0.01)	1.1 (0.3)	12.5 (1.1)	1.812 (0.009)	0.8 (0.1)	9.1 (3.6)	1.5 (0.4)
100	7.5 (1.3)	0.76 (0.01)	1.1 (0.4)	18.1 (1.4)	1.748 (0.004)	1.5 (0.2)	6.9 (3.4)	1.2 (0.3)

Table 8. *Parameters (Drude-Smith) obtained by fitting Drude-Smith and Lorentz model for 24 μJ/cm^2. (Errors are given in parentheses.)*

t_p (ps)	c	σ_{dc} (S/m)	τ (fs)	ω_p (THz)	$n(t_p)$ (10^{15} cm^{-3})	$\mu(t_p)$ (cm^2/Vs)
0	-1 (0.06)	51.1 (2.3)	91.0 (4.8)	7.96 (0.40)	9.98 (0.97)	320 (17)
5	-1 (0.06)	45.8 (1.8)	89.7 (4.6)	7.59 (0.35)	9.08 (0.83)	315 (16)
10	-1 (0.05)	44.8 (1.7)	100.3 (4.7)	7.11 (0.30)	7.95 (0.67)	352 (16)
20	-1 (0.06)	38.4 (1.5)	86.0 (4.5)	7.10 (0.33)	7.93 (0.73)	302 (16)
30	-1 (0.06)	32.5 (1.3)	100.2 (4.94)	6.06 (0.27)	5.78 (0.51)	352 (17)
40	-1 (0.06)	27.0 (1.2)	92.0 (4.9)	5.76 (0.28)	5.23 (0.51)	323 (17)

50	-1 (0.06)	28.0 (1.2)	91.8 (4.7)	5.87 (0.27)	5.43 (0.51)	322 (17)
60	-1 (0.06)	25.6 (1.1)	91.3 (4.9)	5.63 (0.27)	4.99 (0.47)	321 (17)
70	-1 (0.06)	21.6 (1.0)	98.9 (5.5)	4.97 (0.26)	3.89 (0.40)	347 (19)
80	-1 (0.06)	18.1 (0.8)	91.1 (5.1)	4.74 (0.24)	3.54 (0.36)	320 (18)
100	-1 (0.06)	17.2 (0.7)	86.0 (4.6)	4.75 (0.22)	3.55 (0.33)	302 (16)
125	-1 (0.06)	14.8 (0.7)	84.0 (5.0)	4.47 (0.25)	3.14 (0.36)	295 (18)
150	-1 (0.06)	14.1 (0.6)	99.0 (5.9)	4.02 (0.21)	2.54 (0.27)	348 (21)

Table 9. *Parameters (Lorentz oscillator) obtained by fitting Drude-Smith and Lorentz model for 24 μJ/cm^2. (Errors are given in parentheses.)*

t_p (ps)	σ_2 (S/m)	ω_1 (THz)	τ_1(ps)	σ_2 (S/m)	ω_2 (THz)	τ_2 (ps)	f_1 (10^{12} S/ms)	f_2 (10^{13} S/ms)
0	21.2 (3.7)	0.77 (0.01)	1.0 (0.4)	20.3 (3.3)	1.819 (0.008)	0.9 (0.1)	39.2 (10.4)	4.4 (1.0)
5	14.6 (4.0)	0.77 (0.01)	1.6 (0.8)	9.3 (3.4)	1.799 (0.007)	1.1 (0.2)	34.8 (7.1)	3.1 (0.8)
10	12.9 (3.5)	0.75 (0.01)	1.6 (0.8)	8.15 (3.0)	1.776 (0.005)	1.1 (0.1)	41.7 (6.2)	3.6 (0.7)
20	11.6 (3.6)	0.77 (0.01)	1.7 (0.9)	7.0 (2.9)	1.795 (0.007)	1.1 (0.2)	29.9 (5.9)	2.7 (0.7)
30	7.6 (2.8)	0.76 (0.01)	1.7 (1.1)	4.4 (2.1)	1.808 (0.008)	1.0 (0.2)	21.5 (4.5)	2.2 (0.6)
40	8.3 (2.4)	0.77 (0.01)	1.4 (0.7)	5.7 (1.9)	1.840 (0.009)	0.9 (0.1)	19.2 (4.6)	2.1 (0.5)
50	6.7 (2.5)	0.76 (0.02)	1.6 (1.0)	4.2 (1.8)	1.812 (0.008)	0.9 (0.1)	20.0 (4.3)	2.2 (0.5)
60	8.6 (2.2)	0.76 (0.01)	1.5 (0.7)	6.0 (2.0)	1.809 (0.006)	1.1 (0.2)	23.2 (4.4)	2.0 (0.5)
70	10.5 (1.7)	0.79 (0.01)	1.1 (0.3)	9.2 (1.7)	1.769 (0.005)	1.2 (0.1)	24.1 (4.3)	2.1 (0.4)
80	5.5 (1.7)	0.75 (0.02)	1.5 (0.9)	3.6 (1.2)	1.816 (0.011)	0.8 (0.1)	10.6 (3.0)	1.4 (0.4)
100	2.9 (1.8)	0.77 (0.03)	1.9 (2.0)	1.5 (1.3)	1.830 (0.009)	1.1 (0.2)	11.4 (2.5)	1.0 (0.3)
125	5.4 (1.6)	0.78 (0.02)	1.5 (0.8)	3.7 (1.4)	1.746 (0.007)	1.2 (0.2)	13.3 (2.9)	1.2 (0.3)
150	5.3 (1.6)	0.78 (0.01)	2.1 (1.0)	2.6 (1.3)	1.760 (0.007)	1.3 (0.2)	12.0 (2.1)	0.9 (0.3)

200	3.7 (1.4)	0.79 (0.02)	1.6 (1.0)	2.3 (1.2)	1.762 (0.008)	1.2 (0.2)	9.9 (2.3)	0.8 (0.3)

Together with pumps scan and probe scans, we obtained different transport parameters. In high bandgap semiconductors, in present case of TlBr NCs film, high carrier mobility and long diffusion lengths might suggest a minimal density of deep-trap states in TlX NCs.

f) Comparison of frequency-averaged and frequency-resolved studies

We have compared the THz kinetics obtained from frequency-averaged and frequency-resolved studies. Carrier dynamics obtained from both methods are similar to the pump-probe delay time, which is less than 275 ps, as shown in Figure 15. Carrier density at particular pump-probe delay (t_p) is calculated from Drude DC conductivity and scattering time (τ) as per equation 12. Normalised carrier density from frequency-resolved (probe scan) at different delays and normalised THz transients (pump scan) at similar fluence are plotted for comparing carrier dynamics. Both methods observe a striking similarity in THz kinetics, which is logically expected as the sample should behave/decay similarly under the same photoexcitation conditions as shown in Figures 15a, 15b and 15c.

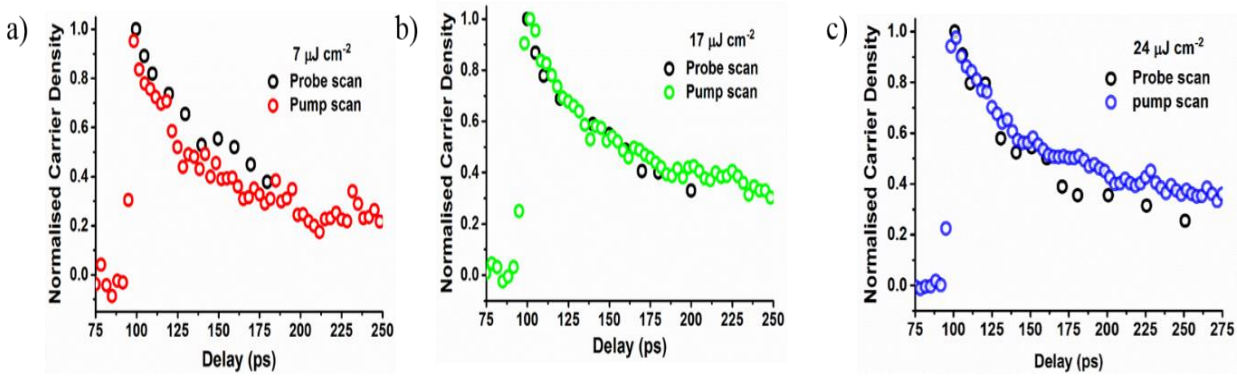

Figure 15. *THz kinetics from frequency-averaged and frequency-resolved THz studies three excitations fluence a)7 μJ/cm^2 b)17 μJ/cm^2 and c)24 μJ/cm^2.*

3.3.2 Charge carrier dynamics in bulk TlBr and TlI

Thin films of thallium halides coated on HDPE substrate were studied using the optical-pump THz-probe spectroscopy. HDPE has negligible and uniform (flat) absorption in the THz

range (below 8 THz). Bulk TlBr and TlI films were investigated using time-resolved THz spectroscopy to study charge carrier dynamics and compare charge carrier dynamics with thallium halide NCs films. To photoexcite the bulk TlX films, a wavelength of 400 nm was chosen, which excited the sample at band edge or just over the bandgap. The film thickness was around 67.8 μm and 26.4 μm for TlBr and TlI, respectively. The thickness of the films were smaller than the wavelength of THz radiation; thallium halide films can be considered optically thin at THz frequency (1 THz ≅ 300 μm). Excitation fluences are in the range of 11.3 to 117 μJ/cm^2, we use equations for N_{Ph}.

$$N_{Ph} = \frac{F_l(1-R)}{\delta\ h\nu} \tag{15}$$

Here δ is penetration depth at a pump wavelength of 400 nm from our earlier study on Thallium halide[8] and R is reflectance. Carrier density (N_0) was found to be varying in the range of from 1.7 x 10^{16} to 17.6 x 10^{16} cm^{-3}. N_0 is calculated from N_{ph} as $N_0 = \varphi\ 2N_{Ph}$. Here φ is the photon to charge conversion ratio. Figures 16a and 16c show the plot of negative differential transmissions $\left(-\frac{\Delta E}{E_{off}}\right)$ against the pump-probe delay time at various fluences for bulk TlBr and TlI films, respectively. We plotted maximum of negative differential transmission with respect to fluence; this trend varies well with linear relation as shown in Figures 16b and 16d. We normalised all negative differential transmission traces with their respective maximum value to observe their fluence dependency (Figures 17a and 17b). We observed that the carrier dynamics of TlBr slow down with fluence, and the carrier dynamics of TlI remain independent of fluence. We have fitted THz transients of Thallium halides to a multiexponential function to get different time components. The multiexponential function was used to model THz transients, and time components for each trace were acquired with their respective contribution. Table 4 and Table 5 list all the time components obtained from multiexponential fitting with different excitation fluences.

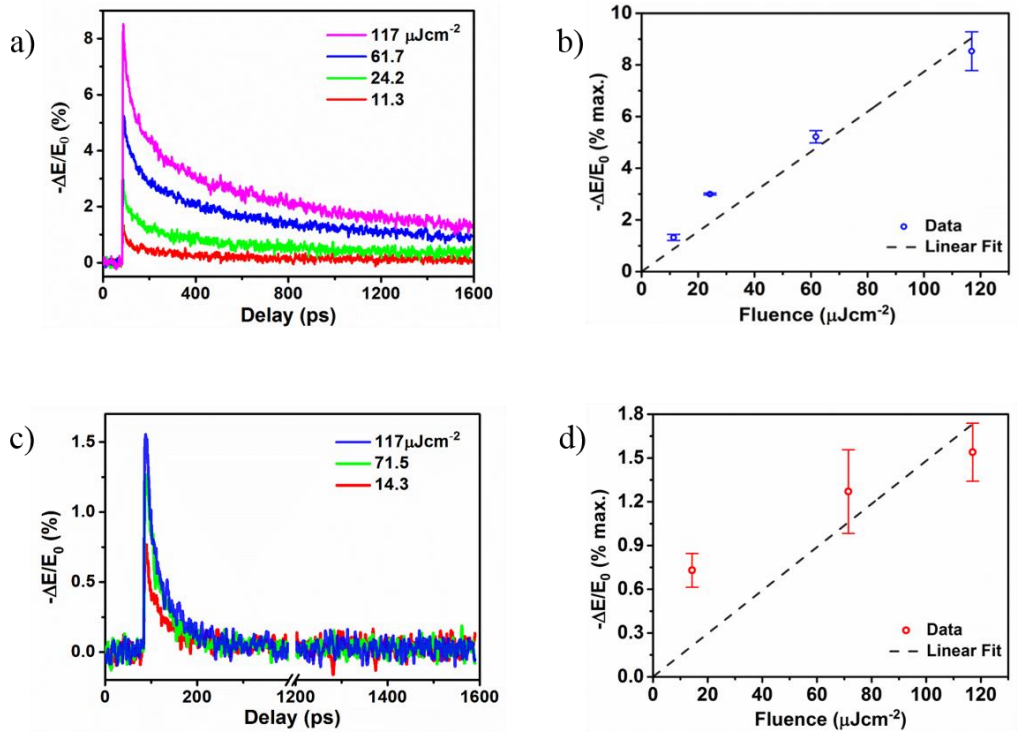

Figure 16. *Differential transmission of a) bulk TlBr and c) bulk TlI (break on the x-axis from 400 to 1200 ps). Maximum of differential transmission vs fluence of and their linear fits b) bulk TlBr film (adj. R^2~0.98) and d) bulk TlI film (adj. R^2~0.88).*

In TlBr three exponential functions were required to fit THz transients while for TlI two exponentials were adequate to fit fluence-dependent THz transients.

In TlBr, the fastest time component (t_1), which increases very slowly with fluence, can be assigned to the trap-filling process. The intermediate time component (t_2) also rises slowly with excitation fluence but has a larger magnitude than the fastest time component. This could be because the trap saturation process and traps involved in the second process could have different nature than the previous process (related t_1). Here we note that the photoexcited carrier density is sufficiently larger than available defect-state density and as a result the the slowest time component (t_3) decreases with fluence. This time constant could be due to bimolecular recombination or trap-assisted recombination. Overall carrier recombination with an average lifetime ($< t >$) of 2330 to 1530 ps becomes faster as fluence increases. Time constants obtained by fitting THz transients of TlBr and of TlI are listed in the Table 10.

In the case of bulk TlI, two time components were obtained with their respective contribution (Table 11). Both these time components are independent of photoexcitation fluence. The

fastest time component (t_1) is around 20 ps, with a higher contribution to total carrier dynamics. The slowest time component (t_2) is about 100 ps. Trap states filling might be occurring at a very fast time scale. In contrast, other types of trap-state filling or trap-assisted recombination could be possible for the slowest process corresponding to 100 ps. Overall average time scale ($< t >$) is independent of fluence and almost one order of magnitude faster than the average time scale of bulk TlBr.

Table 10. *Time constants obtained from fitting THz transient of bulk TlBr. (Errors are given in parentheses.)*

Fluence μJ/cm^2	N_0 (10^{16} cm^{-3})	t_1 (ps)	a_1	t_2 (ps)	a_2	t_3 (ps)	a_3	$< t >$ (ps)
116.9	17.66	34.4 (0.2)	0.310 (0.001)	202.4 (1.3)	0.269 (0.000)	1672.7 (4.5)	0.367 (0.000)	1528.9 (3.7)
61.7	9.32	41.0 (0.2)	0.314 (0.001)	257.4 (2.0)	0.318 (0.000)	2110.7 (12.2)	0.350 (0.001)	1896.6 (11.1)
24.2	3.64	28.8 (0.2)	0.378 (0.001)	252.9 (2.5)	0.322 (0.001)	2570 (41.3)	0.206 (0.002)	2222.9 (39.6)
11.3	1.7	15.1 (0.1)	0.546 (0.003)	201.4 (1.9)	0.347 (0.001)	2772.1 (71.6)	0.137 (0.001)	2329.9 (69.8)

Table 11. *Time constants obtained from fitting THz transient of bulk TIl. (Errors are given in parentheses.)*

Fluence (μJ/cm^2)	N_0 (10^{16} cm^{-3})	t_1 (ps)	a_1	t_2 (ps)	a_2	$< t >$ (ps)
117	24.9	21.3 (0.1)	0.776 (0.002)	101.0 (0.6)	0.280 (0.003)	71.6 (0.6)
71.5	15.22	25.0 (0.2)	0.828 (0.004)	100.0 (1.1)	0.229 (0.004)	64.4 (1.0)
14.3	3.04	18.5 (0.2)	0.607 (0.004)	100.0 (0.9)	0.386 (0.004)	81.6 (0.7)

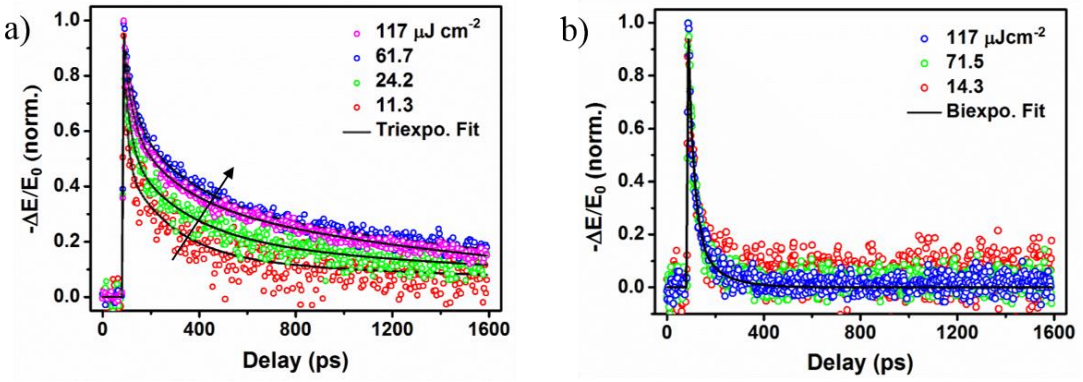

Figure 17. *Normalised THz transients of a) bulk TlBr film b) bulk TlI NCs film and their multiexponential fits.*

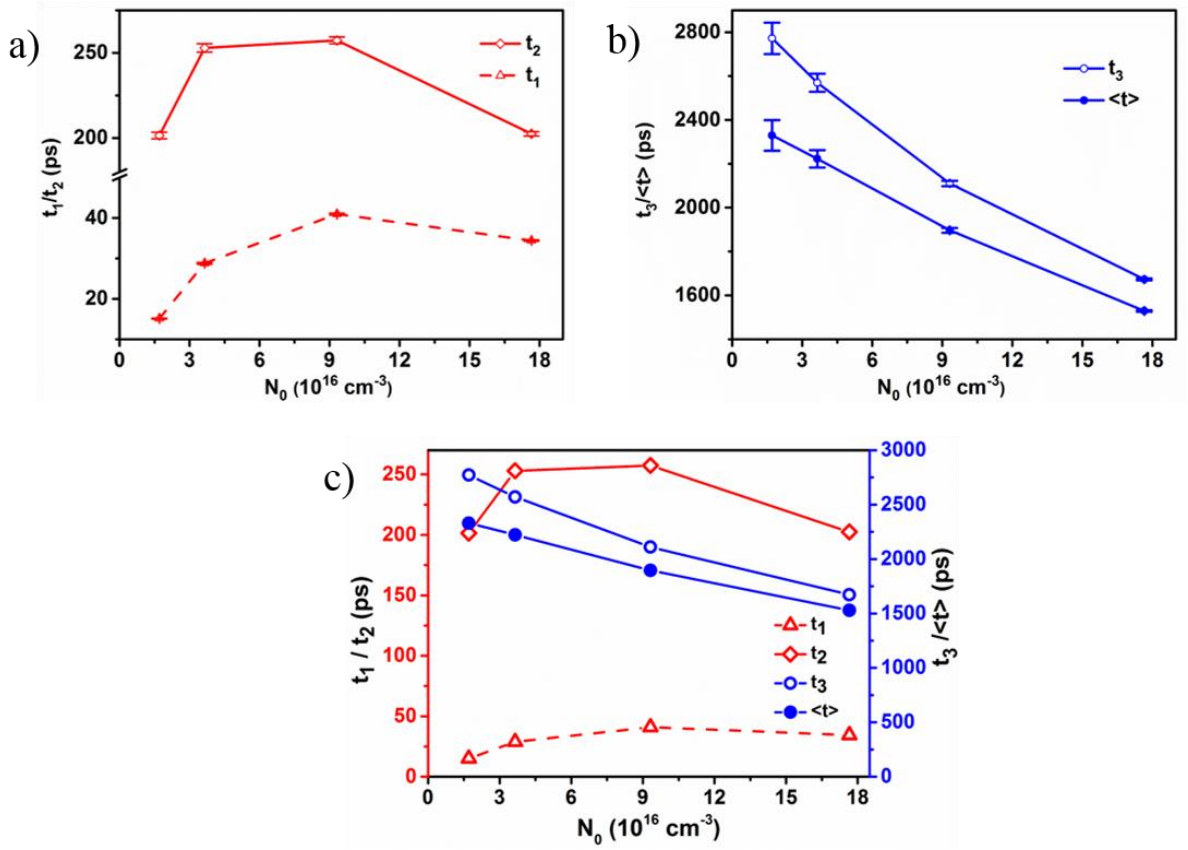

Figure 18. *Time constants obtained by fitting THz transients of bulk TlBr a) t_1 and t_2 with respective residual (break on y-axis from 50 to 180 ps for visual clarity) b) t_3 and <t>(with respective residual) and c) All time constants and <t> (without residual).*

a) Charge carrier mobility and diffusion length of bulk Thallium Halides

Charge carrier mobility and diffusion lengths were determined from the peak photoconductivity of the bulk thallium halide and are listed in the Table 12 and Table 13 below. Fluence dependent mobility and diffusion lengths are plotted in Figures 19a and 19b respectively. At the lowest fluence of around 11.3 μJ/cm^2, mobility is about 65 cm^2/Vs, and diffusion length is approximately 0.6 μm for TlBr. At the fluence of 14.3 μJ/cm^2, mobility is found to be 60.95 cm^2/Vs and diffusion length is found to be 0.11 μm for TlI. The charge carrier mobility is sufficiently high, and the diffusion length is long for the thin film considering the experiment was conducted at a photons density of 10^{16} -10^{17} cm^{-3}. In the Table 15, we have compared the mobility and the diffusion length of several large bandgaps (lie in UV-visible range) semiconductors.

Table 12. *Effective mobility and diffusion length of bulk TlBr. (Errors are given in parentheses.)*

Fluence μJ/cm^2	Photons per pulse (10^{14} cm^{-2})	N_{Ph} (10^{16} cm^{-3})	N_0 (10^{16} cm^{-3})	$\frac{-\Delta E}{E_0}(max.)$	Peak Conductivity (Sm^{-1})	Mobility (cm^2/Vs)	L_d (um)
116.9	2.3539	8.83	17.66	0.085 (0.007)	115.1 (10.1)	40.7 (3.6)	0.401 (0.018)
61.7	1.24234	4.66	9.32	0.052 (0.002)	70.4 (3.2)	47.2 (2.2)	0.481 (0.012)
24.2	0.486475	1.82	3.64	0.030 (0.0004)	40.5 (0.5)	69.2 (0.8)	0.631 (0.009)
11.3	0.227545	0.85	1.70	0.013 (0.001)	17.8 (1.6)	65.1 (5.7)	0.627 (0.037)

Table 13. *Effective mobility and diffusion length of bulk TlI. (Errors are given in parentheses.)*

Fluence (μJ/cm^2)	Photons per pulse (10^{14} cm^{-2})	N_{ph} (10^{16} cm^{-3})	N_0 (10^{16} cm^{-3})	$\frac{-\Delta E}{E_0}(max.)$	Peak conductivity (Sm^{-1})	Mobility (cm^2/Vs)	L_d (um)
117	2.354	12.45	24.9	0.015 (0.002)	62.7 (8.1)	15.71 (2.02)	0.054 (0.004)
71.5	1.438	7.61	15.22	0.013 (0.003)	51.7 (11.7)	21.21 (4.78)	0.059 (0.007)
14.3	0.288	1.52	3.04	0.007 (0.001)	29.7 (4.7)	60.95 (9.67)	0.113 (0.009)

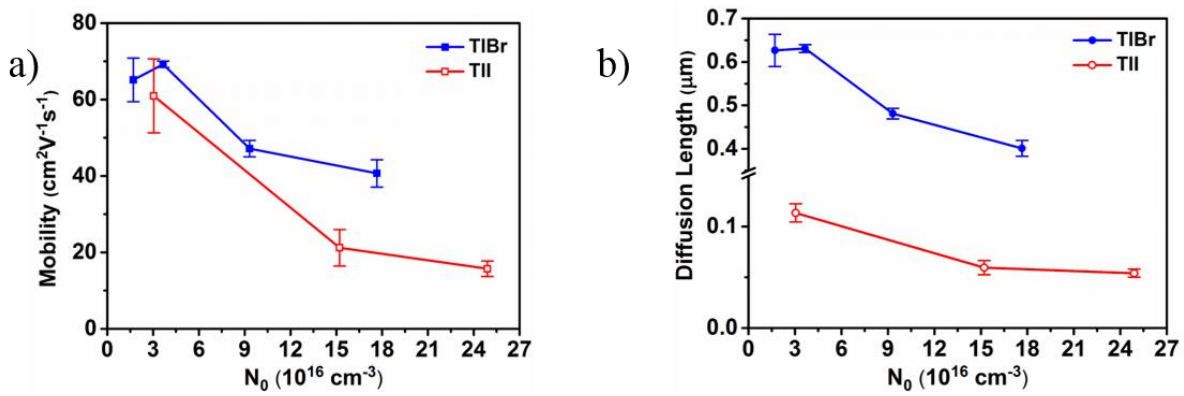

Figure 19. *a) Effective mobility and b) Diffusion length (break from 1.5 to 3.5 μm) of bulk TlBr and TlI.*

3.4 Comparison of charge carrier dynamics in bulk and nanocrystals thallium halide films

a) Charge carrier dynamics in Thallium halides

We could qualitatively compare the carrier dynamics of NCs and bulk films by studying their fluence-dependent THz transients even though we studied them at different photon densities (ranging from 10^{15} to 10^{16} cm^{-3}). In bulk and NCs film of TlI, similar time scales for carrier recombination were obtained with photon density of two orders of difference. In TlBr NCs and bulk film, charge carrier dynamics is found to be slowing down with an increase in the carrier density. Carrier recombination dynamics in bulk TlBr is slower than that in the NCs film mostly due to relatively slower trap-assisted recombination process in bulk TlBr. Overall, we do not observe any stark difference in carrier recombination dynamics of TlX between NCs and bulk forms. This may have resulted from NC size being larger than/comparable to the Bohr excitonic radii of TlX. Hence it will be interesting to investigate and understand the effects of size and quantum confinement on carrier dynamics at smaller NCs than those examined in this work.

b) Possible defect-tolerance in Thallium halide from mobility and diffusion length

Our study on NCs of TlBr and TlI films reveals very high mobility and long diffusion length.[8] The mobility and diffusion lengths for thallium halides films studied in this chapter are in the same order compared to halide perovskite film around excitation conditions, as shown in Table 14.[8, 40-42]

Generally, semiconductors with bandgap in UV-region possess high density of defects in mid gap which can be detrimental to their applications.[7] We have listed semiconductors with bandgap in UV-range in Table 15, which shows mobility, diffusion lengths and PLQY. High PL efficiency in such high bandgap semiconductors is also reasonable.

Our study shows that TlBr and TlI display high mobility, long diffusion length and fairly high PL efficiency, and all these features suggest that TlX could be a defect-tolerant semiconductor system.

Table 14. *Mobility and diffusion lengths of our films and metal halide perovskites measured through the TRTS technique.*

Sample (Film)	Carrier density N_0 (cm^{-3})	Mobility (cm^2/Vs)	Diffusion length (μm)	Ref.
TlBr NCs	1.7×10^{15}	260	0.97	[8]
TlBr bulk	1.70×10^{16}	65.1	0.627	unpublished (this work)
TlI NCs	1.76×10^{15}	91	0.13	[8]
TlI bulk	3.04×10^{16}	60.95	0.113	unpublished (this work)
$CH_3NH_3PbI_3$ bulk	6×10^{17}	8.2	~0.2	[41]
$FAPbI_3$ bulk	$\sim 10^{15}$	27	3.14	[40]
$FAPbBr_3$ bulk	$\sim 10^{15}$	14	1.26	[40]
$CsPbBr_3$ NCs	1.1×10^{18}	60	-	[42]
$CsPbBr_3$ thin film	$\sim 10^{14}$	170	0.7	[43]

Table 15. *Mobility, diffusion length and PLQY in semiconductors with bandgap in UV-range. (* denotes data obtained from thin film)*

Sample	Optical gap (eV), λ	PLQY (%)	Mobility ($cm^2V^{-1}s^{-1}$)	Diffusion Length (μm)	Technique adapted	Ref.
TlBr NCs	3.1, 400	10	350	0.8	THz	unpublished (this work),[8]
TlI NCs	2.8, 436	6	250	0.25	THz	unpublished (this work),[8]
TlBr bulk			μ_e = 40.2 μ_h = 11.8		Conductivity, Drift mobility	44
$CsPbCl_3$ QD Solid	3.02, 410	3, 1*				45
Carbon-dots QDs	2.69, 460	4-10, 57*	*μ_e = 8.5 x 10^{-5} *μ_h = 3.8 x 10^{-5}		FET measurement	46-48
CdS nanorod	3.2, 383	10	32		I-V characteristics	49, 50
CdS NCs	2.58, 480	6.4				51, 52
CdS thin film bulk			17		TFT	53
CdSe NCs	2.4 -2.7, 450 – 500	Few % - 10%	1 – 100		THz	26, 54
ZnSe NCs	3.3- 2.8, 370-430	10-50				55
ZnSe single Crystal			267, 40*, 0.017*		THz, I-V characteristics	56, 57
CdSe/ZnS Core shell	2.53, 490	30				58

The wide bandgap semiconductor system, Thallium Halides (TlX), holds promise mainly in high-energy radiation detector applications. Radiation detection principally relies on photoexcited state properties of semiconductors under consideration. In addition, this family of semiconductors (TlX) offer to check defect-tolerant properties in semiconductor due to their electronic band structure resemblance to metal halide perovskites, which is highly important in view of the optoelectronic properties of any given semiconductors.

Here, we presented our work on two semiconductors of this TlX system, TlBr and TlI, in the form of nanocrystal thin films and bulk thin films. We studied thin films on (non-conducting)

substrates of semiconductors using ultrafast THz spectroscopic techniques such as THz-TDS and TRTS. The main advantage of studying semiconductors using THz spectroscopy is measuring steady state and dynamical electronic properties in non-contact and non-invasive manners. In our study, we found that carrier dynamics upon exciting TlX NCs films just above/around the bandgap give completely different dynamics at similar photoexcitation carrier concentration for TlBr and TlI, which show the nature of halides affects the carrier dynamics. THz spectroscopy traces important device parameters such as carrier mobility, diffusion length, and carrier lifetime. Our study found that carrier mobility is reasonably high (~250 cm^2/Vs) and diffusion length (~1 μm) is long, which directly correlates with the defect environment of semiconductors and its effect on carrier transport. Hence, we suspect that TlX possibly shows a defect-tolerant electronic band structure due to promising transport properties traced by THz spectroscopy. We understand that many different experimental studies under different conditions will be required to strengthen the defect-tolerant claim; our study partially but reasonably supports this claim. To compare carrier dynamics of TlX NCs film to bulk film, we carried out similar experiments on TlBr and TlI bulk films coated on substrates. Our study finds that carrier dynamics show a similar trend for bulk thallium halide films. Here, it is to be noted that carrier dynamics have been studied at different excitation photon densities for bulk TlX. In this bulk TlX film, we found reasonable mobility (~65 cm^2/Vs) and diffusion length considering (~0.6 μm) one to two orders of magnitude higher of excitation photon density. As discussed in Chapter 1 and Chapter 2, the unique interaction of THz photon with matter makes it possible to monitor excited properties and evaluate important device parameters.

3.5 Conclusions

Thallium halides are one the promising semiconductor systems mainly for application in high-energy radiation detectors, which is entirely dependent on the photoexcited state properties of these semiconductors. Additionally, thallium halides share the same electronic band structure as metal halide perovskites due to their similar composition, which may have a significant impact on their electrical and transport properties. In this chapter, we investigated charge carrier dynamics in Thallium halide nanocrystal thin film and bulk thin films using ultrafast time-resolved THz spectroscopy. High mobility, long diffusion length, and fairly high PLQY of Thallium halides suggest the possible defect-tolerant nature of its electronic band structure. Charge carrier dynamics is studied by two methods (frequency-averaged and frequency-resolved THz studies); from both methods, we found high mobility and similar carrier dynamics in TlX. These transport properties can be very well utilised in their potential optoelectronics applications. We also found the presence of low-frequency phonon absorption in Thalium halides in nanocrystal films through steady-state and photoexcited-state THz studies. As a result, electron-phonon coupling and its effect on carrier transport in Thallium halides is an interesting study for future experiments. Excited state carrier shows strong carrier localization as (complex) photoconductivity deviates from a pure free carrier-like Drude's response.

We observed a weak effect of particle size on charge carrier dynamics when comparing TlX NCs and bulk films. Our THz spectroscopic study of Thallium halides has unravelled their charge carrier dynamics and has investigated transport properties in a non-contact manner by measuring their mobility and diffusion length. It is interesting to conduct similar experiments on Thallium halide semiconductor systems on thinner films (a few 10s to 100s of nanometers) and at similar photoexcitation conditions to gain an even more fundamental understanding. Also, further investigation of optoelectronic properties using various contact and non-contact techniques will help in confirming the practical usefulness of thallium halides for its specific applications, and our research will contribute to this effort.

3.6 References

1. Protesescu, L.; Yakunin, S.; Bodnarchuk, M. I.; Krieg, F.; Caputo, R.; Hendon, C. H.; Yang, R. X.; Walsh, A.; Kovalenko, M. V., Nanocrystals of Cesium Lead Halide Perovskites (CsPbX3, X = Cl, Br, and I): Novel Optoelectronic Materials Showing Bright Emission with Wide Color Gamut. *Nano Letters* **2015,** *15* (6), 3692-3696.
2. Yakunin, S.; Protesescu, L.; Krieg, F.; Bodnarchuk, M. I.; Nedelcu, G.; Humer, M.; De Luca, G.; Fiebig, M.; Heiss, W.; Kovalenko, M. V., Low-threshold amplified spontaneous emission and lasing from colloidal nanocrystals of caesium lead halide perovskites. *Nature Communications* **2015,** *6* (1), 8056.
3. Tan, Z.-K.; Moghaddam, R. S.; Lai, M. L.; Docampo, P.; Higler, R.; Deschler, F.; Price, M.; Sadhanala, A.; Pazos, L. M.; Credgington, D.; Hanusch, F.; Bein, T.; Snaith, H. J.; Friend, R. H., Bright light-emitting diodes based on organometal halide perovskite. *Nature Nanotechnology* **2014,** *9* (9), 687-692.
4. Kim, J. Y.; Lee, J.-W.; Jung, H. S.; Shin, H.; Park, N.-G., High-Efficiency Perovskite Solar Cells. *Chemical Reviews* **2020,** *120* (15), 7867-7918.
5. Mudring, A.-V., Thallium Halides – New Aspects of the Stereochemical Activity of Electron Lone Pairs of Heavier Main-Group Elements. *European Journal of Inorganic Chemistry* **2007,** *2007* (6), 882-890.
6. Brandt, R. E.; Stevanović, V.; Ginley, D. S.; Buonassisi, T., Identifying defect-tolerant semiconductors with high minority-carrier lifetimes: beyond hybrid lead halide perovskites. *MRS Communications* **2015,** *5* (2), 265-275.
7. Talapin, D. V.; Lee, J.-S.; Kovalenko, M. V.; Shevchenko, E. V., Prospects of Colloidal Nanocrystals for Electronic and Optoelectronic Applications. *Chemical Reviews* **2010,** *110* (1), 389-458.
8. Mir, W. J.; Warankar, A.; Acharya, A.; Das, S.; Mandal, P.; Nag, A., Colloidal thallium halide nanocrystals with reasonable luminescence, carrier mobility and diffusion length. *Chemical Science* **2017,** *8* (6), 4602-4611.
9. Stoumpos, C. C.; Malliakas, C. D.; Peters, J. A.; Liu, Z.; Sebastian, M.; Im, J.; Chasapis, T. C.; Wibowo, A. C.; Chung, D. Y.; Freeman, A. J.; Wessels, B. W.; Kanatzidis, M. G., Crystal Growth of the Perovskite Semiconductor CsPbBr3: A New Material for High-Energy Radiation Detection. *Crystal Growth & Design* **2013,** *13* (7), 2722-2727.
10. Kim, H.; Kargar, A.; Cirignano, L.; Churilov, A.; Ciampi, G.; Higgins, W.; Olschner, F.; Shah, K., Recent Progress in Thallium Bromide Gamma-Ray Spectrometer Development. *IEEE Transactions on Nuclear Science* **2012,** *59* (1), 243-248.
11. Hitomi, K.; Shoji, T.; Ishii, K., Advances in TlBr detector development. *Journal of Crystal Growth* **2013,** *379*, 93-98.
12. Agekyan, V. F.; Akai, I.; Karasawa, T., Morphology and optical spectra of metal iodate microcrystals in porous matrices. *Physics of the Solid State* **2003,** *45* (6), 1170-1176.
13. Bachrach, R. Z.; Brown, F. C., Exciton-Optical Properties of TlBr and TlCl. *Physical Review B* **1970,** *1* (2), 818-831.
14. Hodby, J. W.; Jenkin, G. T.; Kobayashi, K.; Tamura, H., Cyclotron resonance of electrons and of holes in thallium chloride and in thallium bromide. *Solid State Communications* **1972,** *10* (11), 1017-1020.
15. Agekyan, V. F.; Stepanov, Y. A., Optical and structural properties of thallium halide microcrystals in a porous matrix. *Physics of the Solid State* **2001,** *43* (4), 763-765.

16. Takiyama, K.; Nakahara, J.; Takenaka, H.; Kobayashi, K.; Fujita, T.; Fujii, A., High Density Excitation Effect of the Indirect Band Luminescence in Thallous Halides*. *Journal of the Physical Society of Japan* **1996,** *65* (1), 307-311.
17. Heidrich, K.; Staude, W.; Treusch, J.; Overhof, H., Optical Properties and Electronic Structure of Polymorphous TICI and TIBr. *Physical Review Letters* **1974,** *33* (20), 1220-1223.
18. Leão, C. R.; Lordi, V., Simultaneous Control of Ionic and Electronic Conductivity in Materials: Thallium Bromide Case Study. *Physical Review Letters* **2012,** *108* (24), 246604.
19. Muduli, S. K.; Varrla, E.; Xu, Y.; Kulkarni, S. A.; Katre, A.; Chakraborty, S.; Chen, S.; Sum, T. C.; Xu, R.; Mathews, N., Evolution of hydrogen by few-layered black phosphorus under visible illumination. *Journal of Materials Chemistry A* **2017,** *5* (47), 24874-24879.
20. Deng, Y.; Peng, E.; Shao, Y.; Xiao, Z.; Dong, Q.; Huang, J., Scalable fabrication of efficient organolead trihalide perovskite solar cells with doctor-bladed active layers. *Energy & Environmental Science* **2015,** *8* (5), 1544-1550.
21. Hattori, K., Exciton Binding Energies in Polar Crystals. *physica status solidi (b)* **1976,** *76* (1), 281-287.
22. Ohno, N.; Nakamura, K.; Nakai, Y., Optical Properties of Orthorhombic Thallous Iodide. *Journal of the Physical Society of Japan* **1986,** *55* (10), 3659-3663.
23. Ohno, N., Time-resolved photoluminescence of exciton–polaritons in orthorhombic TlI. *Journal of Luminescence* **2006,** *119-120*, 47-50.
24. Nienhuys, H.-K.; Sundström, V., Intrinsic complications in the analysis of optical-pump, terahertz probe experiments. *Physical Review B* **2005,** *71* (23), 235110.
25. Wahlstrand, J. K.; Heilweil, E. J., Contactless THz-based bulk semiconductor mobility measurements using two-photon excitation. *Optics Express* **2018,** *26* (23), 29848-29853.
26. Beard, M. C.; Turner, G. M.; Schmuttenmaer, C. A., Size-Dependent Photoconductivity in CdSe Nanoparticles as Measured by Time-Resolved Terahertz Spectroscopy. *Nano Letters* **2002,** *2* (9), 983-987.
27. Lakowicz, J. R., *Principles of Fluorescence Spectroscopy*. Springer US: **2011**.
28. Parkinson, P.; Joyce, H. J.; Gao, Q.; Tan, H. H.; Zhang, X.; Zou, J.; Jagadish, C.; Herz, L. M.; Johnston, M. B., Carrier Lifetime and Mobility Enhancement in Nearly Defect-Free Core−Shell Nanowires Measured Using Time-Resolved Terahertz Spectroscopy. *Nano Letters* **2009,** *9* (9), 3349-3353.
29. Zhang, X.; Li, M.; Wu, B.; Ekahana, S. A.; Utama, M. I. B.; Xing, G.; Xiong, Q.; Sum, T. C. In *Size and Surface Effects on Transient Photoconductivity in CdS Nanobelts Probed by Optical Pump-Terahertz Probe Spectroscopy*, Asia Communications and Photonics Conference 2013 Postdeadline, Beijing, 2013/11/12; Optica Publishing Group: Beijing, **2013**; p AF2A.7.
30. Shi, Y.; Zhou, Q.-l.; Zhang, C.; Jin, B., Ultrafast high-field carrier transport in GaAs measured by femtosecond pump-terahertz probe spectroscopy. *Applied Physics Letters* **2008,** *93* (12), 121115.
31. Deng, X.; Wen, X.; Huang, S.; Sheng, R.; Harada, T.; Kee, T. W.; Green, M.; Ho-Baillie, A., Ultrafast Carrier Dynamics in Methylammonium Lead Bromide Perovskite. *The Journal of Physical Chemistry C* **2016,** *120* (5), 2542-2547.
32. Ulbricht, R.; Hendry, E.; Shan, J.; Heinz, T. F.; Bonn, M., Carrier dynamics in semiconductors studied with time-resolved terahertz spectroscopy. *Reviews of Modern Physics* **2011,** *83* (2), 543-586.

33. Kar, S.; Jayanthi, S.; Freysz, E.; Sood, A. K., Time resolved terahertz spectroscopy of low frequency electronic resonances and optical pump-induced terahertz photoconductivity in reduced graphene oxide membrane. *Carbon* **2014,** *80*, 762-770.
34. Duvillaret, L.; Garet, F.; Coutaz, J.-L.; Whitaker, J. F. In *A Reliable Method for the Extraction of Material Parameters of Thick and Thin Samples in THz Time-Domain Spectroscopy*, Ultrafast Electronics and Optoelectronics, Incline Village, Nevada, 1997/03/17; Nuss, M.; Bowers, J., Eds. Optica Publishing Group: Incline Village, Nevada, **1997**; p UF10.
35. Cowley, E. R.; Okazaki, A.; Cochran, W., The lattice dynamics of thallous bromide. *Proceedings of the Royal Society of London. Series A. Mathematical and Physical Sciences* **1967,** *300* (1460), 45-61.
36. Kushwaha, M. S., Phonon dispersion in thalous halides. *Physica B+C* **1984,** *125* (1), 45-52.
37. Du, M.-H.; Singh, D. J., Enhanced Born charge and proximity to ferroelectricity in thallium halides. *Physical Review B* **2010,** *81* (14), 144114.
38. Joyce, H. J.; Boland, J. L.; Davies, C. L.; Baig, S. A.; Johnston, M. B., A review of the electrical properties of semiconductor nanowires: insights gained from terahertz conductivity spectroscopy. *Semiconductor Science and Technology* **2016,** *31* (10), 103003.
39. Ulatowski, A. M.; Herz, L. M.; Johnston, M. B., Terahertz Conductivity Analysis for Highly Doped Thin-Film Semiconductors. *Journal of Infrared, Millimeter, and Terahertz Waves* **2020,** *41* (12), 1431-1449.
40. Rehman, W.; Milot, R. L.; Eperon, G. E.; Wehrenfennig, C.; Boland, J. L.; Snaith, H. J.; Johnston, M. B.; Herz, L. M., Charge-Carrier Dynamics and Mobilities in Formamidinium Lead Mixed-Halide Perovskites. *Advanced Materials* **2015,** *27* (48), 7938-7944.
41. Wehrenfennig, C.; Eperon, G. E.; Johnston, M. B.; Snaith, H. J.; Herz, L. M., High Charge Carrier Mobilities and Lifetimes in Organolead Trihalide Perovskites. *Advanced Materials* **2014,** *26* (10), 1584-1589.
42. Cinquanta, E.; Meggiolaro, D.; Motti, S. G.; Gandini, M.; Alcocer, M. J. P.; Akkerman, Q. A.; Vozzi, C.; Manna, L.; De Angelis, F.; Petrozza, A.; Stagira, S., Ultrafast THz Probe of Photoinduced Polarons in Lead-Halide Perovskites. *Physical Review Letters* **2019,** *122* (16), 166601.
43. Gatto, L.; Treglia, A.; Crippa, G.; Devetta, M.; Folpini, G.; Petrozza, A.; Stagira, S.; Vozzi, C.; Cinquanta, E., Time-resolved terahertz spectroscopy for probing the effects of low-temperature annealing on CsPbBr3 evaporated thin-films. *Journal of Optics* **2022,** *24* (10), 104001.
44. Hitomi, K.; Matsumoto, M.; Muroi, O.; Shoji, T.; Hiratate, Y., Thallium bromide optical and radiation detectors for X-ray and gamma-ray spectroscopy. *IEEE Transactions on Nuclear Science* **2002,** *49* (5), 2526-2529.
45. Kim, Y.; Yassitepe, E.; Voznyy, O.; Comin, R.; Walters, G.; Gong, X.; Kanjanaboos, P.; Nogueira, A. F.; Sargent, E. H., Efficient Luminescence from Perovskite Quantum Dot Solids. *ACS Applied Materials & Interfaces* **2015,** *7* (45), 25007-25013.
46. Liu, W.; Xu, S.; Li, Z.; Liang, R.; Wei, M.; Evans, D. G.; Duan, X., Layer-by-Layer Assembly of Carbon Dots-Based Ultrathin Films with Enhanced Quantum Yield and Temperature Sensing Performance. *Chemistry of Materials* **2016,** *28* (15), 5426-5431.

47. Kwon, W.; Do, S.; Won, D. C.; Rhee, S.-W., Carbon Quantum Dot-Based Field-Effect Transistors and Their Ligand Length-Dependent Carrier Mobility. *ACS Applied Materials & Interfaces* **2013,** *5* (3), 822-827.
48. Sun, Y.-P.; Zhou, B.; Lin, Y.; Wang, W.; Fernando, K. A. S.; Pathak, P.; Meziani, M. J.; Harruff, B. A.; Wang, X.; Wang, H.; Luo, P. G.; Yang, H.; Kose, M. E.; Chen, B.; Veca, L. M.; Xie, S.-Y., Quantum-Sized Carbon Dots for Bright and Colorful Photoluminescence. *Journal of the American Chemical Society* **2006,** *128* (24), 7756-7757.
49. Son, J. S.; Park, K.; Kwon, S. G.; Yang, J.; Choi, M. K.; Kim, J.; Yu, J. H.; Joo, J.; Hyeon, T., Dimension-Controlled Synthesis of CdS Nanocrystals: From 0D Quantum Dots to 2D Nanoplates. *Small* **2012,** *8* (15), 2394-2402.
50. Zhang, Z. Y.; Jin, C. H.; Liang, X. L.; Chen, Q.; Peng, L. M., Current-voltage characteristics and parameter retrieval of semiconducting nanowires. *Applied Physics Letters* **2006,** *88* (7), 073102.
51. Spanhel, L.; Haase, M.; Weller, H.; Henglein, A., Photochemistry of colloidal semiconductors. 20. Surface modification and stability of strong luminescing CdS particles. *Journal of the American Chemical Society* **1987,** *109* (19), 5649-5655.
52. Saunders, A. E.; Ghezelbash, A.; Sood, P.; Korgel, B. A., Synthesis of High Aspect Ratio Quantum-Size CdS Nanorods and Their Surface-Dependent Photoluminescence. *Langmuir* **2008,** *24* (16), 9043-9049.
53. Conde, J.; Mejia, I.; Aguirre-Tostado, F. S.; Young, C.; Quevedo-Lopez, M. A., Design considerations for II–VI multi-gate transistors: the case of cadmium sulfide. *Semiconductor Science and Technology* **2014,** *29* (4), 045006.
54. Qu, L.; Peng, X., Control of Photoluminescence Properties of CdSe Nanocrystals in Growth. *Journal of the American Chemical Society* **2002,** *124* (9), 2049-2055.
55. Li, L. S.; Pradhan, N.; Wang, Y.; Peng, X., High Quality ZnSe and ZnS Nanocrystals Formed by Activating Zinc Carboxylate Precursors. *Nano Letters* **2004,** *4* (11), 2261-2264.
56. Ropagnol, X.; Morandotti, R.; Ozaki, T.; Reid, M., Toward High-Power Terahertz Emitters Using Large Aperture ZnSe Photoconductive Antennas. *IEEE Photonics Journal* **2011,** *3* (2), 174-186.
57. Venkatachalam, S.; Jeyachandran, Y. L.; Sureshkumar, P.; Dhayalraj, A.; Mangalaraj, D.; Narayandass, S. K.; Velumani, S., Characterization of vacuum-evaporated ZnSe thin films. *Materials Characterization* **2007,** *58* (8), 794-799.
58. Lee, J.; Sundar, V. C.; Heine, J. R.; Bawendi, M. G.; Jensen, K. F., Full Color Emission from II–VI Semiconductor Quantum Dot–Polymer Composites. *Advanced Materials* **2000,** *12* (15), 1102-1105.

Chapter 4

Charge Carrier Dynamics in Indium Selenide

4.1 Introduction

Confinement of charge carriers, i.e., electrons and holes on a two-dimensional (2D) plane, gives rise to very interesting optical and electronic properties.[1-3] After the discovery of graphene, the theoretical and experimental efforts to search for other 2D materials have rapidly increased. Optoelectronic properties of 2D layered materials can be effectively tuned as per the thickness of materials, i.e., the number of layers of 2D materials. Different electronic and optoelectronic properties of these 2D materials are dependent on the number of monolayers stacked together and, hence, are strikingly different from their bulk counterpart. Indium selenide (InSe) is an III-VI layered semiconductor.[4, 5] InSe has hexagonal lattice in the 2D plane with Se-In-In-Se in-plane covalent bonding and van der Waals (vdW) interaction across planes.

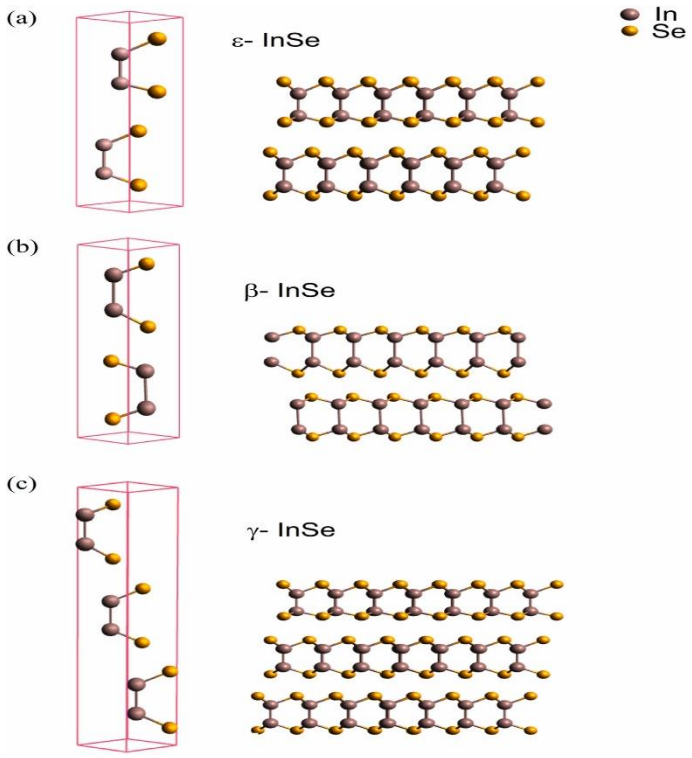

Figure 1. *Crystal structure of common polytypes of InSe: unit cell (left) and side view (right) a) ε-InSe b) β-InSe and c) γ-InSe. Reprinted with permission from ref.* [6] *Copyright (2020), Elsevier.*

InSe can exist in different polytypes, such as β, γ, and ε (Figure 1).[5-7] Since InSe has the appropriate band gap required for photovoltaic cells, it is a promising material in the field of photovoltaic as a light absorbing layer.[8] Tunable bandgaps over the entire visible range, high carrier mobility at room temperature, high on-off ratio, large photo-responsivity, and anisotropic and nonlinear optical properties are some of the important features of InSe, which are discovered in recent times.[4, 5, 7, 9-14] Photodetectors based on InSe have emerged as promising devices.[15] InSe is also an important semiconductor from a potential thermoelectric material point of view as it shows low intrinsic thermal conductivity at room temperature.[16, 17] Several class III-VI semiconductors, including InSe, are under intense experimentations for their possibility to be used as an emitter and detector even in the THz frequency range.[18-20] Overall, InSe has been showing excellent promise for different electronic and optoelectronic device applications.

Although there is no direct report of the TRTS study of the β-phase of bulk InSe at room temperature in the literature, the charge carrier dynamics of InSe in different morphologies and phases have been investigated using different spectroscopic techniques in the last few years. Siebbeles and co-workers reported a study on ultrathin InSe nanosheets using the optical pump THz probe (OPTP) spectroscopy.[21] They reported the carrier mobility measured by this non-contact method as high as 20 ± 2 cm^2/Vs at an excitation photon density of 10^{13} cm^{-2}. They have also reported the carrier quantum yield and exciton formation at low and high excitation photon densities. Weiss and co-workers studied bulk InSe using transient reflectivity spectroscopy. The authors inferred that the hot carrier cooling occurs through phonon scattering, and the observed effect is similar to lead-iodide perovskites.[22] They estimated surface recombination velocity (SRV) and ambipolar diffusion coefficient for bulk InSe. Dong Sun and co-workers studied In-rich multilayer InSe (~12 layers) using OPTP spectroscopy and they found that charge carrier dynamics in InSe-multilayer is insensitive to carrier density and pump photon wavelength, but it is very sensitive to temperature variations.[23] There are several other ultrafast spectroscopic studies on InSe that contribute significantly in understanding the carrier dynamics and relaxations in InSe.[24-27]

Here, we studied ultrafast carrier dynamics of bulk β-InSe. Time-resolved THz spectroscopy (TRTS) in reflection geometry was employed in studying photoexcited properties of Bulk InSe. TRTS is an excellent tool for accessing the dynamics of photocarriers in the excited state of semiconductor materials, as it measures the electronic properties in a non-contact

way.[28] A significant insight has been gained recently on 2D materials using TRTS techniques.[29, 30] We found that charge carrier dynamics in InSe is very sensitive to incident photon density, and it slows down with increasing photon density. This observation can be partially understood from the trap state saturation effect. Important semiconductor parameters such as carrier mobility and diffusion length were also determined from our TRTS data. These parameters are considerably higher in the case of the bulk β-InSe that we have studied.

4.2 Experimental Section

4.2.1 Sample preparation and characterization

Sample preparation

Indium selenide (InSe) sample was provided by Mr. Moinak Dutta from Prof. Kanishka Biswas's group at JNCASR, Bengaluru, India. Highly oriented InSe single crystals were prepared by dual zone vertical Bridgman technique. Stoichiometric quantities of high purity in (99.99%, Alfa Aesar) and Se (99.9999%, Alfa Aesar) (total weight of 10 g) were taken in a tapered quartz ampoule and sealed under high vacuum of 10-5 torr. The contents in the ampoule were heated up to 773 K in 12 hours, was kept at this temperature for 20 hours, then the temperature was increased to 1223 K in 8 hours. The reaction mixture was dwelling at this temperature (1223 K) for 44 hours and then cooled to 998 K in 24 hours. The melt was then passed through a temperature gradient from 998 K to 848 K at a speed of 1.5 mm/hr. Finally, the sample was slowly cooled to room temperature in 43 h.

Characterization

Room temperature X-ray diffraction (XRD) measurements of InSe were performed using Rigaku SmartLab SE diffractometer using Cu Kα (λ= 1.54059 Å) radiation. The XRD data of InSe was measured along the in-plane layer direction and cross-plane direction and can be indexed for the β-InSe phase (space group: $P6_3/mmc$). The compound, when measured along the cross-plane direction (|| to c-axis), shows highly intensified (0, 0, l) peaks, while the

intensity of the same peaks gets subsided when measured along the in-plane direction (⊥ to c-axis) as shown in Figure 2a. β-InSe phase has hexagonal crystal structure. [6]

The absorption spectrum of InSe was measured by diffuse reflection spectroscopy (DRS), and Tauc plot was used to obtain band gap (E_g) of InSe (Figure 2b). In DRS, The Kubelka-Munk Function, $F(R)$, is measured, which is given by the following equation 1.

$$F(R) = \frac{\alpha}{s} = \frac{(1-R)^2}{2R} \quad (1)$$

$$R = \frac{R_{Sample}}{R_{Ref-BaSO4}} \quad (2)$$

Here, α and s absorption and scattering coefficients respectively. R is the diffuse reflectance. Barium sulphate ($BaSO_4$) was used as reference in DRS with an absorption coefficient $\alpha \sim 0$ and R ~1. The Tauc plot equation is used to obtain bandgap (E_g) of semiconductor material.[31]

$$(\alpha h\nu)^n = A(h\nu - E_g) \quad (3)$$

Here, h is Plank constant, ν is frequency of optical light, n is integer (value of n depends on direct and indirect nature of bandgaps (as discussed below) and A is constant.

n=2 for direct bandgap semiconductor. Tauc plot equation in terms of the Kubelka-Munk Function, $F(R)$ can be written as,

$$(F(R)h\nu)^2 = A(h\nu - E_g) \quad (4)$$

$(F(R)h\nu)^2$ vs $h\nu$ is plotted and value of band gap (E_g) is the value of x axis at y = 0 from above equation. The bandgap is found to be 1.14 eV.

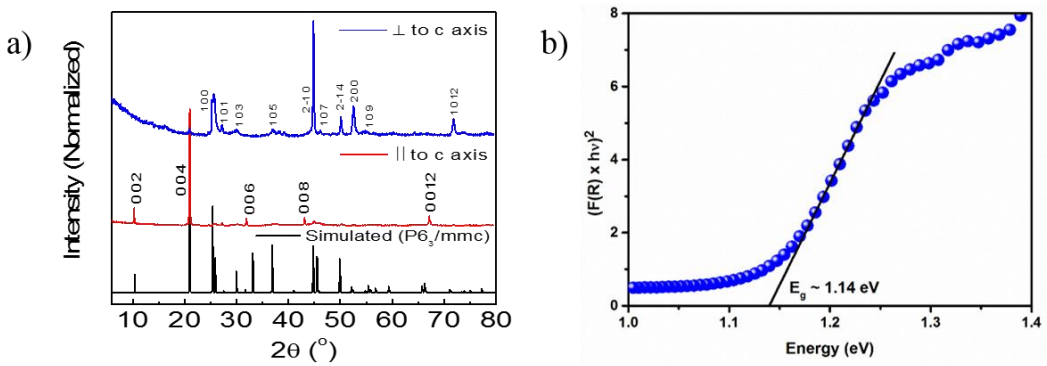

Figure 2. *a) PXRD collected of InSe perpendicular (blue) and parallel (red) to c axis of crystal. Reference XRD (black) of P6$_3$/mmc and b) Absorption of InSe used to estimate bandgap using Tauc plot.*

4.2.2 Reflection mode time-resolved THz spectroscopy setup

Our home-built TRTS setup is operated in normal incidence reflection geometry to record photoconductivity of InSe. Generally, TRTS is recorded in transmission geometry to study charge carrier dynamics and relaxation processes in various materials such as semiconductors, nanoparticles in solution and thin film forms, etc. If the sample to be studied is optically thick (high THz absorption cross-section), then THz transmission through the sample is extremely low. TRTS in reflection mode is done on such optically thick samples.

Our TRTS setup is based on ultrafast Ti:Sapphire laser system, which includes an ultrafast oscillator (Tsunami, Spectra Physics) and a regenerative amplifier from (Spitfire, Spectra-Physics). Output of the amplifier is near infrared femtosecond pulses (NIR) with a central wavelength of 800 nm, a repetition rate of 1 kHz, the pulse width of around 35 fs, and the total output power is ~4 mW. Half of the total power is utilised for the generation and detection of THz radiations and the remaining half power is used to pump an optical parametric amplifier [32].[32] We used air photonics-based THz generation and detection methods. The main advantage of air photonics-based methods is the capability to generate and detect ultra-broadband THz radiation up to 20 THz (even higher under certain conditions). In short, THz pulses are generated by focusing amplified laser pulses of 800 nm and its second harmonic (400 nm), which creates air plasma in dry air (less than 2% relative humidity) under continuously purging nitrogen (N_2) gas in a closed chamber. This air plasma is capable of producing broad spectra of electromagnetic (EM) radiation along with broadband THz radiations. THz radiations are filtered from the rest of the EM radiations by

using high resistivity silicon filter. THz radiations are detected using Air biased Coherent Detection (ABCD) techniques. The principle of ABCD method is exactly the reverse of the generation method, where a gate pulse of 800 nm interacts with the THz electric field in the nonlinear medium of a weak plasma to produce the second harmonic (400 nm) of the gate beam. The intensity of the second harmonic is proportional to the THz electric field. Air plasma generated THz pulses are detected by scanning the gate beam (~35 fs) over the entire THz waveform (~1-2 ps). The temporal overlap of the THz and gate pulses is varied using a mechanical stage. is The detected second-harmonic signal as the function of time-delay is the cross-correlation between the THz pulse and the optical gate pulse, hence maps out the entire THz waveform in time-domain. The details of the experimental setup are discussed in Chapter 2.

In reflection mode TRTS, a sample is photoexcited using optical pulse (the pump pulse) and probed using THz pulses. THz probe pulses are reflected from pumped and unpumped parts of samples and subsequently detected by ABCD method discussed above. Another mechanical delay stage provides the required time delay between the optical pump and THz probe pulses. In this work, the bulk InSe sample is photoexcited with a pump of wavelength of 800 nm i.e., energy of 1.55 eV. Since the direct electronic bandgap of InSe is close to 1.14 eV,[33] electrons are excited to the conduction band due to photoexcitation. Exciton binding energy of InSe is less than the thermal energy at the room temperature (~25 meV).[34-36] Hence, free electrons and holes are expected to be the dominant photoexcited species present in photoexcited InSe. Once the electrons and holes are photoexcited, their relaxation and recombination processes are probed by THz pulses arriving after the pump pulse. The polarisation of the optical pump and THz probe beams is parallel, and both beams are horizontally polarised. The polarisation of the pump and probe is perpendicular to the c-axis. (perpendicular to pressing direction). It should be noted here that the direction of sample pressing is chosen along the c-axis. Hence, we are measuring the photoconductivity of InSe in perpendicular to the c-axis, i.e. perpendicular to the pressing direction.

In reflection mode TRTS, transient photoconductivity ($\Delta\sigma$) is measured by collecting pump-induced change in the THz electric field $\Delta R(t)$ reflected from the sample,

$$\Delta R(t) = R_{on} - R_{off} \qquad (5)$$

R_{on} and R_{off} are the THz electric field reflected from the photoexcited (pump-on) and non-photoexcited (pump-off) samples, respectively. To minimize the effect of laser-pulse fluctuations, we used a double lock-in technique to collect the pump-induced change in the reflected electric field (ΔR) and the reflected electric field off the un-pumped sample (R_{off}) simultaneously. The differential transient reflectance ($\Delta R/R_{off}$) is directly used to obtain photoconductivity (Δσ) of InSe, which will be discussed further.

4.3 Results and Discussion

4.3.1 THz Time-domain Spectroscopy (THz-TDS) in Reflection Geometry

First, we measured steady-state absorption of InSe using time-domain THz spectroscopy in normal reflection geometry to observe the presence of any absorption peaks in the broadband THz frequency range (up to 8 THz). Figure 3a shows a time-domain electric field of THz pulse signals reflected from the reference (high resistivity silicon wafer) and the sample (InSe disk of 1 cm diameter and 1.4 mm thickness). The frequency dependent complex refractive indices of InSe were determined from the reflected THz signals (reference and sample) using the Fresnel equation for normal mode reflection (discussed in Chapter 2). It important to note that both the change in amplitude and phase between the reflected THz fields off the sample and the reference are detected, which enables us to determine both the absorption coefficient and the refractive index of the sample without any Kramers-Kronig analysis. In the absorption spectrum of the InSe, distinct peaks are observed, which are due to the THz absorption of the IR-active phonon modes. Low energy phonon modes are responsible for low thermal conductivity in many semiconductors and need to be understood throughly.[37, 38] We observed the strong absorption features at ~ 5.5 THz in the THz absorption spectrum of InSe (Figure 3b).

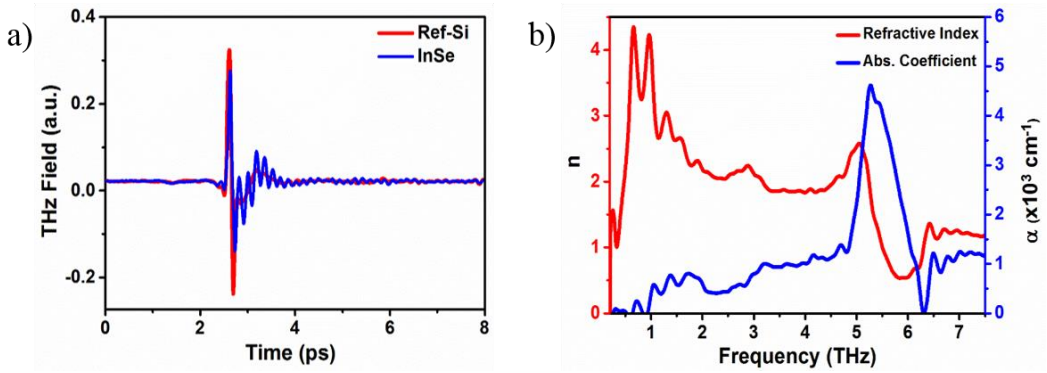

Figure 3. *a) Time-domain THz signals reflected from InSe (sample) and reference (silicon) and b) Frequency-dependent refractive index and absorption coefficient of InSe.*

4.3.2 Time-resolved THz spectroscopy (TRTS) in Reflection Geometry

Time-resolved THz spectroscopy (TRTS), also referred to as optical-pump and THz-probe spectroscopy (OPTP), is applied on a 1.4 mm thick bulk InSe. TRTS was performed in reflection geometry in normal-incidence mode at room temperature. The THz setup was continuously purged with dry nitrogen gas to avoid THz absorption by water in moist ambient air. In the TRTS study of InSe, the sample was photoexcited above the bandgap with an optical pulse of ~50 fs and central wavelength of 800 nm (i.e., equivalent photon energy of 1.55 eV). The bandgap of InSe was found to be 1.15 eV. First, THz signal reflected from the surface of an unpumped sample is collected. Further, sample is pumped with the optical pulse of 800 nm with specific fluence and the magnitude of the maximum reflected THz signal is monitored as a function of pump-probe delay time (t_p). Using the double lock-in technique with reference frequencies 333 Hz and 500 Hz, the photoinduced change in reflectance (ΔR) and unpumped reflectance ($R_{0/off}$) were simultaneously measured as pump-probe delay (t_p) was varied from -10 ps to 1600 ps. In Figure 4a, the time evolution of differential transient reflectance, $\frac{\Delta R}{R_0}$ have been shown with photoexcitation fluence from 45.6 μJ/cm^2 to 156.9 μJ/cm^2. Measured differential reflectance of InSe sample is under linear region for experimental fluences, as shown in Figure 4b.

Fluences can be converted to incident photon density, N_{ph} using the following equation.

$$N_{ph} = \phi\alpha = \frac{f_l\,(1-R)}{h\upsilon\delta} \qquad (6)$$

Here, N_{ph} is incident photon density, f_l is fluence, R is the reflectance at pump wavelength 800 nm, $h\upsilon$ is incident photon energy, δ is the penetration depth at the pump wavelength, and δ is equal to 10 μm taken from the literature.[23, 36, 39] Further, charge carrier density (N_0) is calculated from incident photon density (N_{ph}) assuming each photon creates two photoexcited charge carriers, an electron and a hole for a semiconductor with low exciton binding energy ($E_b < kT$). Photon density used for this experiment vary from 1.5×10^{17} to 5.2×10^{17} cm^{-3}. The photoinduced change in the conductivity (Δσ) is obtained using the following equation,[40]

$$1 + \frac{\Delta E(t_p)}{E_0(t_p)} = \frac{\left(1 - \tilde{n} - z_0 d \Delta\tilde{\sigma}(t_p)\right)}{\left(1 + \tilde{n} + z_0 d \Delta\tilde{\sigma}(t_p)\right)} \frac{(1+\tilde{n})}{(1-\tilde{n})} \tag{7}$$

$\tilde{n}$ is the frequency-dependent complex refractive index of non-photoexcited InSe. Frequency-dependent complex refractive index is obtained by solving Fresnel equation for reflection in normal incidence mode. For frequency-averaged THz study, we have taken low-frequency (around 1 THz) value real refractive index, n. z_0 is free-space impedance, and its value equals to 377 Ω, d is the thickness of the photoexcited layer, and in this work, it is obtained from the absorption coefficient (α) of InSe using relation $d = 1/\alpha$. The above equation 7 of photoconductivity can be approximately written in the following way when differential reflectivity is smaller than 1, i.e., $\frac{\Delta R(t_p)}{R_0}$"1.

$$\Delta\sigma(t_p) = \frac{(n^2-1)}{2z_0 d} \frac{\Delta R(t_p)}{R_{off}(t_p)} \tag{8}$$

$$\frac{\Delta R}{R_{off}} = \frac{\Delta E}{E_{0ff}} = \frac{E_{on} - E_{off}}{E_{off}} \tag{9}$$

Here, thin film approximation is used to account for the thickness of the photoexcited layer smaller than the smallest THz wavelength interacting with the sample (here note that wavelength of 1 THz frequency corresponds to 300 μm).

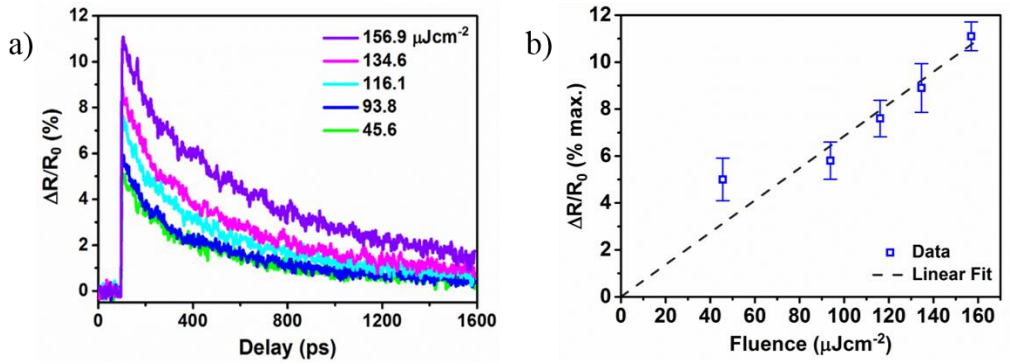

Figure 4. *a) Pump-induced differential reflectance at various excitation fluence and b) Maximum of each differential reflectance variation with fluence and its fit to linear equation (adj. R^2~0.98).*

4.3.3 Charge carrier dynamics of InSe

The photoinduced change in conductivity depends on the product of charge carrier density and the mobility ($\Delta\sigma(t_p) \sim N_0 * \mu_{eff}$). Here, we assume that the effective mobility of the photoinduced charge carriers remains constant throughout the entire pump-probe delay for which we have collected our data. Hence, the temporal evolution of the differential transient reflectance shown in Figure 4a is the measure of the temporal evolution of the carrier density up to ~1600 ps after photoexcitation. A decrease in differential transient reflectance represents the recombination and trapping of charge carriers after photoexcitation, hence a decrease in carrier density. To understand fluence-dependent response of photoexcited InSe, differential transient reflectance is normalised to its maximum value, as shown in Figure 5a. Initial rise in differential transient reflectance represents the generation of charge carriers after absorption of pump pulse of 800 nm wavelength. This process takes place in a sub-10ps timescale due to moderated excitonic binding energy. In most traditional bulk inorganic semiconductors such as GaAs, CdSe, and Si, buildup of photoexcited charge carries occurs in a faster timescale (> 5 ps) due to low excitonic energy (less than room temperature thermal energy of about 25 meV). Decay of the differential transient reflectance, which is dependent on excitation fluence, represents the evolution of photoexcited charges after excitation. Decay dynamics has information of recombination processes of photoexcited charge carriers of InSe. Interestingly, in the case of InSe, charge carrier dynamics seems to slow down with an increase of the excitation fluence (Figure 5a). We have used flueces from 45.6 to 156.9

μJ/cm^2 to photoexcite bulk InSe. Average radii of pump and probe beams at the sample were 1.7 mm and 0.4 mm, respectively, as measured by knife-edge method.

a) Photoinduced THz transients, their multiexponential fitting and recombination processes

To understand the recombination processes involved, multiexponential function convoluted Gaussian (equation 10) was used to fit normalised THz reflectance transients (of InSe.

$$y(t) = G(t - t_0) \otimes \frac{\sum_i^n a_i \, exp(t - t_0)}{t_i} \tag{10}$$

Here, $y(t)$ represents normalized differential reflectance and t_0 is the time zero, and t_i is the time constant for ith process, $G(t - t_0)$ represents the instrument response function (IRF), which is the cross-correlation function between the optical pump and the THz probe. The IRF for all TRTS experiments presented in this work is ~300 fs. Fluence-dependent normalized differential reflectance transients were fitted reasonably well on including three exponentials (Figure 5b). The fitted parameters, time constants (t_i) and their coefficients (a_i), have been given in Table 1. The average time, $< t >$ for each fluence-dependent transient, was calculated using the following relation.

$$< t >= \sum_i f_i t_i \tag{11}$$

$$f_i = \frac{a_i t_i}{\sum_i a_i t_i} \tag{12}$$

Here, f_i is contribution of i^{th} term or process towards the overall decay process. Smallest time constants i.e., fastest time t_1 obtained are in the range of 96 ps to 107 ps. These time constants remain almost independent of fluence and hence photo excited carrier density. Both intermediate time constant, t_2 and the slowest time constant t_3 are weakly dependent on fluence. Intermediate time constant (t_2) decreases with the increase in fluence, whereas the slowest time constant becomes faster as the fluence increases. Time constans (from the fastest

to the slowest and average time) are plotted against the carrier density as shown in Figures 6a and 6b.

It is important to have a clear understanding of the fluence dependence of charge carrier dynamics because it provides direct evidence of photophysical properties in semiconductors. Based on time constants obtained from fitting fluence-dependent THz transients, one can get a qualitative understanding of the physical processes involved in the recombination of photoexcited charge carriers. Since the fastest time constants are independent of fluence, we assigned this timescale to the process of filling available defect states. This process should have a monomolecular dependence on both the carrier density and the trap density. Intermediate timescale (358 to 537 ps at different fluence) could possibly be due to the saturation of trap states, and hence due to the complete filling of trap states, there is an increase in intermediate time component with the increase in fluence at photoexcited carrier density of about 10^{17} cm^{-3}.[41] Trap states involved in this process might be surface states and hence, the density of the surface states might be different than that of the mid-gap (bulk) defect states and surface states are getting filled slowly upon photoexcitation.[41] The fasted timescale is assigned to the filling of bulk states, whereas the intermediate timescale is assigned to the filling of surface states. The slowest timescale is assigned to the process of bimolecular electron-hole recombination as its contribution (amplitude) increases at the highest fluence as compared to the lowest fluence. The average time calculated from equation 11 shows roughly a decreasing trend with an increase in fluence. Charge carrier dynamics in InSe exists for more than 1 ns time. Long lifetime after photoexcitation in semiconductors is an important condition for light-harvesting applications such as solar cells. The average carrier lifetimes are in the range of 1-1.5 ns, which are long enough for charge carriers to be extracted for specific applications. But if the timescale is longer due to the trapping of photoexcited charges in trap states, then the desired application cannot be achieved efficiently, especially in optoelectronic applications.

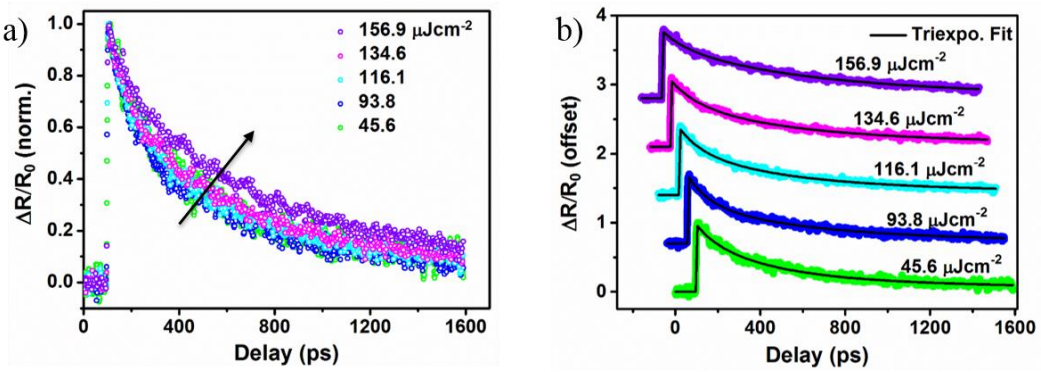

Figure 5. *a) Normalised THz transients and b) Triexponential fitting of THz transients.*

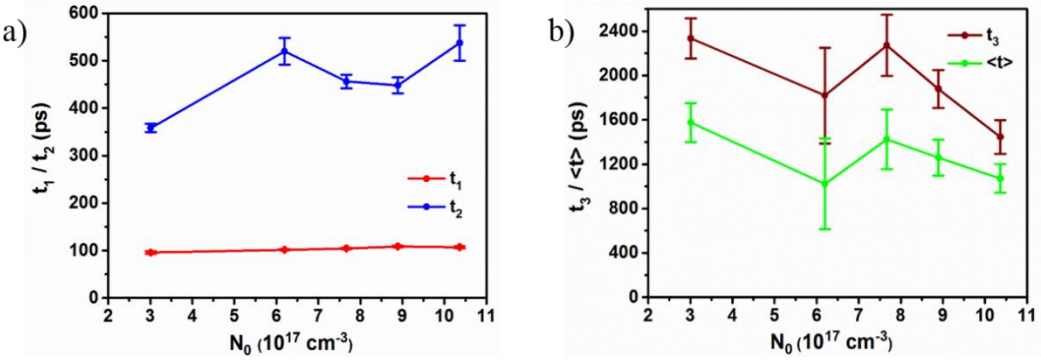

Figure 6. *Time constants obtained from fitting THz transients of InSe a)* t_1 *and* t_2 *(with one standard deviation) and b)* t_3 *and* $< t >$ *(with one standard deviation).*

Table 1. *Time constants obtained by triexponential fitting of photoinduced THz transients. (Errors/one standard deviations are given in parentheses.)*

Fluence ($\mu J/cm^2$)	t_1 (ps)	a_1	t_2 (ps)	a_2	t_3 (ps)	a_3	$< t >$ (ps)
45.6	96 (3)	0.201 (0.009)	358.5 (9.0)	0.608 (0.004)	2333.6 (180)	0.166 (0.009)	1575.5 (174.4)
93.8	101.7 (1.0)	0.398 (0.005)	519.8 (28.2)	0.476 (0.029)	1819.6 (431)	0.111 (0.034)	1022.0 (409.7)
116.1	104.7 (1.4)	0.307 (0.006)	456.2 (14.7)	0.526 (0.010)	2271.4 (276)	0.143 (0.016)	1423.9 (266.7)
134.6	108.9 (1.8)	0.268 (0.007)	447.9 (16.9)	0.513 (0.013)	1878.4 (170)	0.189 (0.019)	1259.6 (160.0)
156.9	107.4 (2.2)	0.196 (0.006)	537.3 (37.1)	0.486 (0.051)	1445 (151)	0.296 (0.057)	1071.7 (130.2)

Why might trap states be the surface trap states?

As per data and discussion in previous sections, THz transients of bulk (β-) InSe are slowing down with increasing fluence. We extracted time components/constants to understand this behaviour by fitting multiexponential functions to fluence-dependent THz transients. We found that the time component (t_2) is roughly varying from about 350 ps to 540 ps with increasing fluence, and this time constant is assigned to surface state saturation/filling. This kind of observation in slowing down of time constant with increasing excitation condition is found in a few other TRTS studies reports, and few reports showed the magnitude of time components of the same order as found in our study. Cunlin Zhang and co-workers investigated semi-insulating GaAs by (femtosecond) optical-pump and THz-probe with various optical pump powers, and they found that carrier decay slows down from 360 to 500 ps on increasing power from 7 to 47 mW.[41] Authors have assigned this trend in carrier decays to surface state filling, and they have suspected this to restrict direct carrier recombination in semi-insulating GaAs. Here, it is interesting to note that the rough estimation of photocarrier density in our study and this study (Cunlin Zhang and co-workers) is of the same order (n_{exc}~10^{17} cm^{-3}). Before this work, M. B. Johnston and co-workers studied passivated and etched semi-insulating GaAs, which affects its the carrier lifetime.[42] In the surface passivated sample, carrier lifetime is slower (389 ps) than the etched sample (192 ps); this is very similar surface states filling process for a passivated sample where the availability of surface states is lower as compared to the etched sample which is resulting in their longer lifetime (and photoconductivity). T. S. Sosnowski and co-workers also observed slowing down electron dynamics with increasing fluence in low-temperature-grown GaAs.[43] This observation, they have explained, is a consequence of trap state saturation. In the proposed rate equation, free-electron densities are sufficiently more prominent than the available surface trap density. The rate of change of electron density becomes independent of electron density and solely depends on available trap density, and filling this trap is a dominant path. Michael B. Johnston and co-workers have observed slowing down of carrier lifetime from 130 to 210 ps that is due to trap saturation in bulk GaN studied using OPTP, and they found significant enhancement in carrier lifetime for GaN NWs which due high-quality and low carrier trap density.[44]

Trap saturation or surface state filling is a process also observed in semiconductor nanowires (NWs) with time component in a few tens of picoseconds when studied from time-resolved

spectroscopic techniques such as Optical-pump THz-Probe (OPTP), differential absorption spectroscopy etc. A. Othonos and co-workers studied Tin Oxide (SnO_2) nanowires; authors have associated fastest component to (photo-)electron transition from conduction band to shallow traps which is slowing down with fluence.[45] In GaAs NWs studied using OPTP by Laura Herz and co-workers, surface trap saturation has been observed, and surface trap density estimated at ~10^{17} cm^{-3}.[46] In another work by Michael B. Johnston and co-workers on four different samples of core-(high-bandgap) shell GaAs NWs, all showed a rise in carrier lifetime with excitation fluence (5 to 20 ps); authors have suggested a reason for this that the existence of trap states which start to saturate at higher photocarrier density. [47]

Trap states affect carrier lifetime, and if their density is smaller than photocarrier density, they might begin to saturate with photocarrier density increases in semiconductors. These (saturating) trap states are found to be surface trap states as per many earlier reports as discussed above.

b) Mobility and diffusion length

One major importance of the TRTS technique is to be able to measure parameters such as charge carrier mobility and diffusion lengths after photoexcitation in a non-contact way.[48, 49] Carrier mobility is calculated from photoconductivity and peak carrier density. Diffusion length is calculated using average carrier time and mobility. Equations are given below to calculate mobility and diffusion length,

$$\phi\mu = \frac{\Delta\sigma}{qN_0} \tag{13}$$

$$L_D = \sqrt{\frac{< t > \mu k_B T}{q}} \tag{14}$$

Mobility calculated through TRTS is the lower limit since we have assumed that there is no scattering loss of the pump photons, and each absorbed photon produces a pair of carriers. In equation 13, ϕ is the photon-to-charge-carrier pair ratio, which is between 0 and 1 under the linear excitation regime. $\phi\mu$ is called the effective mobility. Carrier mobility and diffusion length are expected not to vary much with pump-probe delay and should remain almost the

same under the linear regime of pump excitation conditions. Figures 7a and 7b show the variation of mobility and diffusion length with respect to carrier concentration, respectively. Mobility and diffusion lengths of InSe are calculated from TRTS, which are around 20.6 $cm^2V^{-1}s^{-1}$ and 289.8 nm, respectively, at photocarrier concentration of 10^{17} cm^{-3}. Mobilities calculated here are expected to have more contribution from the electrons as the effective mass (m^*) is lower for the electron ($m_e^* = 0.14m_0$) as compared to the effective mass of the hole (which is at least five times that of the electron mass, $m_h^* = 0.73m_0$) InSe .[5, 7, 50, 51] Mobilities of undoped InSe are reported from earlier studies at intrinsic carrier concentrations (measured by contact method) of the order of 10^{13} to 10^{14} cm^{-3} as shown in Table 3. Carrier transport (carrier mobility) is severely impacted by the density of defects in semiconductors.[52-54]

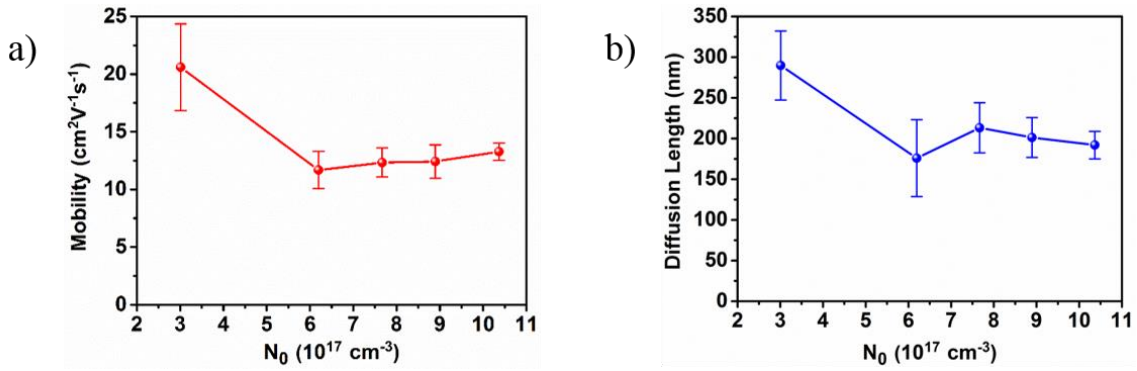

Figure 7. *a) Mobility and b) Diffusion length as a function of photon density (carrier density).*

Table 2. *Parameters obtained from TRTS photoconductivity measurements: mobility and diffusion length. (Errors are given in parentheses.)*

Fluence ($\mu J/cm^2$)	N_{ph} ($10^{17}cm^{-3}$)	$\Delta R/R_0$ (max.)	Photoconductivity (S/m)	Mobility (cm^2/Vs)	$< t >$ (ps)	Diffusion length (nm)
45.6	1.5	0.050 (0.009)	99.2 (18.1)	20.6 (3.7)	1575.5 (174.4)	289.8 (42.4)
93.8	3.1	0.058 (0.008)	115.9 (15.9)	11.7 (1.6)	1022.0 (409.7)	175.9 (47.3)
116.1	3.8	0.076 (0.008)	151.3 (15.4)	12.3 (1.3)	1424.0 (266.7)	213.2 (30.8)
134.6	4.4	0.089 (0.010)	176.8 (20.6)	12.4 (1.4)	1259.6 (160)	201.3 (24.5)
156.9	5.2	0.111	220.3	13.3	1071.7	191.9

		(0.006)	(12.2)	(0.7)	(130.2)	(16.9)

c) Comparison between Intrinsic conductivity (four-probe method) and photoconductivity (TRTS)

Intrinsic conductivity is measured through a four-probe method using the ULVAC-RIKO ZEM3 instrument is 0.08 S/cm (unpublished work). Photoconductivity is around 0.99 S/cm at the lowest photocarrier concentration at 3×10^{17} cm^{-3}. The intrinsic carrier concentration of InSe is of the order of 10^{13} to 10^{14} cm^{-3}.[17, 55, 56] Low value of direct (intrinsic) conductivity is due to low intrinsic carrier concentration of InSe at room temperature, as shown in Table 3. Despite of possessing low intrinsic lattice thermal conductivity, the low electronic conductivity may be detrimental for InSe as a thermoelectric material as the thermoelectric efficiency depends on both the thermal and electronic conductivities. Hence, the electronic conductivity must be increased by increasing carrier concentration (for example, by doping) or any other strategies for potential thermoelectric applications of InSe.

Table 3. *Carrier concentration (undoped), mobility and conductivity (measured by Hall measurement) of InSe. PA, PE: parallel and perpendicular to the pressing direction, respectively. (Layers get stacked along pressing direction. Hence, the pressing direction is along the c-axis.)*

Carrier Concentration (cm^{-3})	Mobility ($cm^2V^{-1}s^{-1}$)	Conductivity (Scm^{-1})	Ref.
2.57×10^{14} (PE)	16.8	6×10^{-4}	[56]
1.15×10^{14} (PA)	30.6	6×10^{-4}	[56]
3.2×10^{13} (PA)	1.9	-	[17]
5.1×10^{13} (PE)	54.4	1.3×10^{-3}	[55]
5.1×10^{13} (PA)	22.7	$< 1.3 \times 10^{-3}$	[55]

At higher temperatures, InSe could be a promising thermoelectric material because the figure of merit increases [17, 55, 56] with temperature if systematic efforts are made to increase

electronic conductivity. Also, it could be a promising optoelectronic material, provided controlled defect engineering is carried out for bulk thin film applications.

4.4 Conclusions

In this chapter, we performed time-domain and time-resolved THz spectroscopy experiments in reflection mode on bulk β-InSe. THz absorption spectra show several absorption peaks that might be responsible for low thermal conductivity in this material. Complex refractive index (or, in general, complex dielectric function) in the THz frequency range is an important dielectric property for any semiconductor for its potential applications, especially in electronics and devices, and obtaining the complex dielectric function is the main advantage of such advanced ultrafast THz spectroscopic technique. We have measured the complex refractive index for InSe through reflection mode THz-TDS and have observed several absorption peaks in low frequencies lie in the THz range that could be responsible for its low thermal conductivity, and this work is being studied further in this direction. The time-resolved THz study unravels the charge carrier dynamics in photoexcited InSe, which shows slowing down dynamics upon increasing photoexcitation density and help to identify photocarrier response under experimental condition and it also helps to estimate the density of defects in InSe, which is equal to less than the photocarrier density under experimental conditions. Photoconductivity measured through TRTS is used to provide a non-contact estimation of the electronic contribution of conductivity. Reasonable mobility and diffusion length are found in InSe despite the reasonable density of defects, which can be a crucial parameter for any material for its integration into an actual device. All these studies might be essential from a potential optoelectronic, thermoelectric applications perspective. Being a layered material, layer-dependent, thickness-dependent ultrafast investigation on InSe will be important and interesting from its potential wide-spread applications in various fields.

4.5 References

1. Wang, Q. H.; Kalantar-Zadeh, K.; Kis, A.; Coleman, J. N.; Strano, M. S., Electronics and optoelectronics of two-dimensional transition metal dichalcogenides. *Nature Nanotechnology* **2012,** *7* (11), 699-712.
2. Mak, K. F.; Shan, J., Photonics and optoelectronics of 2D semiconductor transition metal dichalcogenides. *Nature Photonics* **2016,** *10* (4), 216-226.
3. Jariwala, D.; Sangwan, V. K.; Lauhon, L. J.; Marks, T. J.; Hersam, M. C., Emerging Device Applications for Semiconducting Two-Dimensional Transition Metal Dichalcogenides. *ACS Nano* **2014,** *8* (2), 1102-1120.
4. Dai, M.; Gao, C.; Nie, Q.; Wang, Q.-J.; Lin, Y.-F.; Chu, J.; Li, W., Properties, Synthesis, and Device Applications of 2D Layered InSe. *Advanced Materials Technologies* **2022,** *n/a* (n/a), 2200321.
5. Wan, W.; Guo, R.; Ge, Y.; Liu, Y., Carrier and phonon transport in 2D InSe and its Janus structures. *Journal of Physics: Condensed Matter* **2023,** *35* (13), 133001.
6. Grimaldi, I.; Gerace, T.; Pipita, M. M.; Perrotta, I. D.; Ciuchi, F.; Berger, H.; Papagno, M.; Castriota, M.; Pacilé, D., Structural investigation of InSe layered semiconductors. *Solid State Communications* **2020,** *311*, 113855.
7. Xu, K.; Yin, L.; Huang, Y.; Shifa, T. A.; Chu, J.; Wang, F.; Cheng, R.; Wang, Z.; He, J., Synthesis, properties and applications of 2D layered MIIIXVI (M = Ga, In; X = S, Se, Te) materials. *Nanoscale* **2016,** *8* (38), 16802-16818.
8. Rai, A.; Sangwan, V. K.; Gish, J. T.; Hersam, M. C.; Cahill, D. G., Anisotropic thermal conductivity of layered indium selenide. *Applied Physics Letters* **2021,** *118* (7), 073101.
9. Bandurin, D. A.; Tyurnina, A. V.; Yu, G. L.; Mishchenko, A.; Zólyomi, V.; Morozov, S. V.; Kumar, R. K.; Gorbachev, R. V.; Kudrynskyi, Z. R.; Pezzini, S.; Kovalyuk, Z. D.; Zeitler, U.; Novoselov, K. S.; Patanè, A.; Eaves, L.; Grigorieva, I. V.; Fal'ko, V. I.; Geim, A. K.; Cao, Y., High electron mobility, quantum Hall effect and anomalous optical response in atomically thin InSe. *Nature Nanotechnology* **2017,** *12* (3), 223-227.
10. Feng, W.; Zheng, W.; Cao, W.; Hu, P., Back gated multilayer InSe transistors with enhanced carrier mobilities via the suppression of carrier scattering from a dielectric interface. *Adv Mater* **2014,** *26* (38), 6587-93.
11. Chen, C.; Dong, N.; Huang, J.; Wang, Z.; Wang, J., Microscopic optical nonlinearities and transient carrier dynamics in indium selenide nanosheet. *Opt. Express* **2022,** *30* (11), 17967-17979.
12. Song, C.; Huang, S.; Wang, C.; Luo, J.; Yan, H., The optical properties of few-layer InSe. *Journal of Applied Physics* **2020,** *128* (6), 060901.
13. Gao, S.; Liu, L.; Wen, B.; Zhang, X., Monolayer InSe photodetector with strong anisotropy and surface-bound excitons. *Physical Chemistry Chemical Physics* **2021,** *23* (10), 6075-6083.
14. Autere, A.; Jussila, H.; Dai, Y.; Wang, Y.; Lipsanen, H.; Sun, Z., Nonlinear Optics with 2D Layered Materials. *Advanced Materials* **2018,** *30* (24), 1705963.
15. Tamalampudi, S. R.; Lu, Y.-Y.; U, R. K.; Sankar, R.; Liao, C.-D.; B, K. M.; Cheng, C.-H.; Chou, F. C.; Chen, Y.-T., High Performance and Bendable Few-Layered InSe Photodetectors with Broad Spectral Response. *Nano Letters* **2014,** *14* (5), 2800-2806.

16. Han, G.; Chen, Z.-G.; Drennan, J.; Zou, J., Indium Selenides: Structural Characteristics, Synthesis and Their Thermoelectric Performances. *Small* **2014,** *10* (14), 2747-2765.
17. Shi, H.; Wang, D.; Xiao, Y.; Zhao, L.-D., Dynamic carrier transports and low thermal conductivity in n-type layered InSe thermoelectrics. *Aggregate* **2021,** *2* (4), e92.
18. Mandal, K. C.; Kang, S. H.; Choi, M.; Chen, J.; Zhang, X. C.; Schleicher, J. M.; Schmuttenmaer, C. A.; Fernelius, N. C., III–VI Chalcogenide Semiconductor Crystals for Broadband Tunable THz Sources and Sensors. *IEEE Journal of Selected Topics in Quantum Electronics* **2008,** *14* (2), 284-288.
19. Liu, K.; Xu, J.; Zhang, X. C., GaSe crystals for broadband terahertz wave detection. *Applied Physics Letters* **2004,** *85* (6), 863-865.
20. Mandal, K. C.; Kang, S. H.; Choi, M. K., Layered Compound Semiconductor GaSe and GaTe Crystals for THz Applications. *MRS Online Proceedings Library (OPL)* **2006,** *969*, 0969-W03-15.
21. Lauth, J.; Kulkarni, A.; Spoor, F. C. M.; Renaud, N.; Grozema, F. C.; Houtepen, A. J.; Schins, J. M.; Kinge, S.; Siebbeles, L. D. A., Photogeneration and Mobility of Charge Carriers in Atomically Thin Colloidal InSe Nanosheets Probed by Ultrafast Terahertz Spectroscopy. *The Journal of Physical Chemistry Letters* **2016,** *7* (20), 4191-4196.
22. Zhong, C.; Sangwan, V. K.; Kang, J.; Luxa, J.; Sofer, Z.; Hersam, M. C.; Weiss, E. A., Hot Carrier and Surface Recombination Dynamics in Layered InSe Crystals. *The Journal of Physical Chemistry Letters* **2019,** *10* (3), 493-499.
23. Lu, W.; Yang, Z.; Hao, J.; Sun, D., Terahertz relaxation dynamics of a two-dimensional InSe multilayer. *Physical Review B* **2020,** *102* (1), 014314.
24. Li, Y.; Ye, J.; Yuan, K.; Zhai, G.; Li, T.; Ye, Y.; Wu, X.; Zhang, X., Photo-excited carrier relaxation dynamics in two-dimensional InSe flakes. *Nanotechnology* **2020,** *31* (9), 095713.
25. Wang, R.; Jiang, X.; Gao, S.; Zhao, J.; Zhang, F.; Huang, W.; Fan, T.; Liang, W.; Li, Z.; Huang, H.; Guo, Z.; Wang, H.; Zhang, Y.; Zhang, X.; Luo, Z.; Zhang, H., Unveiling the Stimulated Robust Carrier Lifetime of Surface-Bound Excitons and Their Photoresponse in InSe. *Advanced Materials Interfaces* **2019,** *6* (13), 1900171.
26. Chen, Z.; Giorgetti, C.; Sjakste, J.; Cabouat, R.; Véniard, V.; Zhang, Z.; Taleb-Ibrahimi, A.; Papalazarou, E.; Marsi, M.; Shukla, A.; Peretti, J.; Perfetti, L., Ultrafast electron dynamics reveal the high potential of InSe for hot-carrier optoelectronics. *Physical Review B* **2018,** *97* (24), 241201.
27. Yang, S.; Kelley, D. F., Transient Absorption Spectra and Dynamics of InSe Nanoparticles. *The Journal of Physical Chemistry B* **2006,** *110* (27), 13430-13435.
28. Ulbricht, R.; Hendry, E.; Shan, J.; Heinz, T. F.; Bonn, M., Carrier dynamics in semiconductors studied with time-resolved terahertz spectroscopy. *Reviews of Modern Physics* **2011,** *83* (2), 543-586.
29. Han, P.; Wang, X.; Zhang, Y., Time-Resolved Terahertz Spectroscopy Studies on 2D Van der Waals Materials. *Advanced Optical Materials* **2020,** *8* (3), 1900533.
30. Lu, J.; Liu, H., A critical review on the carrier dynamics in 2D layered materials investigated using THz spectroscopy. *Optics Communications* **2018,** *406*, 24-35.
31. Makuła, P.; Pacia, M.; Macyk, W., How To Correctly Determine the Band Gap Energy of Modified Semiconductor Photocatalysts Based on UV–Vis Spectra. *The Journal of Physical Chemistry Letters* **2018,** *9* (23), 6814-6817.

32. Ropagnol, X.; Morandotti, R.; Ozaki, T.; Reid, M., Toward High-Power Terahertz Emitters Using Large Aperture ZnSe Photoconductive Antennas. *IEEE Photonics Journal* **2011,** *3* (2), 174-186.
33. Boukhvalov, D. W.; Gürbulak, B.; Duman, S.; Wang, L.; Politano, A.; Caputi, L. S.; Chiarello, G.; Cupolillo, A., The Advent of Indium Selenide: Synthesis, Electronic Properties, Ambient Stability and Applications. *Nanomaterials* **2017,** *7* (11), 372.
34. Camassel, J.; Merle, P.; Mathieu, H.; Chevy, A., Excitonic absorption edge of indium selenide. *Physical Review B* **1978,** *17* (12), 4718-4725.
35. Merle, J. C.; Bartiromo, R.; Borsella, E.; Piacentini, M.; Savoia, A., Direct-gap excitons in InSe by modulated magneto-optics and photoconductivity. *Solid State Communications* **1978,** *28* (3), 251-255.
36. Gürbulak, B.; Şata, M.; Dogan, S.; Duman, S.; Ashkhasi, A.; Keskenler, E. F., Structural characterizations and optical properties of InSe and InSe:Ag semiconductors grown by Bridgman/Stockbarger technique. *Physica E: Low-dimensional Systems and Nanostructures* **2014,** *64*, 106-111.
37. Dutta, M.; Matteppanavar, S.; Prasad, M. V. D.; Pandey, J.; Warankar, A.; Mandal, P.; Soni, A.; Waghmare, U. V.; Biswas, K., Ultralow Thermal Conductivity in Chain-like TlSe Due to Inherent Tl+ Rattling. *Journal of the American Chemical Society* **2019,** *141* (51), 20293-20299.
38. Jana, M. K.; Pal, K.; Warankar, A.; Mandal, P.; Waghmare, U. V.; Biswas, K., Intrinsic Rattler-Induced Low Thermal Conductivity in Zintl Type TlInTe2. *Journal of the American Chemical Society* **2017,** *139* (12), 4350-4353.
39. Damon, R. W.; Redington, R. W., Electrical and Optical Properties of Indium Selenide. *Physical Review* **1954,** *96* (6), 1498-1500.
40. Cooke, D. G.; Krebs, F. C.; Jepsen, P. U., Direct Observation of Sub-100 fs Mobile Charge Generation in a Polymer-Fullerene Film. *Physical Review Letters* **2012,** *108* (5), 056603.
41. Shi, Y.; Zhou, Q.-l.; Zhang, C.; Jin, B., Ultrafast high-field carrier transport in GaAs measured by femtosecond pump-terahertz probe spectroscopy. *Applied Physics Letters* **2008,** *93* (12), 121115.
42. Lloyd-Hughes, J.; Merchant, S. K. E.; Fu, L.; Tan, H. H.; Jagadish, C.; Castro-Camus, E.; Johnston, M. B., Influence of surface passivation on ultrafast carrier dynamics and terahertz radiation generation in GaAs. *Applied Physics Letters* **2006,** *89* (23).
43. Sosnowski, T. S.; Norris, T. B.; Wang, H. H.; Grenier, P.; Whitaker, J. F.; Sung, C. Y., High-carrier-density electron dynamics in low-temperature-grown GaAs. *Applied Physics Letters* **1997,** *70* (24), 3245-3247.
44. Parkinson, P.; Dodson, C.; Joyce, H. J.; Bertness, K. A.; Sanford, N. A.; Herz, L. M.; Johnston, M. B., Noncontact Measurement of Charge Carrier Lifetime and Mobility in GaN Nanowires. *Nano Letters* **2012,** *12* (9), 4600-4604.
45. Othonos, A.; Zervos, M.; Tsokkou, D., Tin Oxide Nanowires: The Influence of Trap States on Ultrafast Carrier Relaxation. *Nanoscale Research Letters* **2009,** *4* (8), 828.
46. Parkinson, P.; Lloyd-Hughes, J.; Gao, Q.; Tan, H. H.; Jagadish, C.; Johnston, M. B.; Herz, L. M., Transient Terahertz Conductivity of GaAs Nanowires. *Nano Letters* **2007,** *7* (7), 2162-2165.
47. Parkinson, P.; Joyce, H. J.; Gao, Q.; Tan, H. H.; Zhang, X.; Zou, J.; Jagadish, C.; Herz, L. M.; Johnston, M. B., Carrier Lifetime and Mobility Enhancement in Nearly

Defect-Free Core−Shell Nanowires Measured Using Time-Resolved Terahertz Spectroscopy. *Nano Letters* **2009,** *9* (9), 3349-3353.

48. Mir, W. J.; Warankar, A.; Acharya, A.; Das, S.; Mandal, P.; Nag, A., Colloidal thallium halide nanocrystals with reasonable luminescence, carrier mobility and diffusion length. *Chemical Science* **2017,** *8* (6), 4602-4611.
49. Yettapu, G. R.; Talukdar, D.; Sarkar, S.; Swarnkar, A.; Nag, A.; Ghosh, P.; Mandal, P., Terahertz Conductivity within Colloidal CsPbBr3 Perovskite Nanocrystals: Remarkably High Carrier Mobilities and Large Diffusion Lengths. *Nano Letters* **2016,** *16* (8), 4838-4848.
50. Ferrer-Roca, C.; Segura, A.; Andrés, M. V.; Pellicer, J.; Muñoz, V., Investigation of nitrogen-related acceptor centers in indium selenide by means of photoluminescence: Determination of the hole effective mass. *Physical Review B* **1997,** *55* (11), 6981-6987.
51. Segura, A. Layered Indium Selenide under High Pressure: A Review *Crystals* [Online], **2018**.
52. Lordi, V.; Erhart, P.; Åberg, D., Charge carrier scattering by defects in semiconductors. *Physical Review B* **2010,** *81* (23), 235204.
53. Mao, J.; Liu, Z.; Zhou, J.; Zhu, H.; Zhang, Q.; Chen, G.; Ren, Z., Advances in thermoelectrics. *Advances in Physics* **2018,** *67* (2), 69-147.
54. YU, P.; Cardona, M., *Fundamentals of Semiconductors: Physics and Materials Properties*. Springer Berlin Heidelberg: **2010**.
55. Lee, K. H.; Oh, M.-W.; Kim, H.-S.; Shin, W. H.; Lee, K.; Lim, J.-H.; Kim, J.-i.; Kim, S.-i., Enhanced thermoelectric transport properties of n-type InSe due to the emergence of the flat band by Si doping. *Inorganic Chemistry Frontiers* **2019,** *6* (6), 1475-1481.
56. Hou, X.; Chen, S.; Du, Z.; Liu, X.; Cui, J., Improvement of the thermoelectric performance of InSe-based alloys doped with Sn. *RSC Advances* **2015,** *5* (124), 102856-102862.

Chapter 5

Charge Carrier Dynamics in Thallium Selenide

5.1 Introduction

Selenide-based semiconductors are promising in infrared optoelectronic and thermoelectric applications. InSe, GaSe, PbSe, and SnSe are a few important selenide-based semiconductors belonging to class III-VI and IV-VI due to their promising applications in the mentioned fields.[1, 2] PbSe and SnSe have emerged as benchmark materials for thermoelectric applications with high figure of merit values.[3-10] GaSe and InSe have shown promising results in optoelectronic applications,[11-13] nonlinear optics,[14, 15] THz optics,[16, 17] etc.

Thallium selenide (TlSe) is a class III-VI, indirect bandgap semiconductor with the bandgap in the near-infrared (NIR) range. It is low-dimensional semiconductor having chain-like Zintl structure.[18, 19] TlSe has not yet been studied from an optoelectronic point of view, unlike other members of the class III-VI semiconductors. In a recent study, Biswas and co-workers showed that thallium selenide has ultralow intrinsic lattice thermal conductivity (0.62−0.4 W/mK) in the temperature range of 295–525 K, which is crucial for achieving high thermoelectric efficiency.[20] TlSe is a mixvalent compound with Tl^{+} and Tl^{3+} cations occupying two inequivalent crystallographic sites, as shown in Figure 1b-c.

The electronic conductivity (σ) of an efficient thermoelectric material should be high without contributing towards the thermal conductivity. The electronic conductivity depends on the carrier properties (such as mobility and diffusion length) and their dynamics. On the other hand, the thermal conductivity depends on the phonon dynamics. Hence, it is immensely important to study the carrier dynamics, phonon dynamics, and the coupling between them in potential thermoelectric materials to identify the mechanism of decoupling the thermal conductivity and electronic conductivity. TRTS is the ideal technique for studying both charge carriers and the phonons at the same time. Also, studying charge carrier dynamics in TlSe can help to understand its applicability in various fields especially in optoelectronics and thermoelectrics. As of now, no ultrafast carrier dynamics study has been reported on TlSe.

In this work, we have employed time-domain and time-resolved THz spectroscopy to study the charge carrier dynamics in bulk TlSe single crystal. Photoconductivity measurement using non-contact time-resolved THz spectroscopy (TRTS) gives a quantitative estimation of electronic properties.

5.2 Experimental Section

5.2.1 Synthesis of TlSe and its characterisation

Thallium selenide semiconductor sample was provided by Mr. Moinak Dutta from Dr. Kanishka Biswas's group at JNCASR, Bengaluru, India. TlSe was synthesised using a modified Bridgman technique. Details of the synthesis procedure and characterisation is given elsewhere.[20]

Synthesis of TlSe

The modified Bridgman technique was used to prepare high-quality crystalline TlSe. The stoichiometric quantities of high-purity Tl (99.999 %) and Se (99.999 %) were taken in a quartz ampoule and sealed under a high vacuum of 10^{-5} torr. The ampoule was heated to 773 K in 6 hr and were kept at that temperature for 6 hr. For crystallisation, ampoule was further cooled to 673 K in 3 hr and was kept at that temperature for 20 hr and then cooled to room temperature in 6 hr to get the final product. The Spark Plasma Sintering was performed on the finely ground product obtained. The sample was placed in a 10 mm graphite die for the Sintering process. The die was heated to 250 ^{o}C in 5 minutes and kept at that temperature for 5 minutes, and then it cooled to room temperature in 10 minutes. This whole sintering process was performed under constant 3.9 kN pressure.

Characterization

UV-visible absorption spectra of Thallium Selenide (TlSe) pellet were recorded using a Shimadzu UV 3600 plus spectrophotometer in reflection mode as shown in Figure 1. Diffuse reflectance was measured with barium sulphate ($BaSO_4$) being used as the reference. Here we recorded diffuse reflectance, R, from the sample and reference. Diffuse reflectance (R) was used to obtain the Kubelka-Munk Function $F(R)$,

$$F(R) = \frac{\alpha}{s} = \frac{(1-R)^2}{2R} \quad (1)$$

here, $R = \frac{R_{Sample}}{R_{Ref-BaSO4}}$. α is the absorption coefficient, and s is the scattering coefficient of the sample. The bandgap of the sample is found using the Tauc plot method from recorded absorption spectra. Tauc equation,

$$(\alpha hv)^n = A(hv - E_g) \quad (2)$$

Here, $n = 2$ for allowed direct transition and $n = \frac{1}{2}$ for allowed indirect transition. TlSe is an indirect band gap semiconductor.[18, 21, 22] Combining the Kubelka-Munk function and Tauc plot equation we get relation,

$$(F(R)hv)^{\frac{1}{2}} = A(hv - E_g) \quad (3)$$

$(F(R)hv)^{1/2}$ is plotted against photon energy, hv, and it is fitted to the linear equation for the linear portion of $(F(R)hv)^{1/2}$. Bandgap E_g is obtained by x-intercept of this line as it is observed from the Kubelka-Munk Function and Tauc equation as shown in Figure 1.

Powder X-ray diffraction (PXRD) of bulk TlSe was carried out by Bruker D8 Advance X-ray diffractometer with Cu K_α (1.54 Å) radiation. The tetragonal symmetry (space group I4/mcm) of TlSe was confirmed from the PXRD pattern at room temperature (Figure 2a).[20] As seen in Figures 2b and 2c, the Tl^{3+} cations are situated at the centre of $(TlSe_2)_n^{n-}$ tetrahedra, which are connected by joint horizontal edges and form linear chains along the c-axis.

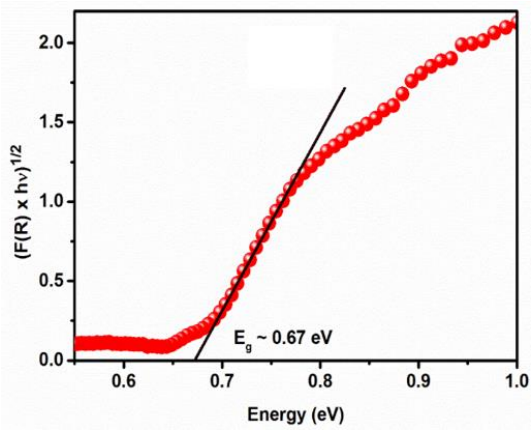

Figure 1. *Absorption spectrum showing band gap using Tau-plot of TlSe. Reprinted (adapted) with permission from ref. [20] Copyright 2019 American Chemical Society.*

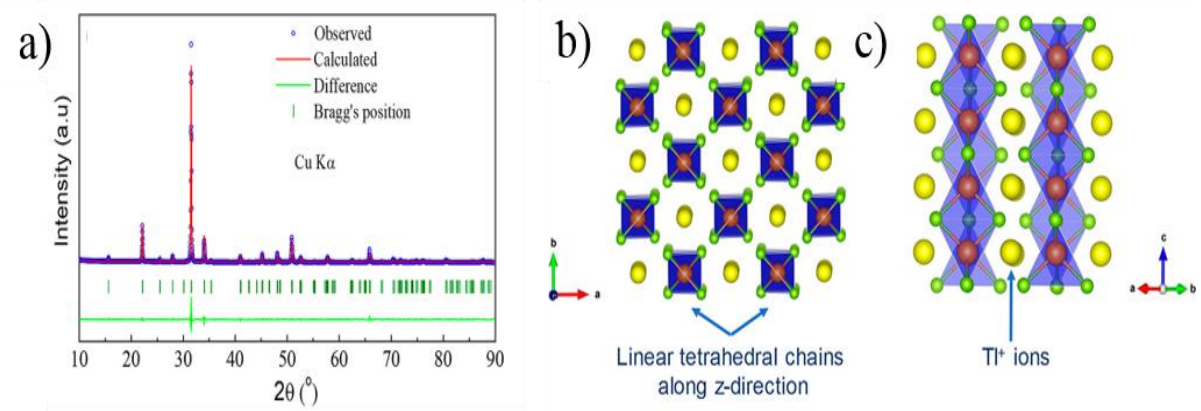

Figure 2. *a) The Rietveld refinement of the Powder X-ray diffraction (PXRD) pattern at room temperature and b-c) Structure of TlSe. Reprinted (adapted) with permission from ref [20]. Copyright 2019 American Chemical Society.*

5.2.2 Time-Domain THz Spectroscopy (THz-TDS) and Time-resolved THz spectroscopy (TRTS) in reflection geometry

Experimental Setup, including THz generation and detection, data acquisition and data analysis of both these experiments (THz-TDS and TRTS), are explained in detail in Chapter 2.

A disk-shaped single crystal of TlSe with a diameter of ~1 cm and thickness of ~ 1.3 mm was used as the sample for all THz-TDS and TRTS experiments. This piece was cut out from a bigger single crystal, and both sides were polished to reduce the scattering of the optical pump and the THz probe lights. All THz experiments were carried out at room temperature. We used 800 nm ultrafast (~35 fs) pulse from our amplifier to photoexcite the sample. To study the fluence dependence of the carrier dynamics, we varied the pump fluence from 4.7 to 123.5 $\mu J/cm^2$. We used a broadband (0.5 to 8 THz) THz probe for all THz experiments. In the TRTS experiments, horizontal polarisation was chosen for both the pump and probe beams. The beam radii of the optical pump and the THz probe on the sample were 1.7 and 0.4 mm, respectively. The beam radii were measured using the knife-edge method. This ensured the probing of uniformly photoexcited sample. For the reflection-mode THz-TDS experiments, we used a high-resistivity silicon wafer as the reference.

5.3 Result and Discussion

5.3.1 Time-Domain THz Spectroscopy (THz-TDS) in Reflection Geometry

We have obtained the complex refractive index function of TlSe in the THz frequency range using THz-time domain spectroscopy in reflection geometry. Figure 3a shows the reflected THz electric field off the TlSe sample as well as the reference (high-resistivity Si). Figure 3b depicts the experimentally observed real refractive index and the absorption coefficient of bulk TlSe in the range of 0.5 to 8 THz. We can calculate the complex dielectric function and complex conductivity of TlSe in this THz frequency range, which are important parameters for any semiconductor.

As shown in Figure 3b, there are several absorption peaks below 6 THz. The strongest optical phonon mode is at 4.75 THz. As discussed in our previous report, the low frequency (< 4 THz) lattice vibrations mainly contribute to the low intrinsic thermal conductivity in TlSe.[20] Tl^{+} is surrounded by eight atoms of Selenium (Se) atoms, which form a slightly deformed cage with a small angle skewed. The distances between Tl^{3+} and Se and, between Tl^{+} and Se are 2.69 Å and 3.43 Å respectively. Due to the presence of this strong (between Tl^{3+} and Se) and weak (Tl^{+} and Se) bondings between Tl and Se within a lattice leads to low-energy phonons (optical modes) of TlSe generated by series of Tl^{+} atoms, which is acts as intrinsic rattler-like vibration. In this compound, the rattling motion of weakly bound Tl^{+} cations scatters off the heat-carrying acoustic phonons leading to low thermal conductivity.[20] In our earlier report we found that thermal conductivity due to lattice in TlSe is low as compared to other traditional, well known low thermal conductivity compounds, as shown in Figures 4a and 4b.

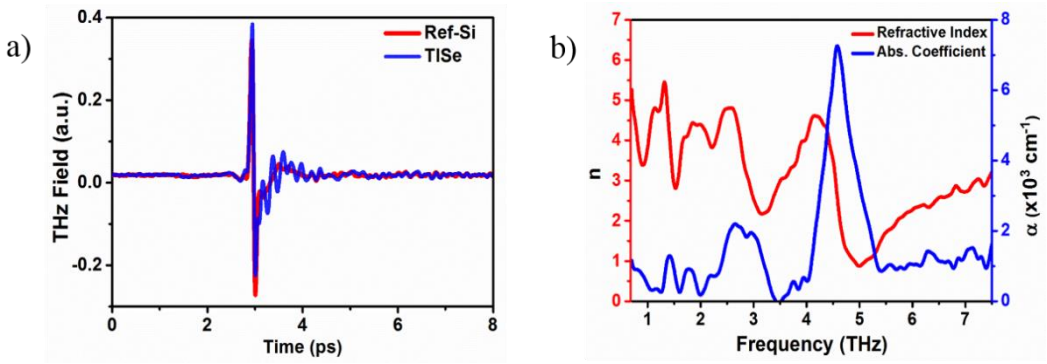

Figure 3. *a) Time-domain THz signals reflected from TlSe (sample) and reference (Silicon) and b) Refractive index and absorption coefficient of TlSe. Reprinted (adapted) with permission from ref.* [20] *Copyright 2019 American Chemical Society.*

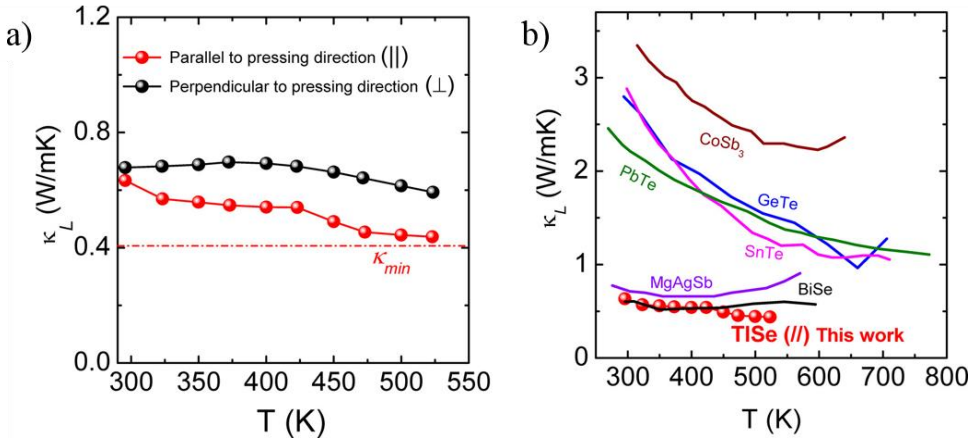

Figure 4. *a) Plot of Lattice thermal conductivity) of TlSe measured parallel (||) and (- perpendicular (⊥) to pressing directions and b) Plot of few traditional, well known ultralow thermal conductive compounds of κ_L vs temperature. (Lattice thermal conductivity= κ_L) Reprinted (adapted) with permission from ref.*[20] *Copyright 2019 American Chemical Society.*

5.3.2 Charge carrier dynamics in Thallium Selenide (TlSe)

We performed time-resolved THz spectroscopy (TRTS) in reflection geometry to investigate the charge carrier dynamics in Thallium selenide (TlSe). The sample is a circularly shaped pellet of about 1.3 mm thickness. TRTS on TlSe was carried out in reflection mode geometry due to the strong absorption of TlSe in the THz frequency band (as shown in Figure 3b) and large sample thickness. The bandgap of TlSe is 0.67 eV, which is determined from the diffuse reflectance of TlSe spectrum and Tauc-plot method. TlSe is optically excited with a pump wavelength of 800 nm (with photon energy of about 1.55 eV), and subsequent charge carrier

relaxation and recombination processes are monitored by time-delayed THz probe pulse. Pump and probe polarisations are parallel to each other and perpendicular to the press direction of sample (the pressed direction is along the c-axis of the compound). In addition to monitoring charge carrier dynamics in semiconductor, TRTS is used to determine important transport parameters such as charge carrier mobility and diffusion length.[23]

In the frequency-averaged scans in TRTS (pump scans), pump-induced change in the peak of the THz electric field is measured as a function of pump-probe time delay (t_p). Fluences from 4.7 to 123.5 μJ/cm^2 were used at excitation pump wavelength of 800 nm to observe their dependence on carrier dynamics. This fluence range corresponds to surface photon density $\left(\frac{f_l}{h\upsilon}\right)$ from 0.2 × 10^{14} to 5 × 10^{14} cm^{-2}. We estimated the bulk photon density (N_{ph}) to be 0.2 × 10^{17} to 4.6 × 10^{17} cm^{-3} from equation 4. We used the penetration depth ($\delta \sim 10\ \mu m$) of TlSe from literature [21] for this calculation.

$$N_{ph} = \frac{f_l\ (1 - R)}{h\upsilon\delta} \tag{4}$$

Here, f_l is the pump fluence R is the diffuse reflectance (reflectivity) at 800 nm, $h\upsilon$ is the photon energy corresponding to the pump wavelength, and δ is the penetration depth near the pump wavelength.

In reflection mode TRTS, the photoinduced change in the reflectance (ΔR) of THz electric field from the sample surface is monitored by measuring the photoinduced change in the peak value of the THz electric field ($\Delta E = E_{on} - E_{off}$) as a function of pump-probe time delay (t_p). ΔE is measured simultaneously with a non-excited THz electric field (E_{off}) , which is reflected from the sample surface. Transients differential THz reflectance $\left(\frac{\Delta R}{R_{off}} = \frac{\Delta E}{E_{off}}\right)$ of TlSe are obtained for fluence range from 4.7 to 123.5 μJ/cm^2. The time-dependent THz reflectance traces are given in Figure 5. It can be seen from Figure 5 that the differential reflectance (THz transient) varies with the excitation fluence. This fluence dependency is even more evident and clear from the plot of normalised differential reflectance, as shown in Figure 6a. Each THz transient represents carrier dynamics of TlSe at a given fluence, and it becomes faster with the increase in fluence as seen from normalised THz transients (Figure 6a). In TRTS,

the photoinduced differential reflectance $\left(\frac{\Delta R}{R_{off}}\right)$ is a measure of photoconductivity $(\Delta\sigma)$ of the sample, which depends on the concentration and mobility of photocarriers by the following expression (equation 5).

$$\frac{\Delta R}{R_{off}} \propto \Delta\sigma \propto n\mu \tag{5}$$

Here $n = n_e + n_h$ is the total photocarrier density and μ is the mobility of photocarrier. It is observed in frequency-averaged TRTS that the change in $\frac{\Delta R}{R_{off}}$ is largely affected by the change in carrier concentration, and mobility remains constant for a few sub-ns time window after photoexcitation.[24] Hence, we assumed that the temporal evolution of the differential THz reflectance is mostly dominated by the temporal evolution of charge carrier density in photoexcited TlSe.

a) Relaxation and recombination mechanisms

To understand relaxation and recombination mechanisms, normalised THz transients of TlSe were fitted using the Gaussian convoluted tri-exponential function (explained in Chapter 2). We obtained three different time constants/components associated with each exponential term for every normalised THz transient. We found that the fastest-time component (t_1) weakly depends on the excitation fluence. The intermediate (t_2) and the slowest time (t_3) scales strongly depend on the excitation fluence, and both time components reduce with an increase in the excitation fluence. Table 1 lists all the time constants obtained by triexponential fitting which are dependent on fluence and, hence, on initial carrier density. Variation of time components with initial carrier density is shown in Figure 7a-b and Figure 8.

We can assign different photoexcited recombination processes to time components obtained from multiexponential fitting. As shown in Figure 8, the fastest time component varies from 57 to 40 ps, with its contribution (a_1) to total recombination increasing with the fluence. This component is not strongly dependent on fluence. It is not rapidly decreasing with increase in fluence, unlike observed in Auger recombination processes. Generally, Auger recombination process is strongly dependent on excitation fluence as it involves three photocarriers. Hence, Auger recombination process associated to t_1 is less likely probable even though its

contribution (a_1) is increasing with fluence. Here, it is important to clarify that we are not completely ruling out Auger process from recombination, it can exist with smaller time scale at given experimental conditions (which we have not detected here). We can assign t_1 component to the trap-filling process in which traps are start getting filled in less than 100 ps irrespective of carrier density. Trap-filling has been observed to occur in sub-100 ps time scale in several semiconductor systems. The intermediate time component (t_2) rapidly decreases from 249 to 175 ps as fluence increases and could be attributed to bimolecular electron-hole recombination.

The slowest time component (t_3) varies from 1950 to 750 ps, and its contribution (a_3) changes weakly with fluence; it can be assigned to the trap-assisted recombination process. With increasing excitation fluence, overall carrier dynamics becomes faster as the average lifetime (as listed in Table 1) varies from 1500 to 495 ps.

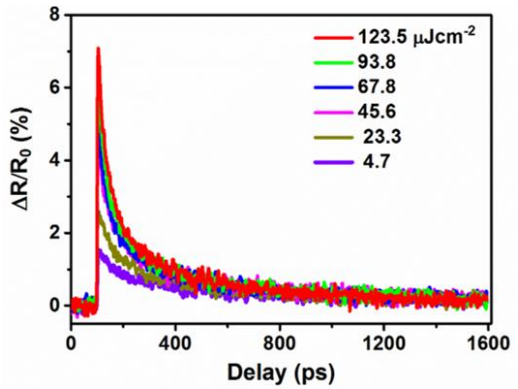

Figure 5. *THz transients with increasing fluence.*

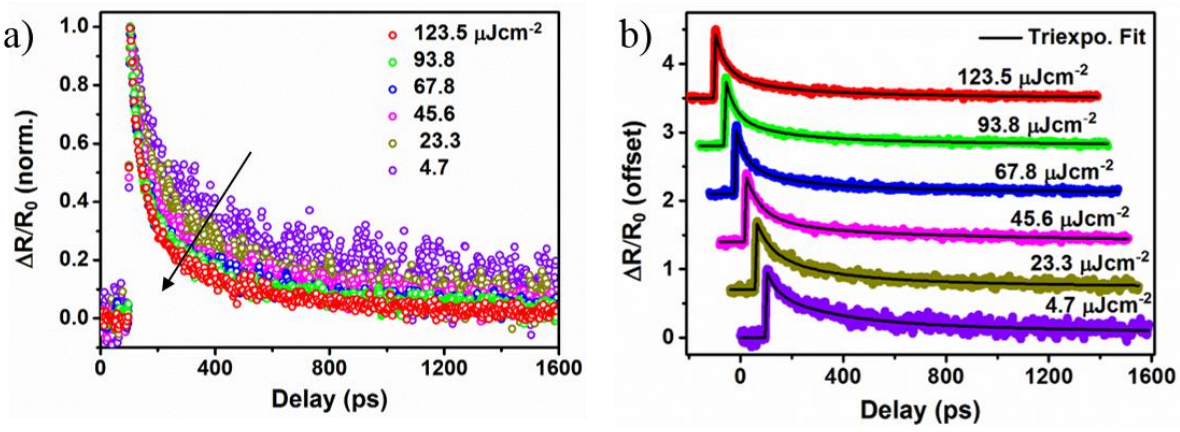

Figure 6. *a) Normalised differential reflectance and b) THz transients fitted to triexponential function.*

Table 1. *Parameters obtained from fitting THz transients to the triexponential function. (Errors/one standard deviation are given in parentheses.)*

Fluence ($\mu J/cm^2$)	t_1 (ps)	a_1	t_2 (ps)	a_2	t_3 (ps)	a_3	$< t >$ (ps)
4.7	40.1 (0.7)	0.318 (0.004)	249.1 (4.3)	0.450 (0.003)	1956 (54)	0.220 (0.004)	1567.1 (50.9)
23.3	56.9 (0.6)	0.445 (0.005)	242 (49)	0.402 (0.003)	1617) (41)	0.15 (0.003)	1154 (37)
45.6	47.7 (0.5)	0.463 (0.008)	140.4 (2.63)	0.300 (0.007)	937 (5)	0.220 (0.001)	740 (3)
67.8	37.8 (0.2)	0.556 (0.002)	209 (2)	0.321 (0.001)	1475 (22)	0.105 (0.001)	1002 (20)
93.8	38.0 (0.2)	0.557 (0.002)	177 (2)	0.305 (0.002)	1056 (9)	0.130 (0.001)	731 (7)
123.5	38.8 (0.2)	0.597 (0.002)	175 (2)	0.256 (0.002)	746 (6)	0.133 (0.002)	496 (6)

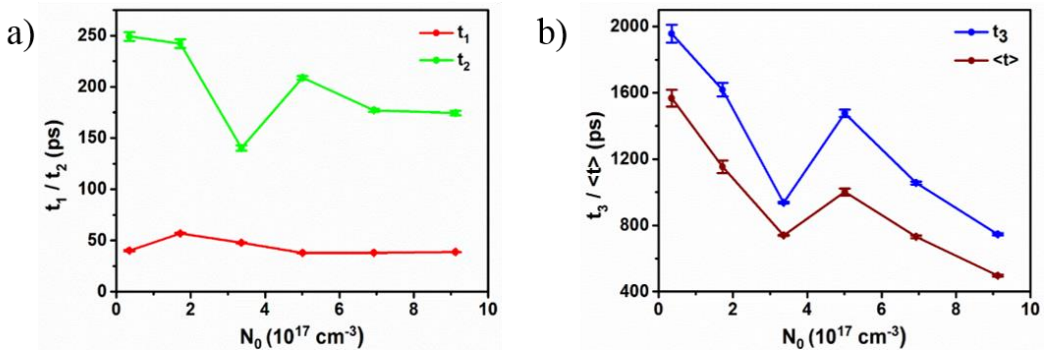

Figure 7. *Time components versus fluence. a) t_1 and t_2 (with their one standard deviation) b) t_3 and <t> (with their one standard deviation).*

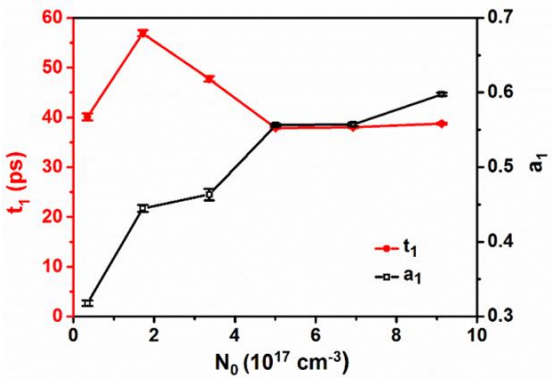

Figure 8. *The fastest time component (t_1) and its amplitude (a_1) vs carrier density.*

We also applied the global fitting procedure for fitting photoinduced THz transients to the kinetic rate equation (Figure 9). The kinetic rate equation is given as,

$$\frac{dn}{dt} = -k_1 n - k_2 n^{\,2} - k_3 n^{\,3} \qquad (6)$$

here k_1, k_2 and k_3 are rate constants corresponding to monomolecular, bimolecular and trimolecular recombination processes, respectively, and n is total carrier density.

We obtained rate constants k_1, k_2, and k_3 corresponding to three different recombination processes, as given in Table 2. Kinetic rate equation fitting and multiexponential fitting show that the charge carrier dynamics of thallium selenide involve multiple carrier recombination channels, including bimolecular, trap-assisted, and Auger recombination processes at surface photon density from 0.2 $\times 10^{14}$ to 5×10^{14} cm^{-2} (carrier density ~ 10^{17} cm^{-3}). It is evident from

Table 2 that the trap-assisted recombination (k_1) is relatively low, with a k_1 value in the order of 10^7 s^{-1}, which indicates that the trap density in the TlSe crystal is low. However, the bi-molecular recombination (k_2) and the Auger recombination rates (k_3) are significantly higher.

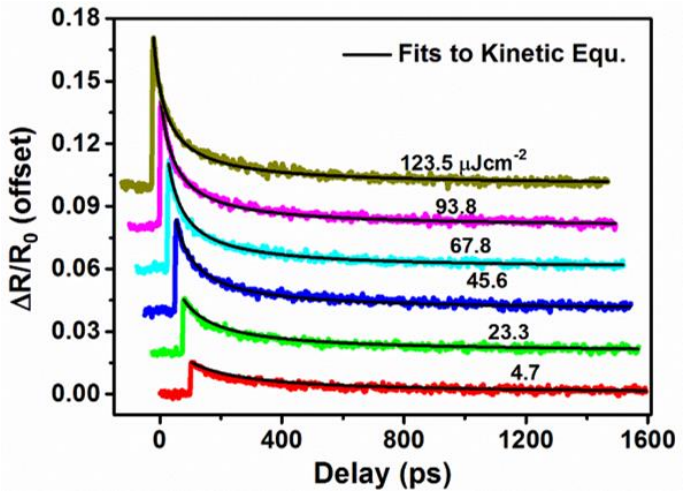

Figure 9. *THz transients fitted to the kinetic equation (equation 6) at different pump fluences. For clarity, THz transients and corresponding fits are offset by constant magnitude in the x-axis and y-axis.*

Table 2. *Carrier recombination rate constants obtained from the global fitting of THz transients at all different pump fluences to the kinetic rate equation of carrier recombination. (Errors are given in parentheses.)*

$k_1(s^{-1})$	$k_2(cm^3s^{-1})$	$k_3(cm^6s^{-1})$
3.7×10^7 (0.4×10^7)	3.92×10^{-8} (0.01×10^{-8})	4.3×10^{-27} (0.2×10^{-27})

Correlation of time constant and recombination process

In our work, time constants are extracted from multiexponential fitting. In addition to this, to understand carrier dynamics of TlSe, we also analysed fluence-dependent THz transients using the kinetic rate equation model (details are discussed in Chapter 2) and obtained rate constants for various recombination processes. These time constants are assigned to different multicarrier recombination processes by combining their (time constants) dependence on excitation fluence and kinetic rate equation modelling. For example, Auger recombination generally occurs in

semiconductors in a few tens of picoseconds, is a many-body process (three-particle process) and strongly depends on fluence. Also, we found that our data (fluence-dependent THz transients) fits well on the addition of higher order Auger recombination term ($-k_3 n_3$), and we found the fastest time constant is less than 50 ps and with its increasing contribution (a_3) with increasing fluence (Figure 8, Chapter 5). Hence, the fastest time component could be the Auger recombination process, which may occur in TlSe at a carrier density of 10^{17} cm^{-3}. Here, we also suggested another possibility for the fastest component: the trap-sate filling process, as this time constant is not rapidly decreasing with excitation fluence. But, our kinetic fitting analysis suggests the existence of the Auger process at 10^{17} cm^{-3} in our bulk TlSe sample. The time constant, t_2, is assigned to bimolecular recombination; it decreases with fluence, with the time component varying from 250 ps to 175 ps. TlSe is a narrow bandgap semiconductor with an (indirect) bandgap of about 0.67 eV (1850.5 nm), and absorbance is not collected due to the unavailability of a spectrometer in that wavelength range. Whether bulk TlSe emits in the near-infrared or not, it will be interesting to observe its emission properties. The reasonable value of the bimolecular rate constant of about 3.92×10^{-8} ($\pm 0.01 \times 10^{-8}$) $cm^3 s^{-1}$ is found from kinetic fitting analysis. Compared to a few other narrow/near-infrared bandgap semiconductors, as listed in Table 3 below (InAs, InSb, GaSb etc.), the rate constant is reasonably high; hence, we think a bimolecular process exists as one of the recombination processes with a time constant a roughly corresponding to t_2. The slowest time constant, t_3, is assigned to trap-assisted recombination as in many semiconductors, and this process happens in 1000s of picoseconds.

Table 3. *Rate constants for some of the narrow bandgap semiconductors.*

(k_2 :Bimolecular recombination rate constant; k_3: Auger recombination rate constant
**Not narrow bandgap semiconductor but technological import one*
***Tin perovskite shows promising light-emission properties)*

Material	Bandgap	k_2 ($cm^3 s^{-1}$)	k_3 ($cm^6 s^{-1}$)	Reference
InAs	0.35 eV	$\sim 1.1 \times 10^{-10}$ (298 K)	$\sim 2.2 \times 10^{-27}$ (300 K)	25
InSb	0.17 eV	$\sim 5 \times 10^{-11}$	5×10^{-26} ($\geq$ 250 K)	25
GaSb	0.726 eV	$\sim 10^{-10}$	$\sim 10^{-30}$ (300 K)	25

Si	1.12 eV	1.1×10^{-14} (300 K)	1.1×10^{-30} (300 K)	[25]
Ge	0.661 eV	6.4×10^{-14}		[25]
**$CsSnI_3$	1.3 eV	$\sim 10^{-8}$		[26]
*GaAs	1.424 eV	7×10^{-10}		[25]
TlSe	0.67 eV	3.92×10^{-8} (300 K)	4.3×10^{-27} (300 K)	Our work

b) Carrier Mobility and Diffusion length

The TRTS measurement of semiconductors estimates the charge carrier mobility and diffusion length in a non-contact fashion. We have evaluated these two parameters for thallium selenide (Table 3). The mobility and the diffusion length are 54.8 ± 12.9 cm^2/Vs and 472 ± 63.1 nm, respectively, at the lowest excitation fluence of 4.7 $\mu J/cm^2$.

Table 4. *Mobility and diffusion length obtained through TRTS of TlSe. (peak photoconductivity=$\Delta\sigma_{Peak}$) (Errors are given in parentheses.)*

Fluence ($\mu J/cm^2$)	N_{ph} ($10^{17} cm^{-3}$)	$\Delta R/R_0$ (max.)	$\Delta\sigma_{Peak}$ (S/m)	Mobility (cm^2/Vs)	$\langle t \rangle$ (ps)	Diffusion length (nm)
4.7	0.2	0.015 (0.004)	30.7 (7.2)	54.8 (12.9)	1567.1 (50.9)	472 (63.1)
23.3	0.9	0.025 (0.004)	50.2 (8.6)	18.2 (3.1)	1154.3 (37)	233 (23.7)
45.6	1.7	0.043 (0.004)	85.9 (8.4)	16.0 (1.6)	740.3 (3)	175 (8.9)
67.8	2.5	0.052 (0.003)	103.0 (6.2)	13.0 (0.8)	1001.7 (20)	183 (7.4)
93.8	3.5	0.061 (0.003)	120.9 (6.7)	10.9 (0.6)	731.4 (7)	144 (4.7)
123.5	4.6	0.071 (0.004)	141.2 (8.3)	9.7 (0.6)	495.9 (6)	111 (3.9)

c) Comparison of Intrinsic conductivity and photoconductivity of TlSe

We have compared the conductivity of TlSe based on two approaches- the direct (contact method) method measured through the four-probe method using the ULVAC-RIKO ZEM3 instrument and the non-contact method measured through TRTS (by evaluating peak photoconductivity) (Table 5). Electrical conductivity is around 0.10 S/cm at room temperature as measured by the four-probe method.[20] The conductivity measured by the four-probe method is the intrinsic (dark) conductivity of the material, which depends on the intrinsic carrier density. The intrinsic carrier concentration of TlSe is about 10^{16} cm^{-3}.[21]. Table 4 shows that the photoinduced change in conductivity from the TRTS experiment is 0.31 S/cm at the lowest fluence of 4.7 $\mu J/cm^2$ and at the corresponding photocarrier density (N_0) of 0.4×10^{17} cm^{-3}.

Table 5. *Comparison of four-probe conductivity and TRTS photoconductivity at lowest fluence. (n_0: intrinsic carrier concentration)*

Sample	Four-probe	TRTS	n_0	N_0
TlSe	0.10 S/cm	0.31 S/cm	~10^{16} cm^{-3}	~10^{17} cm^{-3}

Our estimated mobility (54.8 cm^2/Vs) and diffusion length (472 nm) values at this carrier density level are encouraging. It is worth mentioning that the ideal thermoelectric material has an intrinsic carrier concentration (n_0) of around ~10^{19}-10^{20} cm^{-3} and electronic conductivity is at least around ~10^2 S/cm.[4, 27] We make an important inference from our observations on the comparison of conductivities that the TlSe crystal, made with higher doping, can lead to higher intrinsic carrier density to achieve an optimum electronic conductivity for its potential thermoelectric application.

Overall, we studied a class III-VI semiconductor, TlSe, which was recently shown to have ultralow thermal conductivity. Our THz-TDS study provides quantitative measurement of IR-active phonon modes (in the THz frequency range), which are found to be one of the main reasons for their low thermal conductivity. Carrier dynamics mainly dominated by free carriers have shown multicarrier recombination pathways as investigated by reflection mode TRTS experiments. We found rate constants for multicarrier recombination processes such as monomolecular, bimolecular and trimolecular recombination processes. THz study on TlSe

offers a great advantage in evaluating material's performance for desired applications, especially in monitoring photoexcited properties for light-emitting applications and phonon dynamics for thermoelectric.

5.4 Conclusions

TlSe is one of the interesting semiconductors from class III-VI due to its potential thermoelectric applications. In terms of its optical and electrical properties, not much research has been done on TlSe. We have observed low-frequency absorption modes lie in the THz frequency range studied from THz-TDS experiments, which is one of the main reasons for the ultralow thermal conductivity of TlSe. Since semiconductors from class III-VI have also shown promising optical and electronic properties, and TlSe has not been explored and studied in this direction, we have conducted TRTS experiments to unravel charge carrier dynamics in TlSe in order to shed light on its electronic properties in excited states. The dynamics of photocarriers in TlSe is studied using the reflection mode TRTS technique, which is an entirely novel and important experiment to conduct on such material to get a detailed understanding in this direction. Multiple carrier recombination pathways, including bimolecular and Auger recombination, are involved in photoexcited dynamics of TlSe at a photocarrier density of about 10^{17} cm^{-3}. The Intrinsic conductivity and the photoconductivity are measured and have been found in a similar order of magnitude. In estimating the electronics transport properties of TlSe, our results from a non-contact TRTS measurement of mobility and diffusion length are also quite encouraging.

More systematic investigations, especially on thin films, are required to fully explore the potential of TlSe from the standpoint of optoelectronics and thermoelectric applications. In this work, we have not investigated the phonon dynamics, and it will be more insightful to probe the phonon dynamics and the carrier-phonon coupling using appropriate TRTS and other pump-probe experiments.

5.5 References

1. Springholz, G.; Bauer, G., Semiconductors, IV–VI. In *Wiley Encyclopedia of Electrical and Electronics Engineering*, **2014**; pp 1-16.
2. Yang, Z.; Hao, J., Recent Progress in 2D Layered III–VI Semiconductors and their Heterostructures for Optoelectronic Device Applications. *Advanced Materials Technologies* **2019,** *4* (8), 1900108.
3. Zhao, L.-D.; Lo, S.-H.; Zhang, Y.; Sun, H.; Tan, G.; Uher, C.; Wolverton, C.; Dravid, V. P.; Kanatzidis, M. G., Ultralow thermal conductivity and high thermoelectric figure of merit in SnSe crystals. *Nature* **2014,** *508* (7496), 373-377.
4. Zhou, C.; Lee, Y. K.; Yu, Y.; Byun, S.; Luo, Z.-Z.; Lee, H.; Ge, B.; Lee, Y.-L.; Chen, X.; Lee, J. Y.; Cojocaru-Mirédin, O.; Chang, H.; Im, J.; Cho, S.-P.; Wuttig, M.; Dravid, V. P.; Kanatzidis, M. G.; Chung, I., Polycrystalline SnSe with a thermoelectric figure of merit greater than the single crystal. *Nature Materials* **2021,** *20* (10), 1378-1384.
5. Zhang, Q.; Cao, F.; Lukas, K.; Liu, W.; Esfarjani, K.; Opeil, C.; Broido, D.; Parker, D.; Singh, D. J.; Chen, G.; Ren, Z., Study of the Thermoelectric Properties of Lead Selenide Doped with Boron, Gallium, Indium, or Thallium. *Journal of the American Chemical Society* **2012,** *134* (42), 17731-17738.
6. Zhang, Q.; Wang, H.; Liu, W.; Wang, H.; Yu, B.; Zhang, Q.; Tian, Z.; Ni, G.; Lee, S.; Esfarjani, K.; Chen, G.; Ren, Z., Enhancement of thermoelectric figure-of-merit by resonant states of aluminium doping in lead selenide. *Energy & Environmental Science* **2012,** *5* (1), 5246-5251.
7. Wang, H.; Gibbs, Z. M.; Takagiwa, Y.; Snyder, G. J., Tuning bands of PbSe for better thermoelectric efficiency. *Energy & Environmental Science* **2014,** *7* (2), 804-811.
8. Parker, D.; Singh, D. J., High-temperature thermoelectric performance of heavily doped PbSe. *Physical Review B* **2010,** *82* (3), 035204.
9. Gayner, C.; Kar, K. K.; Kim, W., Recent progress and futuristic development of PbSe thermoelectric materials and devices. *Materials Today Energy* **2018,** *9*, 359-376.
10. Zhao, L.-D.; Hao, S.; Lo, S.-H.; Wu, C.-I.; Zhou, X.; Lee, Y.; Li, H.; Biswas, K.; Hogan, T. P.; Uher, C.; Wolverton, C.; Dravid, V. P.; Kanatzidis, M. G., High Thermoelectric Performance via Hierarchical Compositionally Alloyed Nanostructures. *Journal of the American Chemical Society* **2013,** *135* (19), 7364-7370.
11. Hu, P.; Wen, Z.; Wang, L.; Tan, P.; Xiao, K., Synthesis of Few-Layer GaSe Nanosheets for High Performance Photodetectors. *ACS Nano* **2012,** *6* (7), 5988-5994.
12. Late, D. J.; Liu, B.; Luo, J.; Yan, A.; Matte, H. S. S. R.; Grayson, M.; Rao, C. N. R.; Dravid, V. P., GaS and GaSe Ultrathin Layer Transistors. *Advanced Materials* **2012,** *24* (26), 3549-3554.
13. Arora, H.; Jung, Y.; Venanzi, T.; Watanabe, K.; Taniguchi, T.; Hübner, R.; Schneider, H.; Helm, M.; Hone, J. C.; Erbe, A., Effective Hexagonal Boron Nitride Passivation of Few-Layered InSe and GaSe to Enhance Their Electronic and Optical Properties. *ACS Applied Materials & Interfaces* **2019,** *11* (46), 43480-43487.
14. Auerhammer, J. M.; Eliel, E. R., Frequency doubling of mid-infrared radiation in gallium selenide. *Optics Letters* **1996,** *21* (11), 773-775.
15. Jie, W.; Chen, X.; Li, D.; Xie, L.; Hui, Y. Y.; Lau, S. P.; Cui, X.; Hao, J., Layer-Dependent Nonlinear Optical Properties and Stability of Non-Centrosymmetric

Modification in Few-Layer GaSe Sheets. *Angewandte Chemie International Edition* **2015,** *54* (4), 1185-1189.
16. Liu, K.; Xu, J.; Zhang, X. C., GaSe crystals for broadband terahertz wave detection. *Applied Physics Letters* **2004,** *85* (6), 863-865.
17. Kudrynskyi, Z. R.; Kerfoot, J.; Mazumder, D.; Greenaway, M. T.; Vdovin, E. E.; Makarovsky, O.; Kovalyuk, Z. D.; Eaves, L.; Beton, P. H.; Patanè, A., Resonant tunnelling into the two-dimensional subbands of InSe layers. *Communications Physics* **2020,** *3* (1), 16.
18. Ellialtıoğlu, Ş.; Mete, E.; Shaltaf, R.; Allakhverdiev, K.; Gashimzade, F.; Nizametdinova, M.; Orudzhev, G., Electronic structure of the chainlike compound TlSe. *Physical Review B* **2004,** *70* (19), 195118.
19. Ketelaar, J. A. A.; t'Hart, W. H.; Moerel, M.; Polder, D., The Crystal Structure of TlSe, Thallous Thallic or Thallosic Selenide. **1939,** *101* (1-6), 396-405.
20. Dutta, M.; Matteppanavar, S.; Prasad, M. V. D.; Pandey, J.; Warankar, A.; Mandal, P.; Soni, A.; Waghmare, U. V.; Biswas, K., Ultralow Thermal Conductivity in Chain-like TlSe Due to Inherent Tl+ Rattling. *Journal of the American Chemical Society* **2019,** *141* (51), 20293-20299.
21. Itoga, R. S.; Kannewurf, C. R., Electrical resistivity, hall effect and optical absorption in TlS, TlS0·5Se0·5 and TlSe. *Journal of Physics and Chemistry of Solids* **1971,** *32* (6), 1099-1110.
22. Pickar, P. B.; Tiller, H. D., Optical Energy Gap in TlSe. *physica status solidi (b)* **1968,** *29* (1), 153-158.
23. Ulbricht, R.; Hendry, E.; Shan, J.; Heinz, T. F.; Bonn, M., Carrier dynamics in semiconductors studied with time-resolved terahertz spectroscopy. *Reviews of Modern Physics* **2011,** *83* (2), 543-586.
24. Zhao, D.; Chia, E. E. M., Free Carrier, Exciton, and Phonon Dynamics in Lead-Halide Perovskites Studied with Ultrafast Terahertz Spectroscopy. *Advanced Optical Materials* **2020,** *8* (3), 1900783.
25. Gildenblat, G. S.; Goldberg, Y. A.; Levinshtein, M. E.; Mikhailova, M. P.; Rumyantsev, S.; Schmidt, N. M.; Shur, M. S.; Vorobjev, L.; Vul', A. Y., *Handbook Series On Semiconductor Parameters, Vol. 1: Si, Ge, C (Diamond), Gaas, Gap, Gasb, Inas, Inp, Insb*. World Scientific Publishing Company: **1996**.
26. Xing, G.; Kumar, M. H.; Chong, W. K.; Liu, X.; Cai, Y.; Ding, H.; Asta, M.; Grätzel, M.; Mhaisalkar, S.; Mathews, N.; Sum, T. C., Solution-Processed Tin-Based Perovskite for Near-Infrared Lasing. *Advanced Materials* **2016,** *28* (37), 8191-8196.
27. Tan, G.; Zhao, L.-D.; Kanatzidis, M. G., Rationally Designing High-Performance Bulk Thermoelectric Materials. *Chemical Reviews* **2016,** *116* (19), 12123-12149.

Chapter 6

Ultrafast Charge Carrier Dynamics of Few-Layer Black Phosphorus Nanoparticles Film

6.1 Introduction

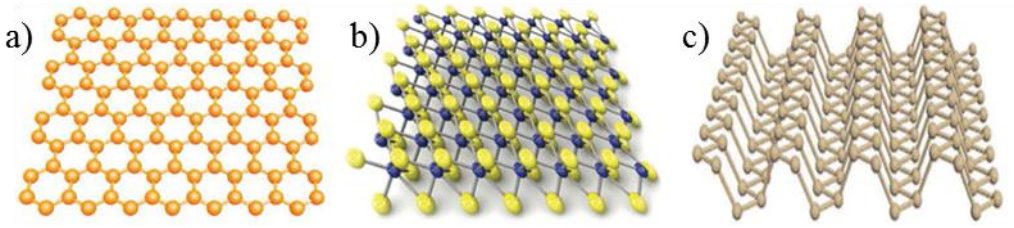

Figure 1. *Schematic of the crystal structure of two-dimensional materials: a) Graphene, b) Transition metal dichalcogenides and c) Black phosphorus. Reproduced with permission from ref.* [1] *Copyright 2017, John Wiley & Sons.*

Black phosphorus (BP) is an elemental two-dimensional (2D) material like graphene. BP has emerged as one of the important and stable allotropes of phosphorus from a semiconducting applications point of view.[2] It has been under re-investigation since the last decade due to its layer-dependent optoelectronic and nonlinear optical properties.[2, 3] In the last two decades, 2D materials, mainly graphene and transition metal dichalcogenides (TMDs/TMDCs), have attracted the research community with their excellent and promising electronic and optoelectronic properties. Figure 1 represents the crystal structures of all three 2D materials, in which graphene has a planer structure, TMDs have a sandwiched structure (monolayer contains a metal atom sandwiched between two chalcogens), and black phosphorus has a puckered structure.

Bandgap plays a crucial role in deciding specific properties of any semiconductor materials. Generally, the bandgap is expected to increase by about 50% when multilayers of 2D material are reduced to a monolayer. This increase in the bandgap is even higher in the case of black phosphorus.[4, 5] The bandgap of graphene has a zero bandgap, while the bandgap of TMDs varies from 1.0 to 2.5 eV as the number of layers decreases.[2, 6] In the case of black phosphorus, the bandgap in the bulk phase is about 0.3 eV and about 2 eV for its monolayer.[2] With the wide tunability of the bandgap of black phosphorus, a broad range of the electromagnetic spectrum, starting from mid-infrared, near-infrared and up to visible, can be utilised in optoelectronic applications and other fields such as plasmonics, communication, defence etc. Therefore, black phosphorus has the potential to fill the gap created by TMDs and graphene based 2D materials regarding multi applications.

It is also important to point out the transport properties of all three 2D material systems. Graphene has carrier mobility as high as 10,000 cm^2/Vs; the mobility of TMDs is much lower than graphene, dropping to below 1000 cm^2/Vs, while black phosphorus has shown mobility of 1000 cm^2/Vs at room temperature.[7,8] Furthermore, black phosphorus exhibits in-plane anisotropy. Distinctive puckered layered shape derives the in-plane anisotropy with different arrangements of atoms along the armchair and zigzag axes. As a result, the effective masses of the carrier along these two axes differ, which leads to different transport of carriers along the two axes.[2] It is also found that black phosphorus shows polarisation-dependent properties due to in-plan anisotropy and can be advantageous, especially in photonic devices.[6]

It is immensely important to understand the interactions of charge carriers among themselves and with the lattice for achieving full potential of black phosphorus in different optoelectronic applications. There are limited reports of charge carrier recombination dynamics of BP using different ultrafast spectroscopy.[9-15] However, use of time-resolved THz spectroscopy (TRTS) to probe the photoexcited state of BP can provide direct information about the nature and ultrafast dynamics of the charge carriers and their interaction with the lattice vibrations. We can also determine crucial semiconductor properties such as carrier mobility and diffusion length. Here in this work, we have investigated charge carrier dynamics study of few-layer black phosphorus (FLBP) nanoparticles (NPs) film using time-resolved THz spectroscopy (TRTS). This study will help to understand photoexcited relaxation and recombination dynamics of FLBP NPs films.

6.2 Experimental Section

6.2.1 Synthesis, characterisation and film preparation of few-layer black phosphorus

Synthesis

The liquid exfoliation method was used to synthesise few-layer BP NPs.[16-18] Few-layer BP NPs were synthesised by the liquid exfoliation method. In an argon-filled glove box, 5 mg of as-purchased black phosphorus crystals were taken with 1 mL of N-methyl pyrrolidone (NMP) in a mortar. The crystals were grounded with a pestle for ~30 min, and a further 3 mL NMP was added. The mixture was transferred to a glass vile and bath sonicated in an ice bath at 300 W

power for 5 hours. After centrifuging the sonicated dispersion at 4000 rpm for 45 min, the top 80 % supernatant was pipette out gently, which contained FLBP NPs. NPs consist of sheets of black phosphorus; hence, they are few-layer black phosphorus NPs.

Characterization

The formation of nanoparticles of black phosphorus was confirmed by transmission electron microscopy images, as shown in Figure 2b. Atomic force microscopy (AFM) was used to measure thickness of nanoparticles, which is about 2 to 4 nm, as shown in Figure 3a-d. UV-visible spectra of FLBP NPs in N-methyl-2-pyrrolidone (NMP) were collected using a Shimadzu UV 3600 plus spectrometer, as shown in Figure 2a. Raman spectrum, collected using micro Raman spectrometer (Renishaw) with an excitation wavelength of 532 nm, was used to characterise FLBP NPs, which clearly indicates characteristics peaks of phonon modes, namely A_g^1 (out of plane mode), B_{2g}, (in-plane mode) and A_g^2 (in-plane mode) as shown in Figure 2c and these peaks are centered at 358.5 cm^{-1}, 433.6 cm^{-1} and 461.5 cm^{-1} respectively.[19] We made thin films of FLBP nanoparticles on 1 mm thick polystyrene substrate for TRTS experiments. Polystyrene is transparent to the broadband probe THz light. We used the drop-cast method for the film fabrication. We placed another polystyrene substrate of the same dimension on top of the drop-casted film and sealed from all four sides to prevent the FLBP film from any environmental exposure during storing, transporting, and different experiments. It should be noted that the film was made and stored inside a nitrogen-filled glovebox at ambient temperature. It is also important to note that our THz setup is placed inside an enclosure continuously purged with dry nitrogen gas, which assures no or minimum exposure of the sample to moisture and ambient air during the TRTS experiments.

The absorbance of black phosphorus can play an important role in distinguishing its size and morphology. The bulk bandgap of black phosphorus is about 0.3 eV[3, 20] and the bandgap increases upon reducing the number of layers. Bandgap variation with the number of layers strongly reflects in the absorption spectrum. We recorded the UV-visible spectra of the polystyrene substrate and the FLBP NPs films in transmission mode using a fibre-coupled miniature UV-visible spectrometer (Ocean Optics, USB 4000) Figure 2a shows the absorption spectra of the substrate and the FLBP nanoparticles films along with the spectrum of the NPs solution. The absorbance of NPs film shifts to a longer wavelength as compared to NPs solution

(Figure 2a), which probably implies the formation of thicker NPs with more layers stacked together. Based on the absorption spectra of FLBP NPs reported in the literature, we made a rough estimate of the number of layers present in the NPs, both in solution and the film.[9, 18] Our NPs solution consists of 3-5 layers, whereas the NPs film consists of 6-10 layers. Based on the number of layers present in NPs film, NPs possess an effective bandgap, which might be about less than 0.6 eV. Photoluminescence (PL) spectra were measured for a thin film of FLBP for different excitation wavelengths using FLS 980 (Edinburgh Instruments), as shown in Figure 2d. PL peaks are near-infrared, around 930 nm to 1001 nm, from excitation wavelengths ranging from 618 nm to 670 nm.

In the THz time-resolved spectroscopic study, we probed few-layer BP NPs films of about 6-10 layers with a bandgap of less than 0.6 eV.

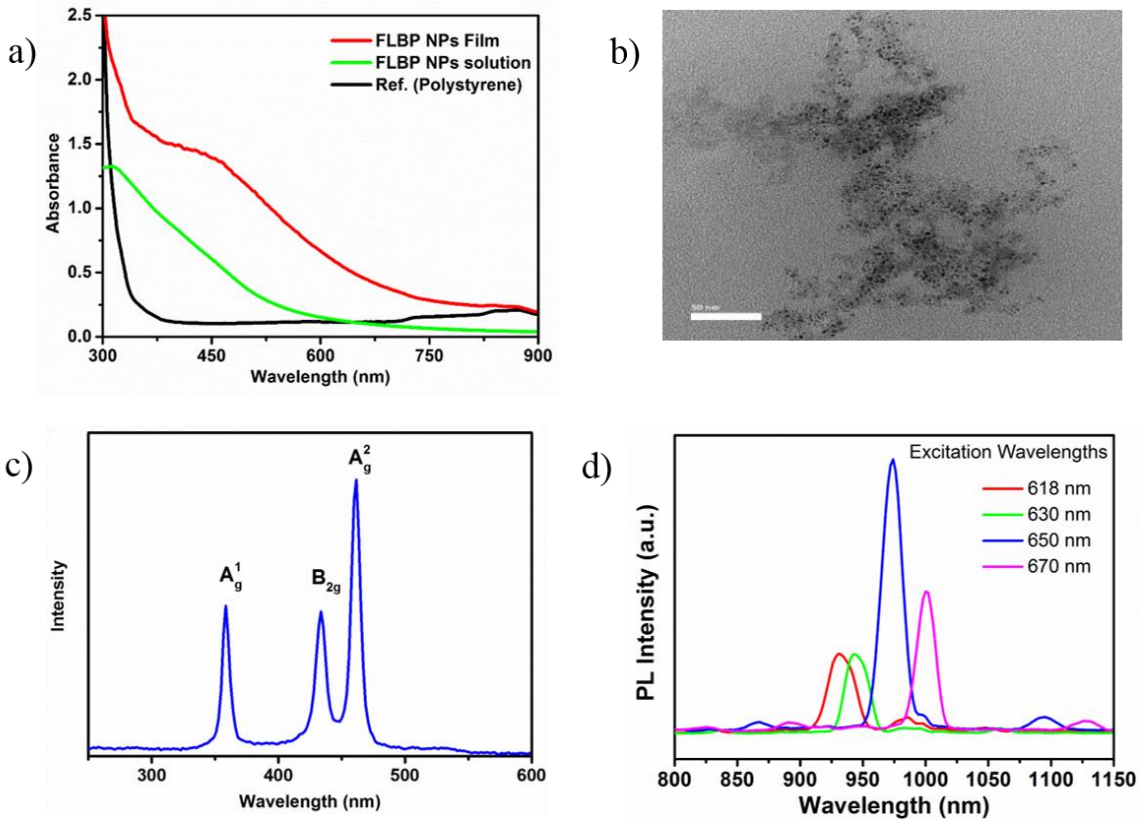

Figure 2*. a) Absorption spectra of FLBP NPs solution (dispersion) in NMP (green), Polystyrene substrate (black), and the FLBP nanoparticles film drop-casted on polystyrene (red) b) TEM image of FLBP NPs (the scale bar is of 50 nm) c) Raman spectrum of FLBP nanoparticles in solution and d) PL spectra of FLBP NPs film.*

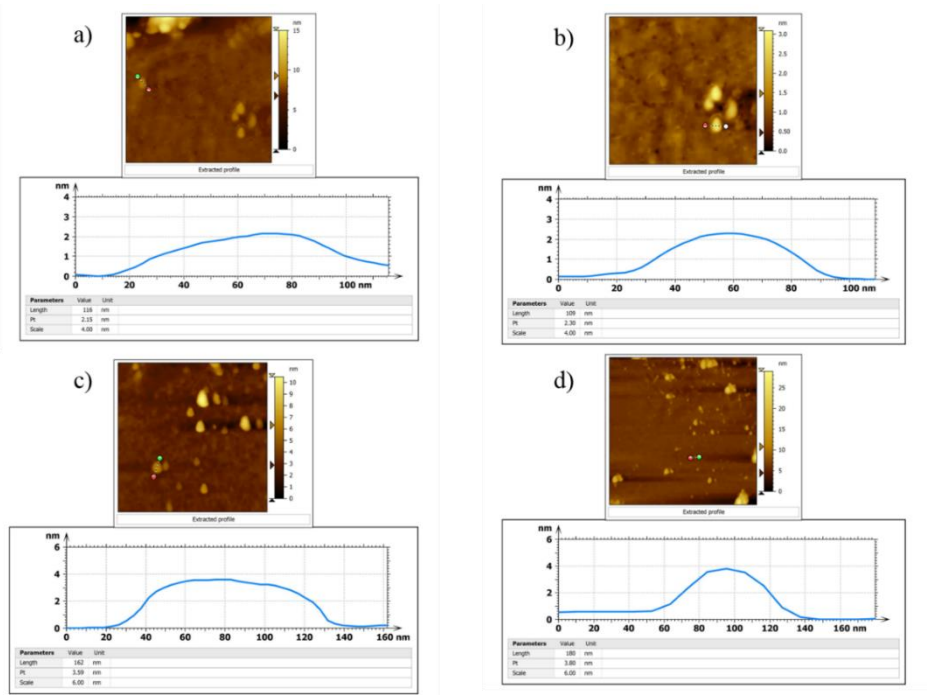

Figure 3. *AFM images showing the thickness of NPs.*

6.2.2 Time-resolved THz spectroscopy in transmission

Experimental setup, data acquisition, and data analysis of time-resolved THz spectroscopy are explained in detail in Chapter 2. Three different pump wavelengths, 480 nm, 600 nm and 800 nm with horizontal polarisation, were used (as pump wavelengths) to photoexcited few-layer black phosphorus NPs. Pump and THz probe beams have the same horizontal polarisation at the film sample. Instrument response functions (IRF) is 300 fs as determined by the cross-correlation of pump and probe beams.

6.3 Results and Discussion

6.3.1 Photoexcited charge carrier dynamics in few-layer black phosphorus nanoparticles film

We employed time-resolved THz spectroscopy (TRTS) in transmission geometry on a few-layer black phosphorus nanoparticles (FLBP NPs) film to study its charge carrier dynamics. Our TRTS setup is based on the amplified ultrafast Ti:sapphire laser system, which is explained in detail in Chapter 2.

To photoexcite the sample, pump wavelengths were obtained from an optical parametric amplifier. Three wavelengths, 480 nm, 600 nm and 800 nm, were chosen to photoexcite the few-layer BP NPs film based on its absorbance. Compared to NPs solution, the absorbance of NPs film is broad and redshifted, suggesting the formation of bigger NPs consisting of more number of layers, as per our discussion in section 6.2. Due to the bigger size of NPs, the bandgap reduces, which is estimated to be around 0.6 eV or less.

In a typical TRTS experiment, the sample is photoexcited with a femtosecond (fs) optical pulse known as a pump pulse, which leads to the creation of non-equilibrium photocarriers. Subsequent relaxation and recombination are traced by interrogating photocarriers with a THz electric field pulse known as a probe pulse. Photoinduced change in transmission of THz electric field (ΔE) is recorded with respect to pump-probe time delay. Change in the transmission of the THz electric field (ΔE) is the difference between the transmission of THz electric fields in the presence and absence of an optical pump pulse. Here, we performed frequency-averaged scans of TRTS (discussed in Chapter 2) where transmission of the peak of the THz electric field through the sample in excited and non-excited states is monitored by means of measuring the photoinduced change in transmission of the THz electric field.[21]

All pump wavelength excites few-layer BP NPs films above the bandgap. Excitation pump fluences were used in the range of 3.8 to 42.2 μJcm^{-2} for all wavelengths corresponding to surface photon density $\left(\frac{f_l}{h\upsilon}\right)$ in the range 10^{13}-10^{14} cm^{-2}. Average radii of pump beams at the sample position were 1.8 mm, 2.2 mm, and 1.5 mm for 480 nm, 600 nm and 800 nm, respectively. Average radius of probe beam was 0.4 mm. Absorbed photon density (N_{ph}) and photocarrier density(N_0) were calculated from the following equations 1 and 2, respectively.

$$N_{ph} = \frac{\alpha\, f_l\, (1 - 10^{-OD})}{h\upsilon} \quad (1)$$

$$N_0 = 2N_{ph}\varphi \quad (2)$$

Here f_l is excitation fluence, OD refers to optical density, $h\nu$ is photon energy of pump pulse, α is absorption coefficient, and φ is photon to charge carrier conversion ratio. To calculate N_{ph}, the absorption coefficient is taken from the literature.[22] N_{ph} is in the range of 10^{17}-10^{18} cm^{-3}. The absorption spectrum of few-layer BP NPs films does not reflect any confinement and excitonic signatures (Figure 1a). Hence the excitonic binding energy in multilayer black phosphorus could be lower than room temperature energy (25 meV), and it is reported that excitonic binding energy is about 8 meV in bulk BP.[15, 20] Hence, the dominant photoexcited species most likely are either free or very loosely bound charge carriers.

We have recorded frequency-averaged scans of TRTS on three different wavelengths, 480 nm, 600 nm and 800 nm, to understand the excitation wavelength-dependent carrier dynamics of few-layer BP NPs film. Figure 4a-c shows the negative differential transmission $\left(\frac{-\Delta E}{E_0}\right)$ versus pump-probe time delay at different fluences for three wavelengths (for visual clarity $\left(\frac{-\Delta E}{E_0}\right)$ scans are offset by -25 and 1.5% units along the x-axis and y-axis, respectively). All the measured wavelength-dependent THz traces lie in the linear excitation region, as confirmed by plotting the peak of every trace $\left(\frac{-\Delta E}{E_0}\right)$ vs fluence, and these graphs are fitted with linear equation (with adj. $R^2 > 0.90$) in Figure 4d-f.

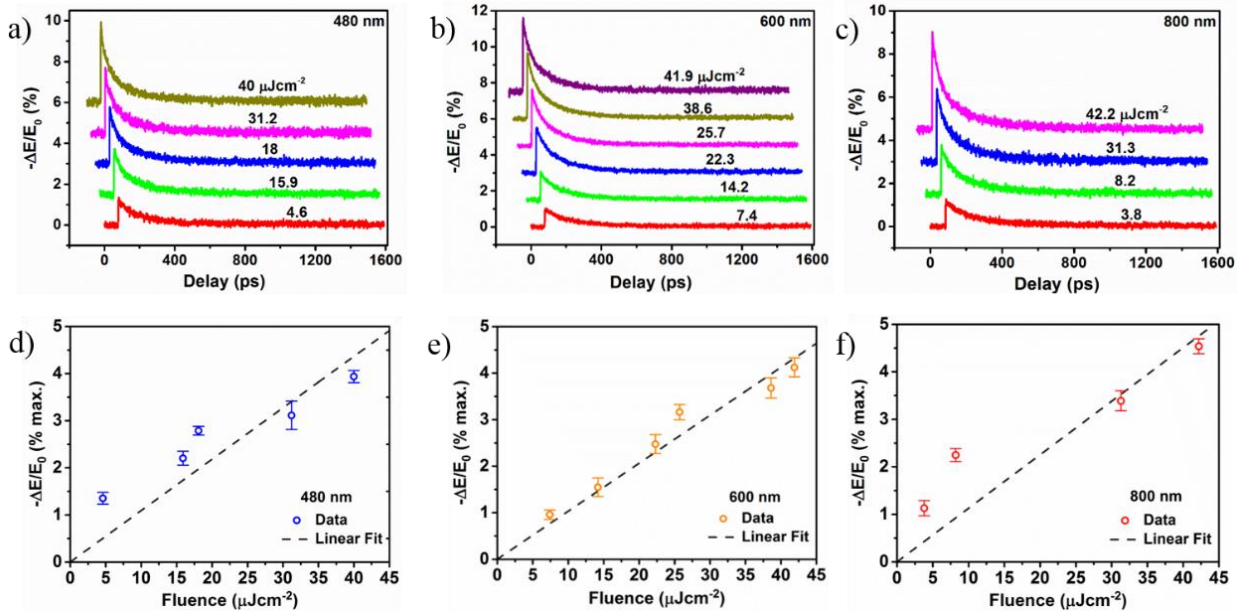

***Figure 4**. THz transients at three wavelengths: a)480 nm, b)600 nm and c)800 nm. Maximum differential transmission versus fluence and their fits to a linear equation d)480 nm (adj. R^2 ~ 0.94), e)600 nm (adj. R^2 ~ 0.99) and f) 800 nm (adj. R^2 ~ 0.92).*

THz transient (i.e. each $\left(\frac{-\Delta E}{E_0}\right)$ scan) represents charge carrier dynamics of few-layer BP NPs films under the photoexcitation of pump wavelength. Charge carrier dynamics involves various carrier relaxation and recombination channels. To understand relaxation and recombination processes in few-layer BP NPs film, we have analysed wavelength-dependent THz transients using multiexponential functions fitting and kinetic rate equations with a global fitting procedure.

THz transients for each wavelength were normalised with their maximum value, showing their fluence dependency as shown in Figure 5. Carrier dynamics is very weakly dependent on fluence, and it becomes slightly faster with increasing fluence for all three wavelengths. The Gaussian convoluted multiexponential function (equation 3) was used to fit normalised THz transients.

$$y(t) = G(t - t_0) \otimes \frac{\sum_i^n a_i \, exp(t - t_0)}{t_i} \qquad (3)$$

$y(t)$ represents normalised THz transient and Gaussian function, centred at t_0 is represented by $G(t - t_0)$ and with the full width at half maximum (FWHM) is about 300 fs. This Gaussian

function represents the instrument response function (IRF) of our TRTS setup. THz transients cannot be fitted well using the monoexponential and biexponential functions. Fluence-dependent normalised THz transients are fitted reasonably well on including three exponentials. Table 1-3 represents time constants (t_1, t_2 and t_3) and their amplitudes (a_1, a_2 and a_3) obtained by triexponential fitting, with one of the time constants (t_3) fixed at 1000 ps (this constant time component can be justified when we analysed THz transients by global fitting using the kinetic rate equation discussed further). Average time, $< t >$ of each fluence dependent THz transient can be calculated using the following equations.

$$< t >= \sum_i f_i t_i \tag{4}$$

$$f_i = \frac{a_i t_i}{\sum_i a_i t_i} \tag{5}$$

f_i is contribution of ith term or process over the entire time. t_1 and t_2 correspond to the fastest and intermediate time constants of two exponential functions, respectively, and t_3 corresponds to the slowest fixed time constant. The fast and intermediate time constants for all three pump excitation wavelengths do not vary with fluence. This trend in time constants results from weak dependence of carrier dynamics of few-layer BP NPs films. Carrier dynamics at 480 nm and 600 nm pump excitation show similar time constants, whereas carrier dynamics at 800 nm show slightly higher time constants t_1 and t_2. Among all three time components, time component t_2 has the maximum contribution to the total amplitude, at least in the low fluence regime. The process corresponds to t_2 has a dominant pathway for recovery of photocarriers (carrier recombination) in few-layer BP NPs film.

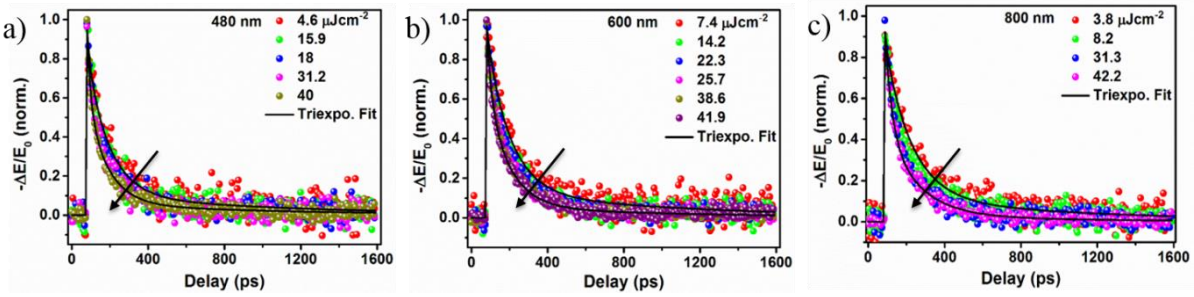

Figure 5. *Normalised THz differential transmission traces at three excitation wavelengths a) 480 nm, b) 600 nm, and c) 800 nm. The solid lines are the fits of the transients to triexponential decay function at the lowest and highest fluences at respective pump wavelengths.*

Table 1. *The fitted parameters (time constant and coefficients) obtained from the triexponential fits of the fluence-dependent THz transients at 480 nm pump. (Errors are given in parentheses.)*

Fluence ($\mu J/cm^2$) **480 nm**	Surface Photon density (10^{13} cm^{-2})	t_1 (ps)	a_1	t_2 (ps)	a_2	t_3 (ps)	a_3	$< t >$ (ps)
4.6	1.12	18.4 (0.8)	0.135 (0.003)	117.2 (0.5)	0.710 (0.003)	1000	0.106 (0.000)	604.0 (0.7)
15.9	3.84	28.1 (0.3)	0.400 (0.003)	141.7 (0.6)	0.566 (0.003)	1000	0.061 (0.000)	475.5 (0.5)
18.1	4.36	22.6 (0.2)	0.358 (0.002)	124.0 (0.4)	0.556 (0.002)	1000	0.075 (0.000)	550.3 (0.4)
31.2	7.54	24.7 (0.3)	0.364 (0.002)	124.9 (0.5)	0.540 (0.002)	1000	0.039 (0.000)	415.6 (0.5)
40.0	9.66	18.4 (0.1)	0.380 (0.002)	107.7 (0.3)	0.531 (0.002)	1000	0.059 (0.000)	529.1 (0.2)

Table 2*. The fitted parameters (time constants and coefficients) obtained from the triexponential fits of the fluence-dependent THz transients at 600 nm pump. (Errors are given in parentheses.)*

Fluence ($\mu J/cm^2$) **600 nm**	Surface Photon density (10^{13} cm^{-2})	t_1 (ps)	a_1	t_2 (ps)	a_2	t_3 (ps)	a_3	$< t >$ (ps)
7.4	2.24	18.8 (2.3)	0.048 (0.003)	122.3 (0.4)	0.795 (0.003)	1000	0.136 (0.000)	631.1 (2.0)
14.2	4.28	15.2 (0.5)	0.114 (0.002)	119.1 (0.3)	0.769 (0.002)	1000	0.084 (0.000)	536.2 (0.4)

22.3	6.73	24.7 (0.5)	0.188 (0.002)	116.5 (0.3)	0.762 (0.002)	1000	0.079 (0.000)	520.2 (0.4)
25.7	7.75	17.2 (0.2)	0.231 (0.001)	113.0 (0.2)	0.717 (0.001)	1000	0.058 (0.000)	469.0 (0.2)
38.6	11.63	23.3 (0.2)	0.348 (0.002)	118.1 (0.3)	0.610 (0.002)	1000	0.062 (0.000)	496.1 (0.3)
41.9	12.65	21.8 (0.2)	0.329 (0.002)	114.3 (0.3)	0.603 (0.002)	1000	0.058 (0.000)	491.4 (0.2)

Table 3*. The fitted parameters (time constants and coefficients) obtained from the triexponential fits of the fluence-dependent THz transients at 800 nm pump. (Errors are given in parentheses.)*

Fluence ($\mu J/cm^2$) **800 nm**	Surface Photon density ($10^{13} cm^{-2}$)	t_1 (ps)	a_1	t_2 (ps)	a_2	t_3 (ps)	a_3	$< t >$ (ps)
3.8	1.53	55.8 (9.8)	0.050 (0.014)	142.9 (1.3)	0.733 (0.014)	1000	0.122 (0.000)	597.4 (8.7)
8.2	3.31	59.8 (0.8)	0.356 (0.006)	173.8 (1.3)	0.493 (0.006)	1000	0.066 (0.000)	474.4 (1.1)
31.3	12.59	32.3 (0.3)	0.360 (0.002)	141.6 (0.5)	0.573 (0.002)	1000	0.0470 (0.000)	421.3 (0.4)
42.2	16.96	35.8 (0.3)	0.477 (0.003)	169.6 (0.9)	0.430 (0.003)	1000	0.030 (0.000)	356.8 (0.8)

a) Processes attributed to time components obtained by multiexponential fitting

Several reports on carrier dynamics are present in the literature on various forms of black phosphorus. Transient absorption spectroscopy of black phosphorus quantum dots showed wavelength- and power-independent carrier dynamics with biexponential decay recovery,[9] which is very similar to what we observed in our few-layer BP NPs film. The fastest time scale, which is about 85 ps, is attributed to radiative recombination. In our study, we have observed that the time constant, t_2 is between 120 and 140 ps for different excitation wavelengths, which could be due to radiative (bimolecular) recombination. A higher time constant in our few-layer BP NPs film most likely results from the bigger NPs also with the non-uniform size distribution of NPs.[23-25] In differential reflection measurements of multilayer BP (thickness of about 16 nm), a photocarrier lifetime of about 100 ps has been reported.[10] In the same report, the initial

fast recovery of about 20 ps of the transient signal was observed to be independent of excitation fluence (from 2 to 10 μJcm^{-2}) upon photoexcitation of 760 nm pump wavelength. Fluence-independent time component in the range of 20 ps to 40 ps is also observed in our few-layer BP NPs film sample. The excitonic lifetime of about 150 ps was reported upon pumping a sample with a 400 nm wavelength and probing it with a 514 nm.[11] Extracted lifetime was found to be insensitive to different pump power. Bulk BP was studied using transient differential reflection spectroscopy, and biexponential decay dynamics were observed with 15 ps and 83 ps time components. The fast timescale is assigned to the relaxation of hot carriers to the band edge, whereas the slower time component is assigned to the photocarrier lifetime.[12] In another work of a two-colour pump-probe experiment in which exciting thin layers (~80 layers) with a 780 nm, two relaxation time scales, 180 ps and 1.3 ns, were observed upon probing with a 1560 nm pump wavelength.[13] In this study, the longer time constant was assigned to photocarrier recombination. Single exponential decay with a time component of about 770 ps was found in the same study at low excitation power. This study was carried out on a photocarrier density of 10^{14} cm^{-2}. A lifetime of about 1.34 ns for minority carriers in multilayer BP is associated with a trap-associated recombination process.[14] This lifetime is closely related to the t_3 time component in our study. The THz transients at all pump wavelengths become parallel to the pump-probe delay axis beyond ~1 ns and are independent of the pump fluence (carrier density). These two characteristics indicate that the slowest carrier recombination channel (t_3) is trap-assisted recombination of carriers, which has a monomolecular dependence on carrier density, as well as trap density.

b) Mobility and diffusion lengths

Various studies show excellent transport properties of black phosphorus.[3, 8] Charge carrier mobility is an extremely important figure of merit parameter and is directly related to the transport property of any semiconductor for its optoelectronic applications. Here, we have calculated charge carrier mobility and diffusion length from photoconductivity measured in the non-contact fashion through the TRTS study of a few-layer BP NPs film. Effective charge carrier mobility ($\varphi\mu$) and diffusion length (L_D) have been calculated using photoconductivity ($\Delta\sigma$) by the following equations.

$$\varphi\mu = \frac{\Delta\sigma}{eN_0} \tag{6}$$

$$L_D = \sqrt{\frac{< t > \mu k_B T}{q}} \tag{7}$$

The mobility and diffusion length values calculated from our experimentally observed THz photoconductivities ($\Delta\sigma$) are presented in Tables 4, 5, and 6 for excitation wavelengths of 480 nm, 600 nm, and 800 nm, respectively. It is evident that the mobility values obtained through TRTS in this work are significantly lower compared to earlier reports on bulk BP.

Carrier mobility strongly depends on crystal axes (zigzag and armchair) of black phosphorus, along which carrier moves having different effective masses. Since the few-layer NPs which we probed are not uniformly aligned, we are measuring effective mobility for carriers irrespective of a particular type and particular direction. Hence, our measurement is resulting from randomly oriented few-layer nanocrystals, and we will try to quantify our result with bulk phase, multilayer BP film.

According to a hall measurement at room temperature black phosphorus (with a bandgap of 0.33 eV), the electron and hole mobilities were calculated to be 220 cm^2/Vs and 350 cm^2/Vs, respectively. [26] Here, it is important to note that our film is not a uniformly stacked layered 2D system but randomly oriented bulk semiconducting layers. Low mobility values in our film are probably due to the random orientation of layers (or nanoparticles).

Diffusion length indicates the average distance that charge carrier transit before being recombined, and in this case, ~50 nm is a decent estimate given a carrier density of 10^{18} cm^{-3}. The magnitude of effective mobility and diffusion length of few-layer BP NPs remain in the same range for all three pump wavelengths.

Table 4. *Mobility and diffusion length at different excitation parameters at pump wavelength of 480 nm. (peak photoconductivity = $\Delta\sigma_{peak}$) (Errors are given in parentheses.)*

Fluence ($\mu J/cm^2$) ***480 nm***	Surface Photon density (10^{13} cm^{-2})	N_{ph} (10^{18} cm^{-3})	N_0 (10^{18} cm^{-3})	$-\Delta E/E_0$ (max.)	$\Delta\sigma_{peak}$ (S/cm)	Mobility (cm^2/Vs)	Diffusion length (nm)

4.64	1.12	1.08	2.16	0.014 (0.001)	2.19 (0.20)	6.35 (0.58)	99.59 (4.62)
15.9	3.84	3.71	7.42	0.022 (0.001)	3.58 (0.24)	3.02 (0.20)	60.90 (2.080)
18.1	4.36	4.21	8.42	0.028 (0.001)	4.53 (0.15)	3.36 (0.11)	69.18 (1.16)
31.2	7.54	7.28	14.56	0.031 (0.003)	5.06 (0.49)	2.17 (0.21)	48.30 (2.36)
40.0	9.66	9.33	18.66	0.039 (0.001)	6.39 (0.21)	2.14 (0.07)	54.14 (0.90)

Table 5*. Mobility and diffusion length at different excitation parameters at pump wavelength of 600 nm. (Errors are given in parentheses.)*

Fluence ($\mu J/cm^2$) **600 nm**	Surface Photon density ($10^{13} cm^{-2}$)	N_{ph} ($10^{18} cm^{-3}$)	N_0 ($10^{18} cm^{-3}$)	$-\Delta E/E_0$ (max.)	$\Delta\sigma_{peak}$ (S/cm)	Mobility (cm^2/Vs)	Diffusion length (nm)
7.4	2.24	1.10	2.21	0.010 (0.001)	1.56 (0.16)	4.40 (0.46)	84.79 (4.60)
14.2	4.28	2.11	4.22	0.015 (0.002)	2.51 (0.32)	3.72 (0.48)	71.84 (4.63)
22.3	6.73	3.31	6.63	0.025 (0.002)	4.02 (0.33)	3.79 (0.31)	71.42 (2.93)
25.7	7.75	3.82	7.63	0.032 (0.002)	5.13 (0.27)	4.20 (0.22)	71.41 (1.86)
38.6	11.63	5.73	11.45	0.037 (0.002)	5.98 (0.35)	3.26 (0.19)	64.71 (1.92)
41.9	12.65	6.23	12.46	0.041 (0.002)	6.69 (0.33)	3.36 (0.17)	65.34 (1.64)

Table 6. *Mobility and diffusion length at different excitation parameters at pump wavelength of 800 nm. (Errors are given in parentheses.)*

Fluence ($\mu J/cm^2$) **800 nm**	Surface Photon density ($10^{13} cm^{-2}$)	N_{ph} ($10^{18} cm^{-3}$)	N_0 ($10^{18} cm^{-3}$)	$-\Delta E/E_0$ (max.)	$\Delta\sigma_{peak}$ (S/cm)	Mobility (cm^2/Vs)	Diffusion length (nm)
3.8	1.53	0.46	0.92	0.011 (0.002)	1.83 (0.26)	12.35 (1.74)	138.18 (10.75)
8.2	3.31	1.00	2.00	0.022 (0.001)	3.65 (0.22)	11.37 (0.68)	118.12 (3.67)
31.3	12.59	3.81	7.62	0.034 (0.002)	5.50 (0.34)	4.51 (0.28)	70.61 (2.23)
42.2	16.96	5.14	10.28	0.045 (0.002)	7.37 (0.25)	4.48 (0.15)	64.31 (1.18)

c) Modelling THz transient traces by kinetic rate equation by the global fitting procedure

To better understand charge carrier recombination in a few-layer BP NPs film, pump-induced fluence-dependent THz traces were modelled using a kinetic rate equation by performing global analysis, explained in Chapter 2.

Fluence-dependent THz transients were globally fitted to a kinetic rate equation for each pump excitation wavelength. We have utilised a kinetic rate equation that included only monomolecular and bimolecular recombination terms.

$$\frac{dn}{dt} = -k_1 n - k_2 n^2 \qquad (8)$$

Here, n is photoexcited carrier density. k_1 and k_2 are monomolecular (first order) and bimolecular (second order) rate constants, respectively. Our attempt to globally fit THz transients, including the third-order term ($-k_3 n^3$), i.e. Auger recombination term in equation 8, did not improve the fitting (i.e. chi-square value of global fitting). Figure 6 shows photoinduced THz transients and their global fits at three wavelengths (THz transients and their corresponding fits are offset vertically and horizontally by constant magnitude for visual clarity).

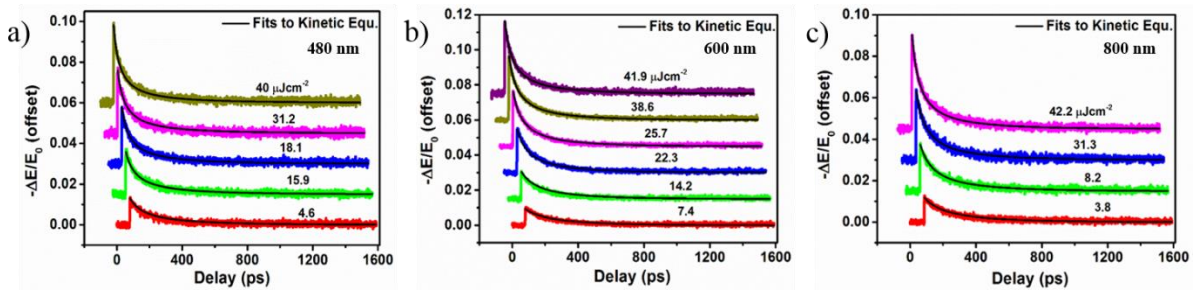

Figure 6. *Global fitting of THz transients to the kinetic model for pump wavelengths of a) 480 nm, a) 600 nm, and c) 800 nm.*

Table 7 lists wavelength-dependent rate constants. Rate constants are obtained using measured THz transients and fitting these transients, as described in Chapter 2. We have obtained first order and second order rate constants for all three wavelengths. As shown in Table 7, both rate

constants k_1 and k_2 fall in the same orders of magnitude for all pump excitation wavelengths, which can be justifiable as rate constants are intrinsic parameters of semiconductor materials.

Table 7. *Rate constants obtained for three excitation pump wavelengths at carrier concentration of about 10^{18} cm^{-3}. (Errors are given in parentheses.)*

Pump wavelength (nm)	$k_1(s^{-1})$	$k_2(cm^3s^{-1})$
480	2.003×10^9 (0.007×10^9)	1.894×10^{-9} (0.003×10^{-9})
600	2.795×10^9 (0.005×10^9)	1.670×10^{-9} (0.002×10^{-9})
800	2.624×10^9 (0.006×10^9)	2.731×10^{-9} (0.004×10^{-9})

Carrier-recombination rate constants of BP have been reported in few studies earlier, with one order of magnitude of difference compared to our study.[14, 15, 27] Since few-layer BP NPs studied here were prepared from a chemical route, different defect and dielectric environments can be possible. Rate constants may be affected by the crystal structure, morphology, dielectric environment and purity of the material.[15] In addition, the stacking arrangement of BP layers and the size of semiconductor particles can also affect the magnitude of rate constants. The dielectric constant is related to the second order rate constant in the case of diffusion-limited radiative process.[15] Our sample is NPs solution drop-casted on a substrate. Therefore, the film may not have perfectly aligned BP layers in a multilayer form, leading to different values of rate constants.

First order recombination rate constant (k_1) in our NPs film is in the order of 10^9 s^{-1}. It is two orders of magnitude higher than 2 mm thick BP at room temperature, as studied from the time-resolved microwave conductivity (TRMC) experiment.[15] In multilayer black phosphorus (20–80 atomic layers) and 150 nm thick BP flakes, k_1 of the order of 10^9 s^{-1} was found by time-resolved photoconduction measurements and time-resolved differential transmission measurements,[27] [14], which is the same order of magnitude as seen in our study. Radiative (second order) recombination rate constant (k_2) is one order of magnitude less than our study in all three studies.[14, 15, 27]

Deviations in k_2 (in our study as compared to earlier reports as shown in Table 8) is possibly due to the number of layers probed under transient measurement, as in our case, we are possibly probing layers up to which it behaves as thick film.

Values of rate constants, k_1 and k_2 obtained in our work (Table 8) suggests that trap-assisted recombination and bimolecular recombination can be dominant and significant channels of charge carrier recombination at experimental excitation conditions when compared to rate constants in low bandgap semiconductors that are applied in infrared optoelectronics systems such as InAs, and InSb.[28]

Table 8. *Rate constants of black phosphorus in earlier reports at room temperature.*

Sample	Carrier concentration (cm^{-3})	k_1 (s^{-1})	k_2 ($cm^3 s^{-1}$)	Technique	Ref.
BP layers of 2 mm	10^{16}	10^{7}	2×10^{-10}	Time-resolved microwave conductivity	15
multilayer BP (20–80 layers)	10^{18}	10^{9}	1.9×10^{-10}	Time-resolved photoconduction measurements	27
BP flake of 150 nm	10^{19}	10^{8}	5.9×10^{-10}	Time-resolved differential transmission	14

The magnitude of the monomolecular rate constant, k_1 is in the order of 10^9 s^{-1} and inverse of k_1 , which come in the order of nanoseconds (ns), could be a rough estimation of the time component (t_3) related to the monomolecular recombination process. In the earlier section (b), multiexponential fitting of THz transient, we have fixed one of the time components to 1000 ps. i.e. 1 ns (we have assigned this process to trap-assisted recombination), and here, we can justify the assumption of fixing to 1 ns from the first-order rate constant value.

Compared to graphene, which is the most studied elemental 2D material, the kinetic recovery of the carrier of the few-layer BP NPs film studied in this work is relatively slower. In few-layer graphene, relaxation of photocarriers has been observed in the order of the few tens ps range, which is due to almost zero bandgap (narrow bandgap), strong carrier-carrier and carrier-photon scattering.[29-34]

Potential light-emitting applications of FLBP

We have observed photoluminescence (PL) emission from thin films of FLBP NPs in near-infrared regions (PL peaks around 930 nm to 1001 nm) upon excitation with different wavelengths (from 618 nm to 670 nm), as shown in Figure 2d. In Table 8, we have compared some of the previous studies on black phosphorus (thin/multilayer films) with different techniques, which showed bimolecular rate constant (k_2) of the order of 10^{-10} cm^3s^{-1} at carrier concentration varying from 10^{16} to 10^{19} cm^{-3}.[15 27 14] Our THz work on FLBP NPs film found a bimolecular rate constant is around ~10^{-9} cm^3s^{-1} at carrier concentrations 10^{18} to 10^{19} cm^{-3}. Considering PL in the IR region (shown in Figure 2d) and relatively high rate constant (k_2) collectively made us think that this system of FLBP NPs could be potentially exploited in near IR emission applications, provided proper care is taken in making devices as BP is highly reactive to oxygen in the air.

6.4 Conclusions

Black phosphorus (BP) is an emerging, elemental two-dimensional material and has been re-investigated in the last few years due to its promising optical, electronic and anisotropic properties. In this chapter, we have investigated the ultrafast response of few-layer BP NPs film using the TRTS technique in transmission mode. We found that the carrier dynamics of few-layer BP NPs film is independent of excitation wavelengths, and it is weakly dependent on pump fluence at a particular wavelength under a linear excitation regime. Wavelength-independent carrier dynamics of a few-layer BP NPs film can be understood as a photoexcited response from the bulk-like BP phase due to the low bandgap of NPs film. Recombination channels are studied from time constants and rate constants obtained by fitting fluence-dependent photoinduced THz transients at a particular wavelength. Considering the low bandgap of few-layer BP NPs, the high bimolecular rate constant and slow photocarrier recombination time (in hundreds of ps) can make black phosphorus an attractive and potential material for light-emitting applications, especially in the near-infrared frequency range.

6.5 References

1. You, J.; Luo, Y.; Yang, J.; Zhang, J.; Yin, K.; Wei, K.; Zheng, X.; Jiang, T., Hybrid/Integrated Silicon Photonics Based on 2D Materials in Optical Communication Nanosystems. *Laser & Photonics Reviews* **2020,** *14* (12), 2000239.
2. Ling, X.; Wang, H.; Huang, S.; Xia, F.; Dresselhaus, M. S., The renaissance of black phosphorus. *Proceedings of the National Academy of Sciences* **2015,** *112* (15), 4523-4530.
3. Xia, F.; Wang, H.; Jia, Y., Rediscovering black phosphorus as an anisotropic layered material for optoelectronics and electronics. *Nature Communications* **2014,** *5* (1), 4458.
4. Tran, V.; Soklaski, R.; Liang, Y.; Yang, L., Layer-controlled band gap and anisotropic excitons in few-layer black phosphorus. *Physical Review B* **2014,** *89* (23), 235319.
5. Castellanos-Gomez, A., Black Phosphorus: Narrow Gap, Wide Applications. *The Journal of Physical Chemistry Letters* **2015,** *6* (21), 4280-4291.
6. Xia, F.; Wang, H.; Xiao, D.; Dubey, M.; Ramasubramaniam, A., Two-dimensional material nanophotonics. *Nature Photonics* **2014,** *8* (12), 899-907.
7. Tan, C.; Cao, X.; Wu, X.-J.; He, Q.; Yang, J.; Zhang, X.; Chen, J.; Zhao, W.; Han, S.; Nam, G.-H.; Sindoro, M.; Zhang, H., Recent Advances in Ultrathin Two-Dimensional Nanomaterials. *Chemical Reviews* **2017,** *117* (9), 6225-6331.
8. Li, L.; Yu, Y.; Ye, G. J.; Ge, Q.; Ou, X.; Wu, H.; Feng, D.; Chen, X. H.; Zhang, Y., Black phosphorus field-effect transistors. *Nature Nanotechnology* **2014,** *9* (5), 372-377.
9. Chen, L.; Zhang, C.; Li, L.; Wu, H.; Wang, X.; Yan, S.; Shi, Y.; Xiao, M., Ultrafast Carrier Dynamics and Efficient Triplet Generation in Black Phosphorus Quantum Dots. *The Journal of Physical Chemistry C* **2017,** *121* (23), 12972-12978.
10. He, J.; He, D.; Wang, Y.; Cui, Q.; Bellus, M. Z.; Chiu, H.-Y.; Zhao, H., Exceptional and Anisotropic Transport Properties of Photocarriers in Black Phosphorus. *ACS Nano* **2015,** *9* (6), 6436-6442.
11. Chen, R.; Tang, Y.; Zheng, X.; Jiang, T., Giant nonlinear absorption and excited carrier dynamics of black phosphorus few-layer nanosheets in broadband spectra. *Applied Optics* **2016,** *55* (36), 10307-10312.
12. Zereshki, P.; Wei, Y.; Ceballos, F.; Bellus, M. Z.; Lane, S. D.; Pan, S.; Long, R.; Zhao, H., Photocarrier dynamics in monolayer phosphorene and bulk black phosphorus. *Nanoscale* **2018,** *10* (24), 11307-11313.
13. Suess, R. J.; Jadidi, M. M.; Murphy, T. E.; Mittendorff, M., Carrier dynamics and transient photobleaching in thin layers of black phosphorus. *Applied Physics Letters* **2015,** *107* (8), 081103.
14. Aytac, Y.; Mittendorff, M.; Murphy, T. E., Probing the free-carrier absorption in multi-layer black phosphorus. *Applied Physics Letters* **2018,** *113* (3), 031108.
15. Bhaskar, P.; Achtstein, A. W.; Vermeulen, M. J. W.; Siebbeles, L. D. A., Radiatively Dominated Charge Carrier Recombination in Black Phosphorus. *The Journal of Physical Chemistry C* **2016,** *120* (25), 13836-13842.
16. Muduli, S. K.; Varrla, E.; Xu, Y.; Kulkarni, S. A.; Katre, A.; Chakraborty, S.; Chen, S.; Sum, T. C.; Xu, R.; Mathews, N., Evolution of hydrogen by few-layered black phosphorus under visible illumination. *Journal of Materials Chemistry A* **2017,** *5* (47), 24874-24879.

17. Muduli, S.; Pandey, P.; Devatha, G.; Babar, R.; M, T.; Kothari, D. C.; Kabir, M.; Pillai, P. P.; Ogale, S., Photoluminescence Quenching in Self-Assembled CsPbBr3 Quantum Dots on Few-Layer Black Phosphorus Sheets. *Angewandte Chemie International Edition* **2018,** *57* (26), 7682-7686.
18. Zhang, X.; Xie, H.; Liu, Z.; Tan, C.; Luo, Z.; Li, H.; Lin, J.; Sun, L.; Chen, W.; Xu, Z.; Xie, L.; Huang, W.; Zhang, H., Black Phosphorus Quantum Dots. *Angewandte Chemie International Edition* **2015,** *54* (12), 3653-3657.
19. Liang, S.; Hasan, M. N.; Seo, J. H., Direct Observation of Raman Spectra in Black Phosphorus under Uniaxial Strain Conditions. *Nanomaterials (Basel)* **2019,** *9* (4).
20. Morita, A., Semiconducting black phosphorus. *Applied Physics A* **1986,** *39* (4), 227-242.
21. Jepsen, P. U.; Cooke, D. G.; Koch, M., Terahertz spectroscopy and imaging – Modern techniques and applications. *Laser & Photonics Reviews* **2011,** *5* (1), 124-166.
22. Li, D.; Jussila, H.; Karvonen, L.; Ye, G.; Lipsanen, H.; Chen, X.; Sun, Z., Polarization and Thickness Dependent Absorption Properties of Black Phosphorus: New Saturable Absorber for Ultrafast Pulse Generation. *Scientific Reports* **2015,** *5* (1), 15899.
23. Li, G.; Xue, X.; Lin, X.; Yuan, S.; Tang, N.; Chu, F.; Cui, H.; Ma, G., Evolution of terahertz conductivity in ZnSe nanocrystal investigated with optical-pump terahertz-probe spectroscopy. *Applied Physics A* **2014,** *116* (1), 45-50.
24. Beard, M. C.; Turner, G. M.; Schmuttenmaer, C. A., Size-Dependent Photoconductivity in CdSe Nanoparticles as Measured by Time-Resolved Terahertz Spectroscopy. *Nano Letters* **2002,** *2* (9), 983-987.
25. Kumar, A.; Solanki, A.; Manjappa, M.; Ramesh, S.; Srivastava, Y. K.; Agarwal, P.; Sum, T. C.; Singh, R., Excitons in 2D perovskites for ultrafast terahertz photonic devices. *Science Advances 6* (8), eaax8821.
26. Keyes, R. W., The Electrical Properties of Black Phosphorus. *Physical Review* **1953,** *92* (3), 580-584.
27. Suess, R. J.; Leong, E.; Garrett, J. L.; Zhou, T.; Salem, R.; Munday, J. N.; Murphy, T. E.; Mittendorff, M., Mid-infrared time-resolved photoconduction in black phosphorus. *2D Materials* **2016,** *3* (4), 041006.
28. Levinshtein, M.; Rumyantsev, S.; Shur, M., *Handbook Series on Semiconductor Parameters*. WORLD SCIENTIFIC: **1996**; p 452.
29. George, P. A.; Strait, J.; Dawlaty, J.; Shivaraman, S.; Chandrashekhar, M.; Rana, F.; Spencer, M. G., Ultrafast Optical-Pump Terahertz-Probe Spectroscopy of the Carrier Relaxation and Recombination Dynamics in Epitaxial Graphene. *Nano Letters* **2008,** *8* (12), 4248-4251.
30. Docherty, C. J.; Johnston, M. B., Terahertz Properties of Graphene. *Journal of Infrared, Millimeter, and Terahertz Waves* **2012,** *33* (8), 797-815.
31. Jnawali, G.; Rao, Y.; Yan, H.; Heinz, T. F., Observation of a Transient Decrease in Terahertz Conductivity of Single-Layer Graphene Induced by Ultrafast Optical Excitation. *Nano Letters* **2013,** *13* (2), 524-530.
32. Tielrooij, K. J.; Song, J. C. W.; Jensen, S. A.; Centeno, A.; Pesquera, A.; Zurutuza Elorza, A.; Bonn, M.; Levitov, L. S.; Koppens, F. H. L., Photoexcitation cascade and multiple hot-carrier generation in graphene. *Nature Physics* **2013,** *9* (4), 248-252.
33. Kar, S.; Mohapatra, D. R.; Freysz, E.; Sood, A. K., Tuning photoinduced terahertz conductivity in monolayer graphene: Optical-pump terahertz-probe spectroscopy. *Physical Review B* **2014,** *90* (16), 165420.

34. Dawlaty, J. M.; Shivaraman, S.; Chandrashekhar, M.; Rana, F.; Spencer, M. G., Measurement of ultrafast carrier dynamics in epitaxial graphene. *Applied Physics Letters* **2008,** *92* (4), 042116.

Chapter 7

Summary and Outlook

Terahertz (THz) spectroscopy is one of the most important ultrafast spectroscopic techniques developed in the last three decades. In our home-built ultrafast spectroscopy laboratory, we have set up and implemented THz time-domain spectroscopy (THz-TDS) and time-resolved THz spectroscopy (TRTS) in reflection and transmission geometries based on laser-induced air plasma generation and detection of broadband THz radiations. These techniques primarily rely on ultrafast laser sources, so photoconductivity in transient states is investigated with hundreds of femtosecond resolutions. In this thesis, the investigations of semiconductors with potential for application in optoelectronics, high-energy radiation detectors, and thermoelectrics are carried out using THz time-domain spectroscopy and time-resolved THz spectroscopy.

Despite having a bandgap in the UV frequency range, thallium halide semiconductor nanocrystals and bulk films demonstrated fairly high carrier mobility and long diffusion length as measured from the noncontact TRTS technique. These excellent transport parameters (high mobility >250 cm^2/Vs and long diffusion length ~1μm) are most likely derived from its perovskite-like defect-tolerant electronic band structure. Also, with bandgap in the UV region, TlX NCs show reasonably high PL efficiency (~10%), suggesting defect-tolerant behaviour TlX. Similar types of charge carrier dynamics are found for TlBr and TlI in their NCs films and bulk films. Slower decay is observed for TlBr compared to TlI due to the saturation of trap states, most likely surface traps. Other detailed experiments will be necessary to validate claims of TlX being a defect-tolerant system, and our study will definitely be one of the most important in this direction.

InSe and TlSe show low thermal conductivity. Hence, they are potential candidates for thermoelectrics. Electronic conductivity plays a significant role in thermoelectric semiconductors and is directly connected to the transport properties of semiconductors. Also, the attractive properties of III-VI layered InSe have generated tremendous interest recently. TRTS is utilised in tracking transport properties by measuring photoexcited charge carrier dynamics, photoconductivity, carrier mobility, diffusion length, carrier lifetime etc. Charge carrier dynamics decipher a lot of information in the intrinsic photoresponse of semiconductors. InSe has shown slowing down carrier dynamics with increasing excitation fluence. This behaviour of photoexcited semiconductors occurs when trap states get filled at experimental excitation conditions. This also indirectly estimated the density of trap states, most likely surface trap states responsible for saturation seen in carrier dynamics. Carrier mobility and diffusion lengths can be traced more systematically, including layer-dependent

experiments on InSe using TRTS. TlSe is not much explored in optoelectronics applications (especially in the infrared regions of the EM radiation) point of view despite being part of a class III-VI semiconductors and containing Thallium (heavy metal) as one of the constituents. This study on InSe and TlSe will help identify the photophysical properties of these semiconductors.

We have conducted time-resolved THz spectroscopy on few-layer black phosphorus NPs film to unravel their wavelength-dependent charge carrier dynamics. Charge carrier recombination is monitored by photoexciting few-layer BP NPs film with excitation photons of wavelengths 480 nm, 600 nm, and 800 nm. Our TRTS study suggests that the dynamics of photocarriers are weakly dependent on excitation fluence at all excitation wavelengths used. Multicarrier recombination pathways are found to include efficient bimolecular processes at experimental conditions. Compared to elemental 2D graphene, carrier recombination is found to be slower (~500 ps) in few-layer BP NPs film. The photocarrier dynamics of few-layer BPs are comparable to those of bulk BP, where the wavelength-independent charge carrier dynamics is expected due to its low bandgap (~0.3 eV).

TRTS study of semiconductors studied in this thesis in various other photocarrier concentrations, preferably at lower photocarrier concentrations, will shed more light on its applicability from a broader perspective. Also, a systematic study of frequency-resolved THz spectra of these materials will reveal the role of phonons in carrier dynamics, phonon dynamics, and carrier-phonon interactions.

SPRINGER NATURE LICENSE
TERMS AND CONDITIONS

Sep 06, 2023

This Agreement between Mr. Avinash Warankar ("You") and Springer Nature ("Springer Nature") consists of your license details and the terms and conditions provided by Springer Nature and Copyright Clearance Center.

License Number	5623040106568
License date	Sep 06, 2023
Licensed Content Publisher	Springer Nature
Licensed Content Publication	Nature Materials
Licensed Content Title	Exciton polarizability in semiconductor nanocrystals
Licensed Content Author	Feng Wang et al
Licensed Content Date	Oct 8, 2006
Type of Use	Thesis/Dissertation
Requestor type	academic/university or research institute
Format	print and electronic
Portion	figures/tables/illustrations
Number of figures/tables/illustrations	3
Would you like a high resolution image with your order?	no
Will you be translating?	no

Circulation/distribution	1 - 29
Author of this Springer Nature content	no
Title	Ultrafast Time-Resolved Terahertz Spectroscopy of Charge Carrier Dynamics in Semiconductors
Institution name	Indian Institute of Science Education and Research, Pune
Expected presentation date	Oct 2023
Portions	Figure 2 , Figure 1
Requestor Location	Mr. Avinash Warankar Dept of chemistry, IISER pune pune, other 411008 India Attn: IISER Pune
Total	0.00 USD

Terms and Conditions

Springer Nature Customer Service Centre GmbH Terms and Conditions

The following terms and conditions ("Terms and Conditions") together with the terms specified in your [RightsLink] constitute the License ("License") between you as Licensee and Springer Nature Customer Service Centre GmbH as Licensor. By clicking 'accept' and completing the transaction for your use of the material ("Licensed Material"), you confirm your acceptance of and obligation to be bound by these Terms and Conditions.

1. Grant and Scope of License

1. 1. The Licensor grants you a personal, non-exclusive, non-transferable, non-sublicensable, revocable, world-wide License to reproduce, distribute, communicate to the public, make available, broadcast, electronically transmit or create derivative works using the Licensed Material for the purpose(s) specified in your RightsLink Licence Details only. Licenses are granted for the specific use requested in the order and for no other use, subject to these Terms and Conditions. You acknowledge and agree that the rights granted to you under this License do not include the right to modify, edit, translate, include in collective works, or create derivative works of the Licensed Material in whole or in part unless expressly stated in your RightsLink Licence Details. You may use the Licensed Material only as permitted under this

Agreement and will not reproduce, distribute, display, perform, or otherwise use or exploit any Licensed Material in any way, in whole or in part, except as expressly permitted by this License.

1. 2. You may only use the Licensed Content in the manner and to the extent permitted by these Terms and Conditions, by your RightsLink Licence Details and by any applicable laws.

1. 3. A separate license may be required for any additional use of the Licensed Material, e.g. where a license has been purchased for print use only, separate permission must be obtained for electronic re-use. Similarly, a License is only valid in the language selected and does not apply for editions in other languages unless additional translation rights have been granted separately in the License.

1. 4. Any content within the Licensed Material that is owned by third parties is expressly excluded from the License.

1. 5. Rights for additional reuses such as custom editions, computer/mobile applications, film or TV reuses and/or any other derivative rights requests require additional permission and may be subject to an additional fee. Please apply to journalpermissions@springernature.com or bookpermissions@springernature.com for these rights.

2. Reservation of Rights

Licensor reserves all rights not expressly granted to you under this License. You acknowledge and agree that nothing in this License limits or restricts Licensor's rights in or use of the Licensed Material in any way. Neither this License, nor any act, omission, or statement by Licensor or you, conveys any ownership right to you in any Licensed Material, or to any element or portion thereof. As between Licensor and you, Licensor owns and retains all right, title, and interest in and to the Licensed Material subject to the license granted in Section 1.1. Your permission to use the Licensed Material is expressly conditioned on you not impairing Licensor's or the applicable copyright owner's rights in the Licensed Material in any way.

3. Restrictions on use

3. 1. Minor editing privileges are allowed for adaptations for stylistic purposes or formatting purposes provided such alterations do not alter the original meaning or intention of the Licensed Material and the new figure(s) are still accurate and representative of the Licensed Material. Any other changes including but not limited to, cropping, adapting, and/or omitting material that affect the meaning, intention or moral rights of the author(s) are strictly prohibited.

3. 2. You must not use any Licensed Material as part of any design or trademark.

3. 3. Licensed Material may be used in Open Access Publications (OAP), but any such reuse must include a clear acknowledgment of this permission visible at the same time as the figures/tables/illustration or abstract and which must indicate that the Licensed Material is not part of the governing OA license but has been reproduced with permission. This may be indicated according to any standard referencing system but must include at a minimum 'Book/Journal title, Author, Journal Name (if applicable), Volume (if applicable), Publisher, Year, reproduced with permission from SNCSC'.

4. STM Permission Guidelines

4. 1. An alternative scope of license may apply to signatories of the STM Permissions Guidelines ("STM PG") as amended from time to time and made available at

https://www.stm-assoc.org/intellectual-property/permissions/permissions-guidelines/.

4. 2. For content reuse requests that qualify for permission under the STM PG, and which may be updated from time to time, the STM PG supersede the terms and conditions contained in this License.

4. 3. If a License has been granted under the STM PG, but the STM PG no longer apply at the time of publication, further permission must be sought from the Rightsholder. Contact journalpermissions@springernature.com or bookpermissions@springernature.com for these rights.

5. Duration of License

5. 1. Unless otherwise indicated on your License, a License is valid from the date of purchase ("License Date") until the end of the relevant period in the below table:

Reuse in a medical communications project	Reuse up to distribution or time period indicated in License
Reuse in a dissertation/thesis	Lifetime of thesis
Reuse in a journal/magazine	Lifetime of journal/magazine
Reuse in a book/textbook	Lifetime of edition
Reuse on a website	1 year unless otherwise specified in the License
Reuse in a presentation/slide kit/poster	Lifetime of presentation/slide kit/poster. Note: publication whether electronic or in print of presentation/slide kit/poster may require further permission.
Reuse in conference proceedings	Lifetime of conference proceedings
Reuse in an annual report	Lifetime of annual report
Reuse in training/CME materials	Reuse up to distribution or time period indicated in License
Reuse in newsmedia	Lifetime of newsmedia
Reuse in coursepack/classroom materials	Reuse up to distribution and/or time period indicated in license

6. Acknowledgement

6. 1. The Licensor's permission must be acknowledged next to the Licensed Material in print. In electronic form, this acknowledgement must be visible at the same time as the figures/tables/illustrations or abstract and must be hyperlinked to the journal/book's homepage.

6. 2. Acknowledgement may be provided according to any standard referencing system and at a minimum should include "Author, Article/Book Title, Journal name/Book imprint, volume, page number, year, Springer Nature".

7. Reuse in a dissertation or thesis

7. 1. Where 'reuse in a dissertation/thesis' has been selected, the following terms apply: Print rights of the Version of Record are provided for; electronic rights for use only on institutional repository as defined by the Sherpa guideline (www.sherpa.ac.uk/romeo/) and only up to what is required by the awarding institution.

7. 2. For theses published under an ISBN or ISSN, separate permission is required. Please contact journalpermissions@springernature.com or bookpermissions@springernature.com for these rights.

7. 3. Authors must properly cite the published manuscript in their thesis according to current citation standards and include the following acknowledgement: '*Reproduced with permission from Springer Nature*'.

8. License Fee

You must pay the fee set forth in the License Agreement (the "License Fees"). All amounts payable by you under this License are exclusive of any sales, use, withholding, value added or similar taxes, government fees or levies or other assessments. Collection and/or remittance of such taxes to the relevant tax authority shall be the responsibility of the party who has the legal obligation to do so.

9. Warranty

9. 1. The Licensor warrants that it has, to the best of its knowledge, the rights to license reuse of the Licensed Material. **You are solely responsible for ensuring that the material you wish to license is original to the Licensor and does not carry the copyright of another entity or third party (as credited in the published version).** If the credit line on any part of the Licensed Material indicates that it was reprinted or adapted with permission from another source, then you should seek additional permission from that source to reuse the material.

9. 2. EXCEPT FOR THE EXPRESS WARRANTY STATED HEREIN AND TO THE EXTENT PERMITTED BY APPLICABLE LAW, LICENSOR PROVIDES THE LICENSED MATERIAL "AS IS" AND MAKES NO OTHER REPRESENTATION OR WARRANTY. LICENSOR EXPRESSLY DISCLAIMS ANY LIABILITY FOR ANY CLAIM ARISING FROM OR OUT OF THE CONTENT, INCLUDING BUT NOT LIMITED TO ANY ERRORS, INACCURACIES, OMISSIONS, OR DEFECTS CONTAINED THEREIN, AND ANY IMPLIED OR EXPRESS WARRANTY AS TO MERCHANTABILITY OR FITNESS FOR A PARTICULAR PURPOSE. IN NO EVENT SHALL LICENSOR BE LIABLE TO YOU OR ANY OTHER PARTY OR ANY OTHER PERSON OR FOR ANY SPECIAL, CONSEQUENTIAL, INCIDENTAL, INDIRECT, PUNITIVE, OR EXEMPLARY DAMAGES, HOWEVER CAUSED, ARISING OUT OF OR IN CONNECTION WITH THE DOWNLOADING, VIEWING OR USE OF THE LICENSED MATERIAL REGARDLESS OF THE FORM OF ACTION, WHETHER FOR BREACH OF CONTRACT, BREACH OF WARRANTY, TORT, NEGLIGENCE, INFRINGEMENT OR OTHERWISE (INCLUDING, WITHOUT LIMITATION, DAMAGES BASED ON LOSS OF PROFITS, DATA, FILES, USE, BUSINESS OPPORTUNITY OR CLAIMS OF THIRD PARTIES), AND WHETHER OR NOT THE PARTY HAS BEEN ADVISED OF THE POSSIBILITY OF SUCH DAMAGES. THIS LIMITATION APPLIES NOTWITHSTANDING ANY FAILURE OF ESSENTIAL PURPOSE OF ANY LIMITED REMEDY PROVIDED HEREIN.

10. Termination and Cancellation

10. 1. The License and all rights granted hereunder will continue until the end of the applicable period shown in Clause 5.1 above. Thereafter, this license will be terminated and all rights granted hereunder will cease.

10. 2. Licensor reserves the right to terminate the License in the event that payment is not received in full or if you breach the terms of this License.

11. General

11. 1. The License and the rights and obligations of the parties hereto shall be construed, interpreted and determined in accordance with the laws of the Federal Republic of Germany without reference to the stipulations of the CISG (United Nations Convention on Contracts for the International Sale of Goods) or to Germany´s choice-of-law principle.

11. 2. The parties acknowledge and agree that any controversies and disputes arising out of this License shall be decided exclusively by the courts of or having jurisdiction for Heidelberg, Germany, as far as legally permissible.

11. 3. This License is solely for Licensor's and Licensee's benefit. It is not for the benefit of any other person or entity.

Questions? For questions on Copyright Clearance Center accounts or website issues please contact springernaturesupport@copyright.com or +1-855-239-3415 (toll free in the US) or +1-978-646-2777. For questions on Springer Nature licensing please visit https://www.springernature.com/gp/partners/rights-permissions-third-party-distribution

Other Conditions:

Version 1.4 - Dec 2022

Questions? customercare@copyright.com.

IISER PUNE

Avinash Warankar <avinash.warankar@students.iiserpune.ac.in>

RE: Permission Request Form: Avinash Warankar

CONTRACTS-COPYRIGHT (shared) <Contracts-Copyright@rsc.org> Thu, Mar 23, 2023 at 8:10 PM
To: "avinash.warankar@students.iiserpune.ac.in" <avinash.warankar@students.iiserpune.ac.in>

Dear Avinash Warankar

Thank you for your enquiry.

As the article you are requesting to reproduce material from is published under a CC-BY open access licence (https://creativecommons.org/licenses/by/3.0/) you do not have to formally request permission to reproduce material from it and you are therefore free to reuse material from it in your thesis.

Please note that if the material specified below or any part of it appears with credit or acknowledgement to a third party then you must also secure permission from that third party before reproducing that material.

Please ensure that the published article carries a credit to The Royal Society of Chemistry (see http://rsc.li/permissions for details) and that any electronic version of the work includes a hyperlink to the article on the Royal Society of Chemistry website.

Thanks

Becky

Becky Roberts
Contracts & Copyright Executive, Sales Operations

Royal Society of Chemistry

T: +44 (0) 1223 432304 | www.rsc.org

ROYAL SOCIETY OF CHEMISTRY

From: avinash.warankar@students.iiserpune.ac.in <avinash.warankar@students.iiserpune.ac.in>
Sent: 23 March 2023 13:00
To: CONTRACTS-COPYRIGHT (shared) <Contracts-Copyright@rsc.org>
Subject: Permission Request Form: Avinash Warankar

Name: Avinash Warankar

Institution: IISER Pune, India

Email: avinash.warankar@students.iiserpune.ac.in

Address:

Department of Chemistry, IISER Pune, India.

Pune
411008
India

I am preparing the following work for publication:

Article/chapter title: Charge Carrier Dynamics in Thallium Halides (TlX, X=Br, I) Nanocrystals and Bulk Films
Journal/book title: Charge Carrier Dynamics in Thallium Halides (TlX, X=Br, I) Nanocrystals and Bulk Films
Editor/author(s): Avinash Warankar
Publisher: IISER Pune
Is this request for a thesis?: Yes

I would very much appreciate your permission to use the following material:

Journal/book title: Chemical Science
Editor/author(s): Authors of paper Wasim J. Mir, Avinash Warankar, Ashutosh Acharya , Shyamashis Das, Pankaj Mandal and Angshuman Nag
ISBN/DOI: https://doi.org/10.1039/C7SC01219E
Year of publication: 2017
Page(s): 4602-4611
Type of material: figures, images
Figure/image number (if relevant):

Any additional comments:

Agree to terms: I agree

ELSEVIER LICENSE
TERMS AND CONDITIONS

Apr 07, 2023

This Agreement between Mr. Avinash Warankar ("You") and Elsevier ("Elsevier") consists of your license details and the terms and conditions provided by Elsevier and Copyright Clearance Center.

License Number	5523540509645
License date	Apr 07, 2023
Licensed Content Publisher	Elsevier
Licensed Content Publication	Solid State Communications
Licensed Content Title	Structural investigation of InSe layered semiconductors
Licensed Content Author	I. Grimaldi,T. Gerace,M.M. Pipita,I.D. Perrotta,F. Ciuchi,H. Berger,M. Papagno,M. Castriota,D. Pacilé
Licensed Content Date	May 1, 2020
Licensed Content Volume	311
Licensed Content Issue	n/a
Licensed Content Pages	1
Start Page	113855
End Page	0
Type of Use	reuse in a thesis/dissertation
Portion	figures/tables/illustrations

Number of figures/tables/illustrations	1
Format	both print and electronic
Are you the author of this Elsevier article?	No
Will you be translating?	No
Title	Ultrafast Time-Resolved Terahertz Spectroscopy of Charge Carrier Dynamics in Semiconductors
Institution name	Indian Institute of Science Education and Research, Pune
Expected presentation date	Apr 2023
Portions	Figure 1.
Requestor Location	Mr. Avinash Warankar Dept of chemistry, IISER pune pune, other 411008 India Attn: IISER Pune
Publisher Tax ID	GB 494 6272 12
Total	0.00 USD

Terms and Conditions

INTRODUCTION

1. The publisher for this copyrighted material is Elsevier. By clicking "accept" in connection with completing this licensing transaction, you agree that the following terms and conditions apply to this transaction (along with the Billing and Payment terms and conditions established by Copyright Clearance Center, Inc. ("CCC"), at the time that you opened your Rightslink account and that are available at any time at http://myaccount.copyright.com).

GENERAL TERMS

2. Elsevier hereby grants you permission to reproduce the aforementioned material subject to the terms and conditions indicated.

Ultralow Thermal Conductivity in Chain-like TlSe Due to Inherent Tl Rattling

Author: Moinak Dutta, Shidaling Matteppanavar, Matukumilli V. D. Prasad, et al
Publication: Journal of the American Chemical Society
Publisher: American Chemical Society
Date: Dec 1, 2019

PERMISSION/LICENSE IS GRANTED FOR YOUR ORDER AT NO CHARGE

This type of permission/license, instead of the standard Terms and Conditions, is sent to you because no fee is being charged for your order. Please note the following:

- Permission is granted for your request in both print and electronic formats, and translations.
- If figures and/or tables were requested, they may be adapted or used in part.
- Please print this page for your records and send a copy of it to your publisher/graduate school.
- Appropriate credit for the requested material should be given as follows: "Reprinted (adapted) with permission from {COMPLETE REFERENCE CITATION}. Copyright {YEAR} American Chemical Society." Insert appropriate information in place of the capitalized words.
- One-time permission is granted only for the use specified in your RightsLink request. No additional uses are granted (such as derivative works or other editions). For any uses, please submit a new request.

If credit is given to another source for the material you requested from RightsLink, permission must be obtained from that source.

BACK CLOSE WINDOW

JOHN WILEY AND SONS LICENSE
TERMS AND CONDITIONS

Apr 04, 2023

This Agreement between Mr. Avinash Warankar ("You") and John Wiley and Sons ("John Wiley and Sons") consists of your license details and the terms and conditions provided by John Wiley and Sons and Copyright Clearance Center.

License Number	5521840500998
License date	Apr 04, 2023
Licensed Content Publisher	John Wiley and Sons
Licensed Content Publication	Laser & Photonics Reviews
Licensed Content Title	Hybrid/Integrated Silicon Photonics Based on 2D Materials in Optical Communication Nanosystems
Licensed Content Author	Jie You, Yukun Luo, Jie Yang, et al
Licensed Content Date	Nov 12, 2020
Licensed Content Volume	14
Licensed Content Issue	12
Licensed Content Pages	23
Type of use	Dissertation/Thesis
Requestor type	University/Academic
Format	Print and electronic

Portion	Figure/table
Number of figures/tables	1
Will you be translating?	No
Title	Ultrafast Time-Resolved Terahertz Spectroscopy of Charge Carrier Dynamics in Semiconductors
Institution name	Indian Institute of Science Education and Research, Pune
Expected presentation date	Apr 2023
Portions	Figure 1
Requestor Location	Mr. Avinash Warankar Dept of chemistry, IISER pune pune, other 411008 India Attn: IISER Pune
Publisher Tax ID	EU826007151
Total	0.00 USD
Terms and Conditions	

TERMS AND CONDITIONS

This copyrighted material is owned by or exclusively licensed to John Wiley & Sons, Inc. or one of its group companies (each a"Wiley Company") or handled on behalf of a society with which a Wiley Company has exclusive publishing rights in relation to a particular work (collectively "WILEY"). By clicking "accept" in connection with completing this licensing transaction, you agree that the following terms and conditions apply to this transaction (along with the billing and payment terms and conditions established by the Copyright Clearance Center Inc., ("CCC's Billing and Payment terms and conditions"), at the time that you opened your RightsLink account (these are available at any time at http://myaccount.copyright.com).

Terms and Conditions